University of Mississippi

eGrove

Development of Cobalt and Iron Catalysts Bearing Rigid Polydentate Ligands for Proton Reduction and C-H Bond Oxidation

Lizhu Chen
University of Mississippi

Follow this and additional works at: https://egrove.olemiss.edu/etd

Part of the Chemistry Commons

Recommended Citation

DEVELOPMENT OF COBALT AND IRON CATALYSTS BEARING RIGID

POLYDENTATE LIGANDS FOR PROTON REDUCTION AND C-H BOND OXIDATION

A Thesis

Presented in partial fulfillment of requirements

For the degree of Master of Science

In the Department of Chemistry and Biochemistry

The University of Mississippi

by

LIZHU CHEN

May 2019

ABSTRACT

The demand for energy consumption has increased exponentially since the Industrial Revolution. The major source of this energy has been and continues to be fossil fuels. The depletion of fossil fuels and environmental concerns associated with their combustion has motivated us to develop a renewable energy alternative to meet future energy demands. Hydrogen is a clean energy alternative to fossil fuels, which can be generated from solar-driven water splitting. However, more efficient and inexpensive catalysts for the hydrogen evolution reaction (HER) are needed. In this context, hydrogen production has been investigated with a stable and highly reactive cobalt-based catalyst. While petroleum and natural gas are not ideal energy sources, they are important feedstocks of inexpensive hydrocarbons for the chemical and pharmaceutical industries. The selective conversion of C-H bonds into new functional groups under mild conditions is therefore of considerable interest. High-valent nonheme iron-oxo catalysts have been developed as potent oxidants for the functionalization of unactivated C-H bonds. Likewise, the desire to further improve catalyst stability and selectivity for C-H bond oxidation encouraged us to develop and study the coordination chemistry of a polyaromatic ligand that is rigid, tetradentate, and absent of weak C-H bonds to give a strong chelate effect and high stability under strongly oxidizing conditions. The geometry, spin state, redox behavior, and other properties are analyzed for a series of first-row metal complexes.

DEDICATION

I dedicate this Master of Science degree to my parents for always supporting and encouraging

me to pursue my dreams. And my friend Yanbing Zhang who always helps me in life and

research. I am very grateful that my advisor – Dr. Jurss and the University of Mississippi have

given me this opportunity to study at this beautiful university.

LIST OF ABBREVIATIONS AND SYMBOLS

A	Amperes
Å	Angstrom
A/K	Alcohol-to-Ketone Ratio
bpy	Bipyridine
C	Coulomb
C-H	Carbon Hydrogen Bond
°C	degrees Celsius
Cm	centimeter
χ_m	Molar Susceptibility
CV	Cyclic Voltammetry
DCM	Dichloromethane
DMF	Dimethylformamide
ε	Molar extinction coefficient
e^-	electron
emu	Electromagnetic Unit
EtOAc	Ethyl Acetate
EtOH	Ethanol
ESI-MS	Electrospray Ionization Mass Spectrometry
Et_2O	Diethyl Ether
$Fc^{+/0}$	Ferrocene

FE	Faraday Efficiency
g	Gram
GCE	Glassy Carbon Electrode
HAT	Hydrogen atom transfer
HER	Hydrogen Evolution Reaction
H_2O_2	Hydrogen Peroxide
HOMO	Highest occupied molecular orbital
h	Hour
i_{cat}	Current under catalytic atmosphere
i_p	Current under inert atmosphere
IR	Infrared Spectroscopy
kcal	Kilocalories
$K_3Fe(CN)_6$	Potassium Ferricyanide
KHP	Potassium Hydrogen Phthalate
k_{obs}	Rate Constants
KIE	Kinetic Isotope Effect
KNO_3	Potassium Nitrate
λ	Wavelength
LDA	Lithium Diisopropylamide
LFT	Ligand Field Transition
$LiClO_4$	Lithium Perchlorate

LMCT	Ligand metal charge transfer
LUMO	Lowest Unoccupied Molecular Orbital
M	Molar (mol L^{-1})
*m*CPBA	*meta*-chloro perbenzoic acid
Me	Methyl
MeCN	Acetonitrile
μ_{eff}	Magnetic Moment
μ_B	Total Magnetic Moment
MeOH	Methanol
mL	milliliter
MLCT	Metal-to-Ligand Charge Transfer
mM	millimolar
mmol	millimole
mol	mole
mV/s	Millivolts per second
NaCl	Sodium Chloride
NaOH	Sodium Hydroxide
Na$_2$SO$_4$	Sodium Sulfate
$^-$NCS	Thiocyanate
NEt$_3$	Triethylamine
NHC	Nitrogen Heterocyclic Carbene

NHE	Standard Hydrogen Electrode
NH$_4$OH	Ammonium Hydroxide
nm	Nanometers
NMR	Nuclear Magnetic Resonance
OTf	Triflate
PCET	Proton coupled electron transfer
Pd(PPh$_3$)$_4$	Palladium tetrakis triphenylphosphine
pKa	negative log of the acid dissociation constant
ppb	Parts per billion
PPh$_3$	Triphenylphosphine
ppm	Parts per million
py	pyridine
RC	Retention of Configuration
SCO	Spin Crossover
τ	Geometry Parameter
Bu$_4$NPF$_6$	Tetrabutylammonium hexafluorophosphate
THF	Tetrahydrofuran
TOF	Turnover Frequency
TON	Turnover Number
TW/h	Terawatt per hour
μL	microliter

UV-Vis	Ultra-violet visible spectroscopy
V	Potential
vs.	Versus
ν	Scan rate

ACKNOWLEDGEMENT

TABLE OF CONTENTS

LIST OF TABLES

LIST OF FIGURES

INTRODUCTION

Economic growth and an increasing global population continue to drive worldwide energy consumption to new heights.[1] Currently, this energy is largely sourced from fossil fuels (Figure 1),[2] whose combustion releases greenhouse gases and other airborne pollutants that are major contributors to climate change and human health concerns.[3] Hydrogen is a clean energy alternative to fossil fuels, which can be generated from solar-driven water splitting (Figure 2).[4] However, more efficient and inexpensive catalysts for the hydrogen evolution reaction (HER) are needed.[5]
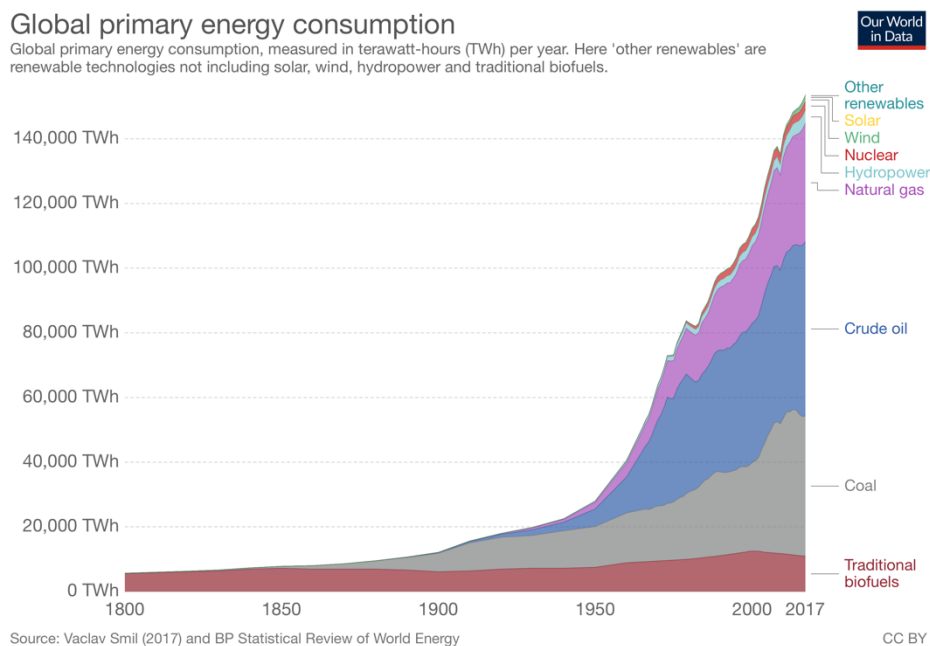
Figure 1. Global energy consumption from 1800 to 2017.[2]
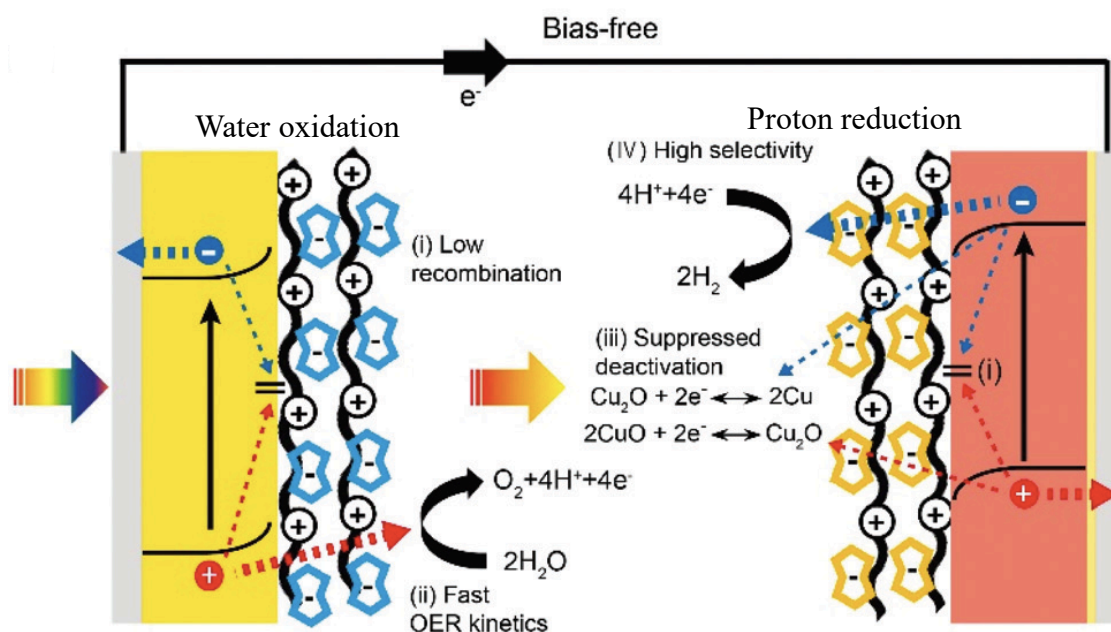
Figure 2. Solar-driven water splitting.[4]

Raw chemical feedstocks, such as petroleum and natural gas, are important sources of inexpensive hydrocarbons for the chemical and pharmaceutical industries. However, they have thermodynamically stable, kinetically inert C-H bonds which are not often viewed as chemical handles for further manipulation. A challenge lies in converting these readily available feedstocks into versatile organic building blocks in a mild and atom economical manner.[6] In this context, synthetic iron-oxo catalysts have been developed for reactions such as olefin epoxidation[7-9] and the hydroxylation of unactivated C-H bonds (Figure 3).[10-12] Circuitous synthetic routes engrossed in the maintenance and interconversion of functional groups throughout a reaction sequence can be avoided with catalysts capable of selective C-H bond functionalization.[12] Despite the remarkable progress that has been made to demonstrate the scope of chemistry available to synthetic nonheme iron-oxo catalysts,[10] significant improvements in catalyst selectivity and stability are needed to realize the full potential of these systems.[13]
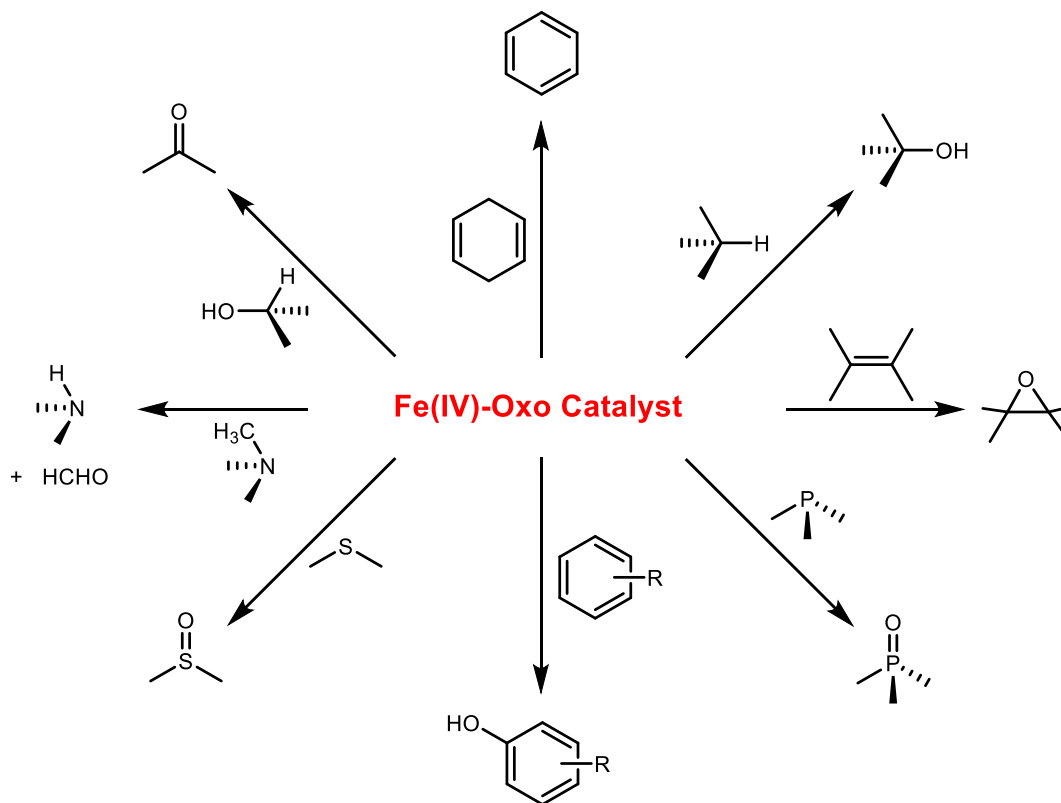
Figure 3. Oxidation reactions catalyzed by mononuclear non-heme iron(IV)-oxo complexes.

In this context, tetradentate and pentadentate ligand frameworks are important classes of ligands for accessing stable first-row transition metal complexes. The metal-ligand bonds of 3d metals are often labile and prone to substitution. Thus, highly chelating ligands are frequently employed to counter this characteristic while affording well-defined coordination spheres with tunable properties. Given the high denticity of these ligand classes, the number and relative orientation of labile coordination sites can be controlled, and specific geometries enforced, by clever ligand design in which preorganization, rigidity, and steric factors are useful strategies.[14,15]

Biphenyl-based polydentate ligands have been employed in a number of areas, including bioinorganic model compounds,[15-17] spin crossover complexes,[18] and homogeneous catalysis.[19] These systems exploit biphenyl as an unyielding structural unit whose substituted phenyl groups are not coplanar, allowing the appended donors to bind at a single metal center but with limited

flexibility. Octahedral Fe(II) compounds of general form $[FeL_6]^{2+}$ or $FeL_4(NCS)_2$ (where L is an N-heterocyclic donor such as pyridine) comprise the vast majority of known spin crossover (SCO) compounds, which hold great promise for applications such as data storage and molecular electronics.[20-23]

Indeed, when first-row transition metal complexes possess d^4 to d^7 electron configurations, the compounds can exist in a high spin (HS) or a low spin (LS) electronic state, which depends on the strength of ligand field as shown in Figure 4. If the complex as a strong field ligand, the metal usually exhibits a LS state because the energy required to pair electrons in the same orbital is less than the energy required to populate the e_g set of molecular orbitals. In contrast, with a weak field ligand, metal compounds generally favor a HS state, because the energy difference between the t_{2g} set and the e_g set of orbitals is less than the electron pairing energy. In addition, the spin state can also be interconvertible, where an external stimulation such as a change in temperature can cause a change in spin state. This often occurs when the energy difference between the low spin and high spin electronic states is small. This change in spin states is called spin crossover (SCO).

$$E$$

$$\Delta > P \qquad \Delta > P$$

$$(t_{2g})^4 (e_g)^2 \qquad (t_{2g})^6$$

Ligand field strength
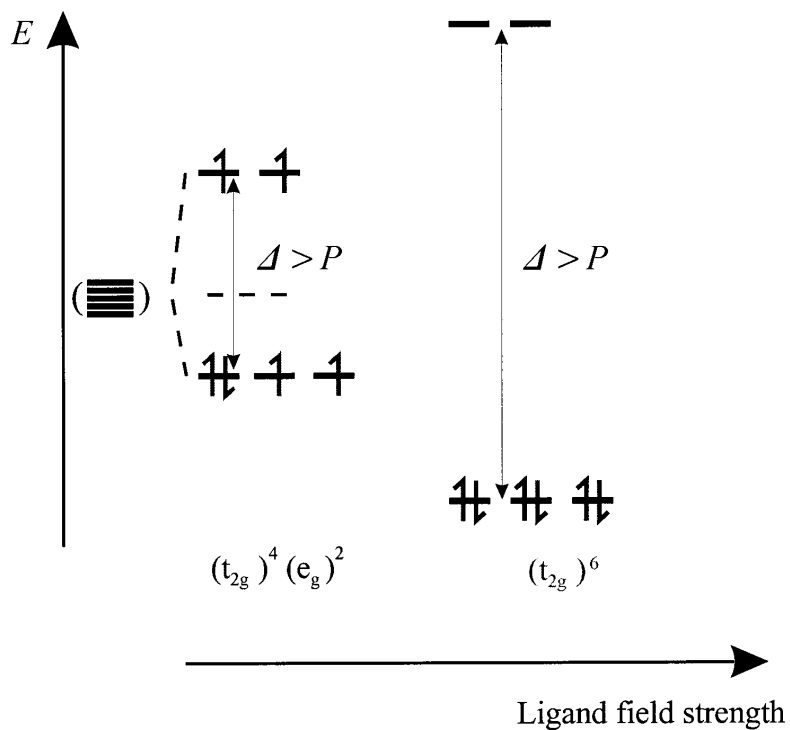
Figure 4. Electronic configuration for a d^6 iron(II) ion in the High Spin state (left) and the Low Spin state (right). Δ stands for the octahedral ligand field parameter and P stands for the mean spin-pairing energy.[21]

There are typically five types of SCO observed (Figure 5), which can be described as follows: a gradual change over a long temperature period (5a), a reversible and abrupt transition over a narrow temperature range (5b), a transition that features a thermal hysteresis loop (5c), a transition that is completed over two steps (5d), and an incomplete transition (5e). The type of spin transition that a compound exhibits is strongly affected by its interactions with neighboring molecules. In this context, SCO compounds are typically studied in the solid state where abrupt transitions between spin states can be observed.[20-23]
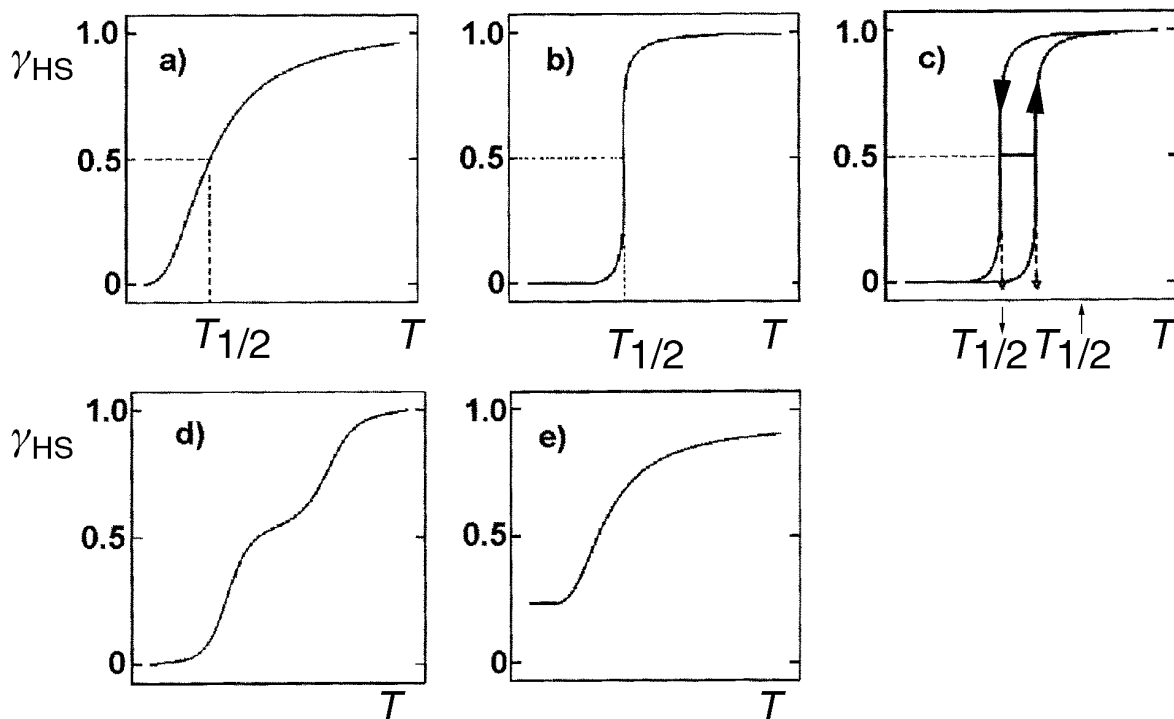
Figure 5. The nature of spin transition curves for spin crossover systems in the solid state: (a) gradual; (b) abrupt; (c) with hysteresis; (d) with steps; (e) incomplete.[21]

One strategy used to engender SCO behavior is the design of sterically demanding ligands that allow tuning of the metal-ligand bonding interactions to access complexes in which the ligand field strength and the spin-pairing energy are comparable.[24,25] This commonly manifests through added substituents at positions adjacent to the donor atoms (i.e. the 6 and 6' positions of 2,2'-bipyridine or the 2 and 9 positions of 1,10-phenanthroline).[26,27] In addition, the spin state of metal complexes has also been explored for its affect on the reactivity of compounds for reactions such as C-H bond oxidation where high spin iron-oxo complexes have significantly higher activity compared to their low spin counterparts.[47a] Thus, developing an understanding of how ligand structures affect the spin state of coordination compounds can allow the development of improved catalysts for C-H bond functionalization.

CHAPTER 1: Synthesis of a Pentadentate, Polypyrazine Ligand and its Application in Cobalt-Catalyzed Hydrogen Production

This project is also contributed by A. Khadivi and M. Singh for their work in synthesis and optimizing the synthetic route for the ligand .

Earth abundant cobalt polypyridyl complexes have garnered widespread attention as active and water compatible catalysts for the hydrogen evolution reaction (HER).[28] Recently, pyrazine-substituted cobalt polypyridyl complexes have been reported with ligand-centered redox activity and lower overpotentials for the two-electron reduction of water to H_2.[29] We sought to further these improvements in catalytic performance by developing an unprecedented pentadentate scaffold comprised entirely of pyrazine donors. The polypyrazine ligand reported here, 2,6-bis(1,1-di(pyrazin-2-yl)ethyl)pyrazine (PZ5Me$_2$), is a highly symmetric analogue of 2,6-bis(1,1-di(pyridin-2-yl)ethyl)pyridine (PY5Me$_2$).[30] PY5Me$_2$-type frameworks have shown exciting results in both oxidative and reductive catalysis with Mn,[31] Fe,[32] Co,[33] Ni,[34] Mo,[35] and Ru[36] metal centers. This class of ligands affords high stability and one labile coordination site for substrate activation and catalysis. Both PY5Me$_2$ and the pentapyrazine PZ5Me$_2$ derivative have C_{2v} symmetry and form well-defined pockets for metal binding (Figure 6). In addition, pyrazine is readily

reduced,[28,37] as it has a more positive gas phase electron affinity by 0.6 eV compared to pyridine,[38] and can serve as an electron reservoir to facilitate the multi electron conversion of protons to hydrogen.[29] While isostructural, pyrazine (pKa of conjugate acid = 0.37) has an extra nitrogen atom making it a less basic heterocycle than pyridine (pKa of conjugate acid = 5.14) and a weaker donor.[39] We reasoned that the chelate effect afforded by the pentadentate scaffold would provide sufficient metal complex stability and a more electropositive cobalt center for catalysis at a lower overpotential. To the best of our knowledge, PZ5Me$_2$ represents the first example of a pentadentate polypyrazine ligand. In fact, there are no reported tetradentate polypyrazine ligands (those containing only pyrazine donors) and even tridentate polypyrazine ligands are rare.[40] Herein, we describe the synthesis and characterization of a polypyrazine cobalt complex, [(PZ5Me$_2$)Co(OH$_2$)](OTf)$_2$ (where OTf is trifluoromethanesulfonate), and its application in electrocatalytic hydrogen production from aqueous protons at neutral pH.
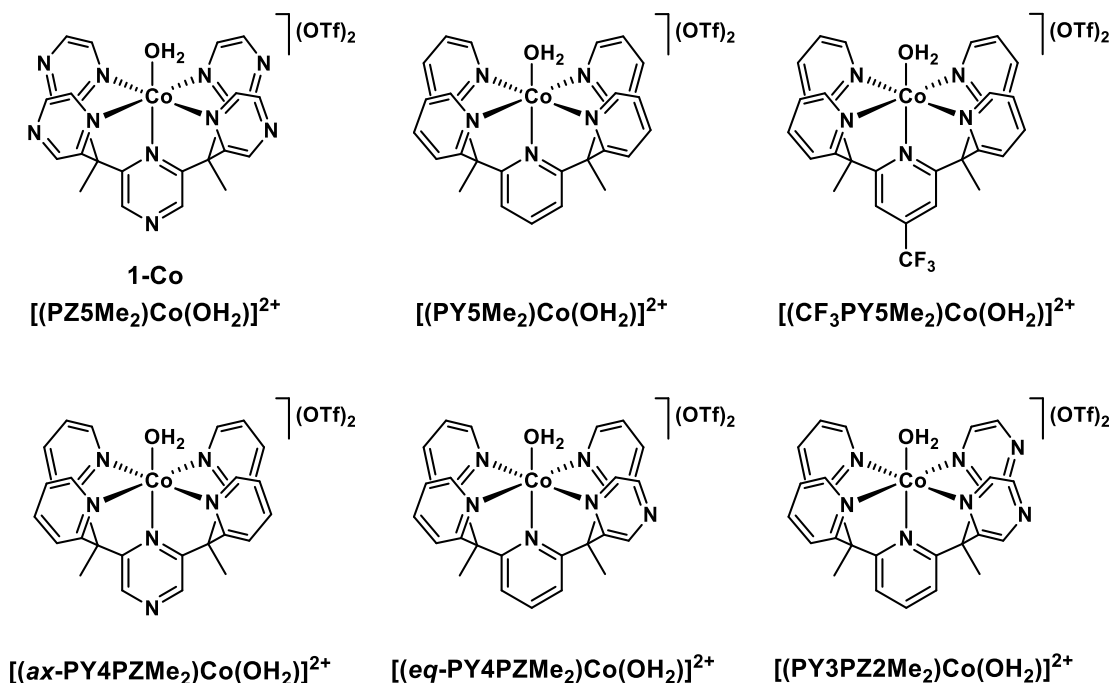
Figure 6. Line drawings of cobalt complexes with related PY5Me$_2$-type ligands and pyrazine-substituted derivatives including **1-Co**.

The 1,1'-dipyrazyl(ethane) precursor is prepared by lithiation of 2-ethylpyrazine and nucleophilic aromatic substitution with 2-chloropyrazine in refluxing THF, as previously reported.[5] Ligand synthesis and metalation are outlined in (Figure 7). Next, two equivalents of the dipyrazine arm are lithiated at the methine position and reacted with 2,6-dichloropyrazine to form the pentapyrazine framework **1**, PZ5Me$_2$, in 72% yield as a white solid. Lithium diisopropylamide (LDA) is required in these reactions as butyl addition to pyrazine rings was observed with *n*-butyllithium.[41] The ligand is dissolved in a 1:1 ratio with Co(CH$_3$CN)$_2$(OTf)$_2$ in a 9:1 acetone:water mixture and stirred at room temperature overnight under inert atmosphere. From a concentrated acetone solution, ether diffusion produces **1-Co**, [(PZ5Me$_2$)Co(OH$_2$)](OTf)$_2$, as a pure yellow precipitate in 60% yield. Upon redissolving in acetonitrile, slow evaporation affords golden shards suitable for X-ray diffraction. We note that the aquo species is retained following

9

recrystallization from acetonitrile solution (Figure 7). Attempts to synthesize the corresponding zinc complex to augment our investigation of ligand-based reductions were unsuccessful
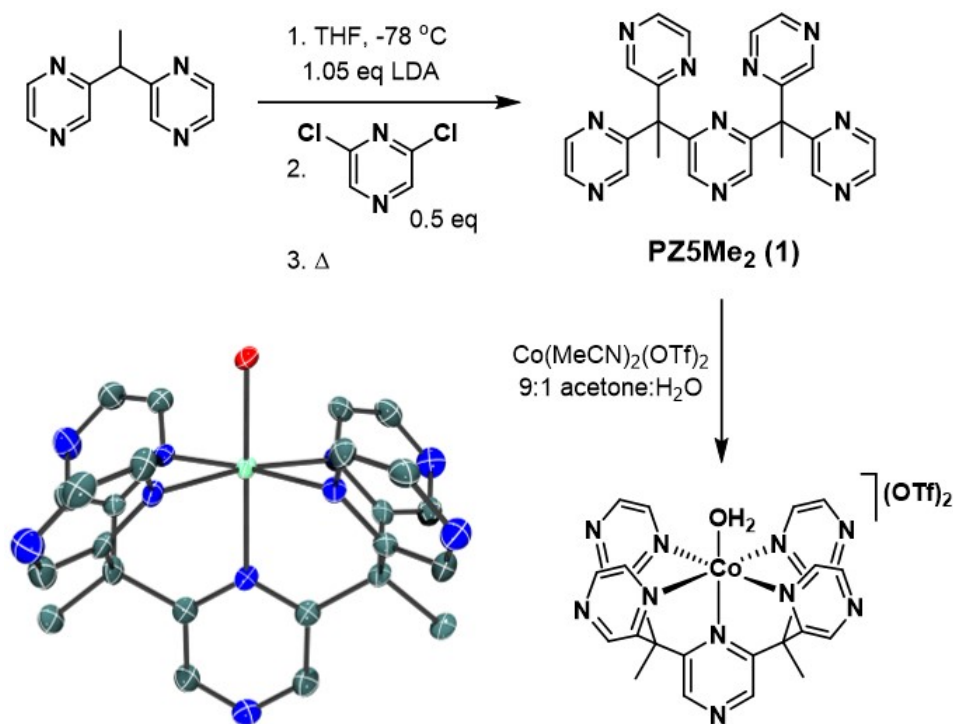
Figure 7. Synthesis of the Co complex and its crystal structure. Synthesis of the pentadentate PZ5Me$_2$ (1) scaffold and its Co(II)-OH$_2$ salt (**1-Co**), [(PZ5Me$_2$)Co(OH$_2$)](OTf)$_2$. Crystal structure of the cobalt ion; thermal ellipsoids are at the 70% probability level.

The complex **1-Co** is synthesized in a 9:1 acetone:water mixture to ensure that H$_2$O occupies the sixth coordination site. Selected bond distances of related Co(II) PY5Me$_2$-type complexes and pyrazine-substituted derivatives are tabulated in Table 1. Although pyrazine is a weaker sigma donor than pyridine, the average Co-N distance of **1-Co** is shorter relative to previously reported polypyridine analogues, indicating significant metal-to-ligand backbonding with the lower lying π^* orbitals of pyrazine. Similarly, the Co-O distance (2.010(4) Å) of the coordinated water is shorter by ≥ 0.04 Å in comparison to Co(II)-aquo PY5Me$_2$-derivatives.

Table 1. Selected Bond Distances of Cobalt Complexes with Related PY5Me$_2$-type Ligands and Pyrazine-Substituted Derivatives (illustrated in Figure 6 above).

Complex	Co-N$_{ax}$	Co-O	avg Co-N$_{eq}$
1-Co, [(PZ5Me$_2$)Co(OH$_2$)](OTf)$_2$ (this work)	2.103(5)	2.010(4)	2.127(5)
[(PY5Me$_2$)Co(OH$_2$)](OTf)$_2$ [21a]	2.103	2.055	2.139
[(CF$_3$PY5Me$_2$)Co(OH$_2$)](OTf)$_2$ [21a]	2.132	2.050	2.129
[(*ax*-PY4PZMe$_2$)Co(OH$_2$)](OTf)$_2$ [17]	2.105	2.034	2.142
[(*eq*-PY4PZMe$_2$)Co(OH$_2$)](OTf)$_2$ [17]	2.099	2.032	2.127
[(PY3PZ2Me$_2$)Co(OH$_2$)](OTf)$_2$ [17]	2.094	2.016	2.113

Cyclic voltammetry studies of both the free ligand and **1-Co** were conducted in anhydrous acetonitrile. Irreversible reductions of PZ5Me$_2$, **1**, begin at -2.22 V vs Fc$^+$/Fc (Appendix Figure 36). Notably, pyrazine-substituted PY5Me$_2$ derivatives did not show redox activity when scanned to -2.3 V under the same conditions.[29] The Co complex exhibits three well-defined redox waves at 0.55 V, -0.90 V, and -1.76 V (Figure 8A). Its scan rate dependence confirms the species is diffusion controlled (Appendix Figures 37, 38). However, the last reduction features a sharp return oxidation consistent with reversible adsorption to the electrode surface (Appendix Figure 39). We first sought to determine the ligand identity at the labile coordination site by metalation of **1** with Co(CH$_3$CN)$_2$(OTf)$_2$ in anhydrous acetonitrile. Cyclic voltammetry of the crude product in 0.1 M Bu$_4$NPF$_6$ CH$_3$CN produced three nearly identical redox features by both shape and potential (Appendix Figure 40) indicating exchange of the aquo ligand of **1-Co** occurs in acetonitrile solution. Square wave voltammetry was then performed to quantify the number of electrons involved in each redox process (Figure 8A). The integrated peak areas under non-catalytic conditions suggest that each wave corresponds to a 1-electron redox event (Figure 8A). However, given the lower peak area for the most positive wave, assigned to a Co(III/II) couple which are

often quasireversible,[33,42] the electron stoichiometry was also evaluated by controlled potential electrolysis in a thin-layer cell calibrated with $Co(bpy)_3^{2+}$ (bpy is 2,2'-bipyridine), which confirmed the 1-electron designations. Accordingly, in 0.1 M KNO$_3$ aqueous solution, waves at 0.55 V and -0.53 V vs NHE are ascribed to 1-electron events followed by a catalytic reduction at -0.8 V (Figure 8B). We assign the most positive waves in Figure 8 to the Co(III/II) couple followed first by a one-electron wave comprising the Co(II/I) couple and then a ligand-centered redox process on the basis of previous assignments of pyrazine-substituted PY5Me$_2$-type cobalt complexes.[29] The more electropositive cobalt center in **1-Co** is reflected in the more positive potentials of its Co(III/II) and Co(II/I) couples relative to previously reported pentadentate Co(II) complexes, Table 2, in acetonitrile. Notably, the complexes listed in Table 2 denote the isolated complex used to prepare the solutions for electrochemistry. Displacement of the coordinated water by acetonitrile was observed in each of the Co-OH$_2$ species listed.[29]
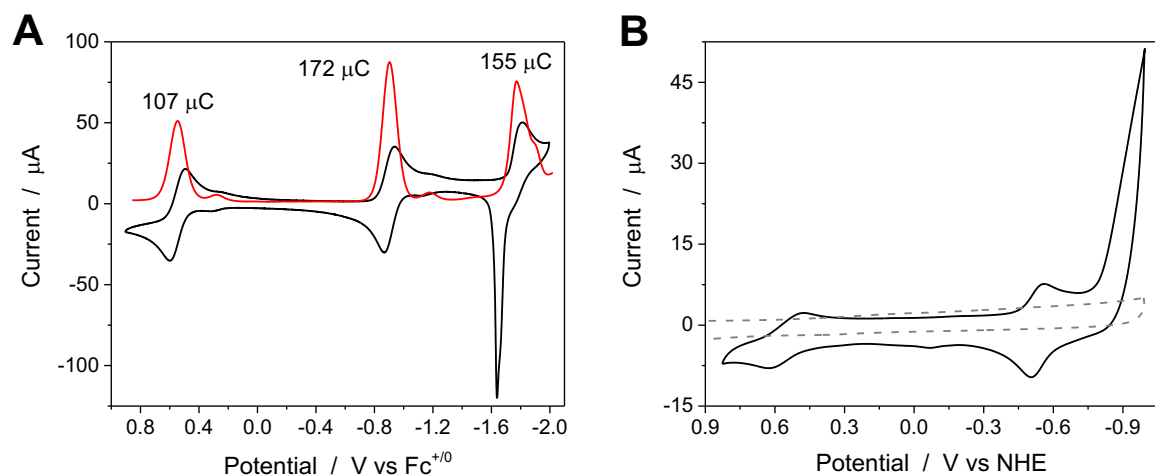
Figure 8. Cyclic voltammograms with an overlaid square wave voltammogram showing integrated peak area in μC. **A)** 2 mM $[(PZ5Me_2)Co(CH_3CN)]^{2+}$ in 0.1 M Bu_4NPF_6 CH_3CN. **B)** 1 mM **1-Co** in 0.1 M KNO_3 aqueous solution; background displayed as gray dashed line. *Conditions:* glassy carbon electrode (3 mm dia.) and 100 mV/s scan rate.

Table 2. Electrochemical potentials (V vs Fc^+/Fc) for related Co complexes (in acetonitrile/0.1 M Bu_4NPF_6).

Complex	Co(III/II)	$E_{p1,c}$	$E_{p2,c}$
1-Co, $[(PZ5Me_2)Co(OH_2)](OTf)_2$	0.55	-0.90	-1.76
$[(PY5Me_2)Co(CH_3CN)](OTf)_2$ [21a]	0.24	-1.47	-2.36
$[(CF_3PY5Me_2)Co(CH_3CN)](OTf)_2$ [21a]	0.34	-1.28	-2.21
$[(ax\text{-}PY4PZMe_2)Co(OH_2)](OTf)_2$ [17]	0.32	-1.22	-1.40
$[(eq\text{-}PY4PZMe_2)Co(OH_2)](OTf)_2$ [17]	0.27	-1.30	-1.42[a]
$[(PY3PZ2Me_2)Co(OH_2)](OTf)_2$ [17]	0.35	-1.18	-1.25[b]

a. Has third reduction, $E_{p3,c}$ at -2.04 V;[17] b. Has third reduction, $E_{p3,c}$ at -1.95 V.[17]

Aqueous electrochemistry of **1-Co** was performed to investigate catalysis as a function of pH (Figure 9). A series of pH dependent cyclic voltammograms of the first reduction are shown in Figure 9A. The corresponding $E_{1/2}$-pH plot exhibits a slope of 60 mV/pH unit, consistent with a 1 $e^-/1H^+$ process (Appendix Figure 41). At more negative potentials, catalytic waves are evident. With decreasing acidity the onset of catalysis becomes increasingly more negative than the first reduction. Scan rate dependent cyclic voltammetry of **1-Co** at pH 7 confirms that the catalyst is diffusion controlled under these conditions (Appendix Figure 42).

Insight into catalyst stability is also apparent under these conditions. Successive cyclic voltammograms overlay in pH 7 potassium hydrogen phthalate (KHP) buffer solutions, but lower current is observed in subsequent cycles at pH 3, such that the characteristic redox features are lost (Appendix Figure 43). Presumably, the ligand is protonated off the reduced metal center following ligand-centered reduction in acidic aqueous media. In agreement with reductive ligand dissociation in acidic pH, the catalyst is indefinitely stable in the 2+ oxidation state and to oxidative scans generating Co(III) as demonstrated by repeated and overlaying cycles in pH 2.5 phosphate buffer (Appendix Figure 44). A reversible Co(III/II) couple with $E_{1/2}$ of 0.86 V vs NHE is observed. For comparison, the same couple at pH 2.5 for the cobalt polypyridine complex $[(PY5)Co(OH_2)](ClO_4)_2$ occurs at 0.73 V.[43]
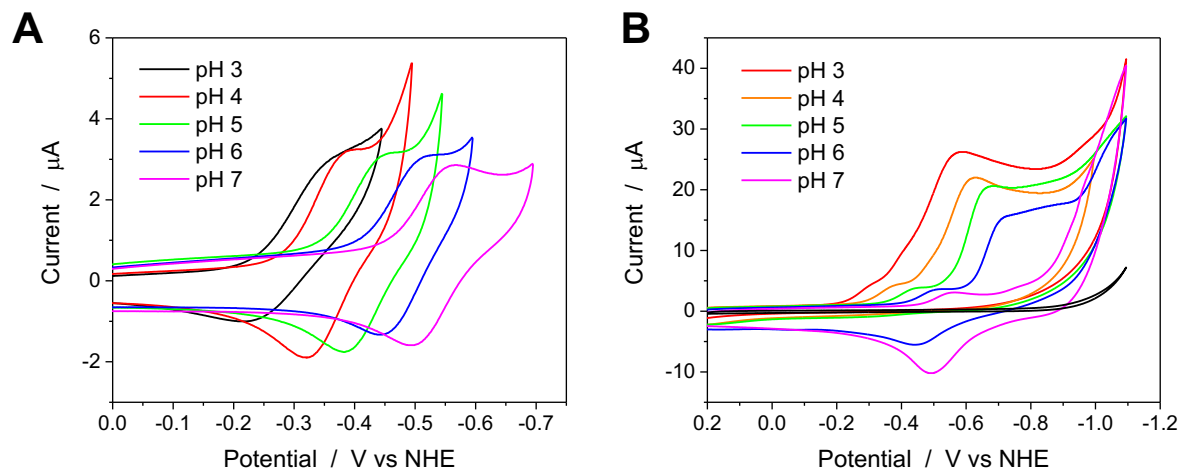
Figure 9. Aqueous cyclic voltammetry of **1-Co. A)** $E_{1/2}$ vs pH for first quasi-reversible reduction. **B)** Catalytic wave. *Conditions:* 1 mM complex, KHP buffer, glassy carbon electrode (3 mm dia).

Given the reductive stability of **1-Co** at neutral pH, controlled potential electrolyses for electrocatalytic hydrogen evolution were carried out at pH 7 in a two-compartment electrochemical cell with a mercury pool working electrode to establish the Faradaic efficiency. Due to the relatively low concentrations that are accessible with KHP buffer, electrolyses and addition electrochemical studies were performed in 1 M pH 7 phosphate buffer for higher buffer capacity. Cyclic voltammetry of **1-Co** at the Hg pool electrode shows considerable activity with respect to the background (Figure 10A). For comparison, a CV of the polypyridine analogue $[(H_2O)Co(PY5Me_2)](OTf)_2$ is also shown under the same conditions. Evolved hydrogen was quantified by periodic analysis of headspace samples using gas chromatography over a 2-hour controlled potential electrolysis with an applied potential of -1.3 V vs NHE (Figure 10B), revealing near quantitative Faradaic efficiency for H_2 generation. The corresponding current vs time plot (Appendix Figure 45) shows steady catalysis and provides evidence for high catalyst stability. Similar observations were made at a more negative applied voltage with significantly

15

faster charge accumulation (Appendix Figure 46). The overpotential for catalysis with **1-Co** is *ca.* 560 mV at pH 7 on a Hg pool electrode, or 100 mV more positive relative to $[(H_2O)Co(PY5Me_2)](OTf)_2$,[33a] as established by comparing accumulated charge in a series of short electrolyses with increasing voltages (Appendix Figures 47, 48). A lower-limit turnover frequency (TOF) of 0.14 s^{-1} was determined with 10 μM catalyst at an applied potential of -1.3 V.
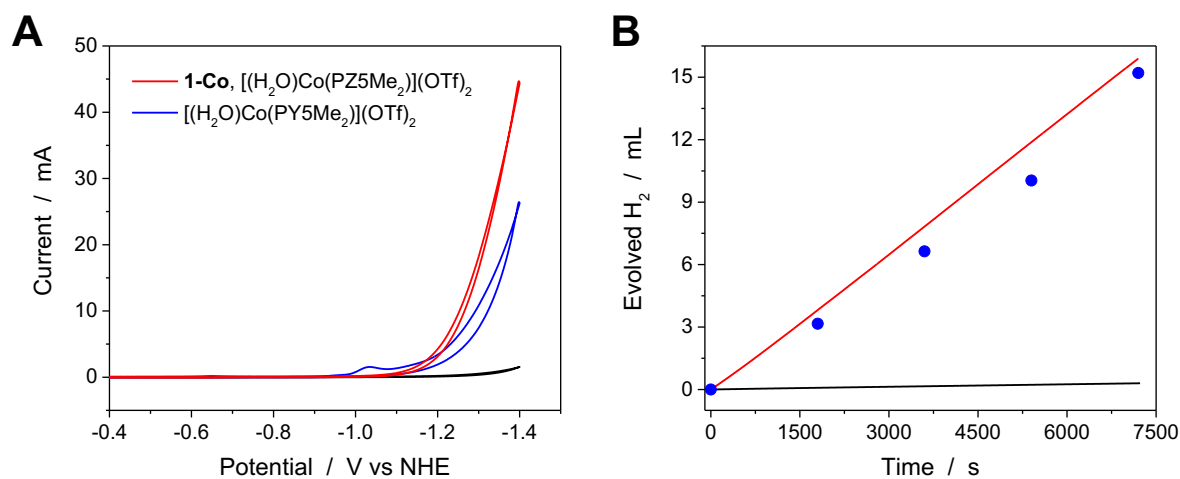
Figure 10. Electrochemistry in 1 M pH 7 phosphate buffer on Hg pool electrode (A = 12.57 cm^2). **A)** Cyclic voltammograms of 10 μM **1-Co** and 10 μM $[(H_2O)Co(PY5Me_2)](OTf)_2$ at ν = 100 mV/s. **B)** Controlled potential electrolyses with (red) and without (black) 10 μM **1-Co** at an applied potential of -1.3 V vs NHE. The maximum theoretical H_2 produced is plotted (line) from accumulated charge. Circles are quantified H_2 from the headspace. Background measurements are shown in black.

Next, we sought to determine the reaction order with respect to **1-Co** during electrocatalytic proton reduction. A series of cyclic voltammograms were obtained with **1-Co** at a Hg pool working electrode (Appendix Figure 49) in which the concentration of catalyst was varied incrementally. From these results, catalytic current was plotted versus [**1-Co**], producing a straight line that

demonstrates a first order dependence on catalyst (Figure 11A). A first order dependence on catalyst concentration was also observed with a glassy carbon working electrode (Appendix Figure 50). In addition, overlaid current-potential profiles for **1-Co** and $[(H_2O)Co(PY5Me_2)](OTf)_2$ using a glassy carbon working electrode are shown in Figure 11B, consistent with CVs obtained of each catalyst on a Hg pool working electrode (Figure 8A), where a lower overpotential for catalysis is observed with the $PZ5Me_2$ derivative.
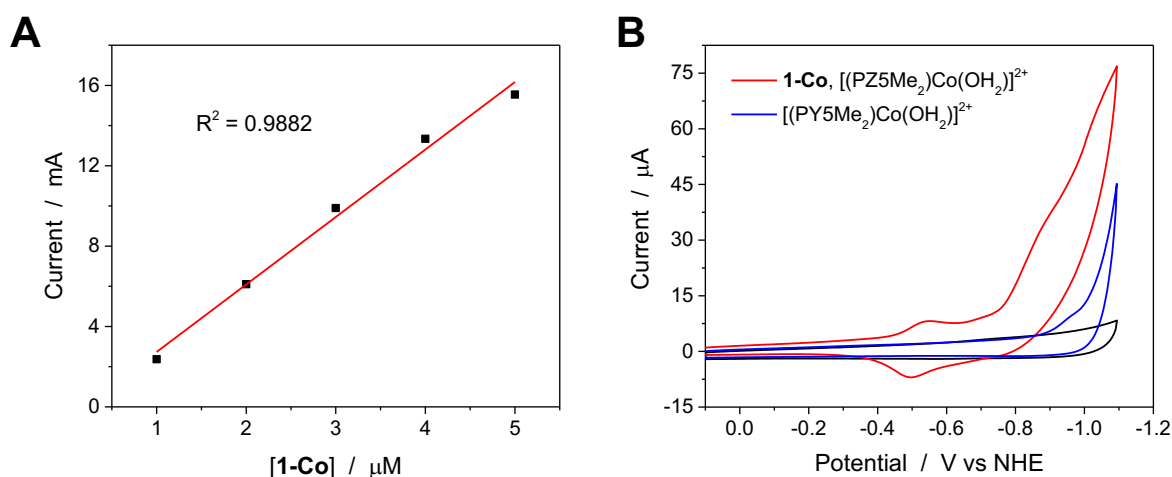
Figure 11. Plot of concentration dependence and CVs for 1-Co. **A)** Catalytic current at -1.30 V vs catalyst concentration [**1-Co**] from CVs (Figure 50) in 1 M pH 7 phosphate buffer, Hg pool electrode, ν = 100 mV/s. B) Cyclic voltammograms of **1-Co** (red) and $[(H_2O)Co(PY5Me_2)](OTf)_2$ (blue) in pH 7 KHP buffer, 1 mM catalyst concentrations, glassy carbon electrode, ν = 100 mV/s. Background is shown in black.

The general mechanism for proton reduction to hydrogen by molecular cobalt catalysts involves initial reduction of the Co(II) species to Co(I) followed by protonation to form a Co(III)-hydride intermediate.[5,44] Subsequent H_2 generation typically occurs through one of two pathways: a heterolytic pathway involving one metal center or by a homolytic pathway involving two metal

centers.[5,44] Formation of the Co(III)-H is a critical step. Given the redox-active PZ5Me$_2$ framework, the description of putative intermediates and their formal oxidation states during catalysis with **1-Co** is unclear. The ligand-centered reduction following the Co(II/I) couple may allow formation of a Co(II)-H intermediate upon protonation of the metal center. However, in the event that the reduced pyrazine acts as a spectator, or uncooperative electron sink, the ligand-centered reduction should serve at a minimum to provide a more electron-rich donor to facilitate protonation at the otherwise electropositive cobalt center (based on Co(III/II) and Co(II/I) redox potentials).

Experimental procedures.

2,6-bis(1,1-di(pyrazin-2-yl)ethyl)pyrazine, (PZ5Me$_2$, 1): Under nitrogen atmosphere, 50 mL of anhydrous tetrahydrofuran was added to 1,1'-dipyrazyl(ethane) (3.8 g, 20.4 mmol) in an oven-dried 2-neck round bottom flask equipped with stir bar and reflux condenser. The reaction vessel was then cooled to -78 °C using a dry ice/acetone bath. A 2.0 M solution of LDA (1 eq, 20.4 mmol, 10.2 mL) was added *via* syringe to the stirred solution before allowing it to warm slowly to room temperature. Next, 2,6-dichloropyrazine (0.33 eq, 1.01 g, 6.8 mmol) was added to the red reaction mixture and set to reflux at 85 °C for 2 days. After cooling to room temperature, the unreacted LDA was quenched with ice, and organics were extracted with diethyl ether (1X), then dichloromethane (2X). The extract was dried over anhydrous sodium sulfate, and the solvent was subsequently removed by rotary evaporation. Purification was achieved by silica gel chromatography to give a white powder (2.06 g) in 68% yield. ^{1}H NMR (CDCl$_3$, 500 MHz): δ 8.48 (6H, m), 8.43 (4H, br), 8.30 (4H, br s), 2.25 (6H, s). ^{13}C NMR (CDCl$_3$, 125 MHz): δ 159.43 (s), 157.91 (s), 145.10 (s), 143.45 (s), 142.68 (s), 142.05 (s), 56.30 (s), 25.84 (s). HR-ESI-MS (M$^+$) m/z calc. [**1** + H$^+$], 449.1945, found, 449.1946.

[(PZ5Me₂)Co(OH₂)](OTf)₂, (1-Co): To a 20 mL scintillation vial was added 0.1 g (0.223 mmol) of PZ5Me₂ (**1**) along with 1 equivalent of $Co(CH_3CN)_2(OTf)_2$ (0.098 g, 0.223 mmol), which was stored inside of a glove box. Then, 5 mL of a 9:1 acetone:H_2O mixture was added to the vial and the reaction was stirred overnight at room temperature under N_2. The reaction mixture was taken to dryness and re-dissolved in acetone. Ether diffusion affords a pure yellow precipitate in 76% yield (0.140 g). X-ray quality crystals (golden shards) of the complex were grown from slow evaporation of a concentrated acetonitrile solution. Elem. Anal. calc. for $C_{26}H_{22}CoF_6N_{10}O_7S_2$: C, 37.92; H, 2.69; N, 17.01. Found: C, 37.94; H, 2.94; N, 16.99. HR-ESI-MS (M⁺) m/z calc. [(PZ5Me₂)Co(OTf)⁺], 656.0719, found, 656.0714; m/z calc. [(PZ5Me₂)Co²⁺], 253.5597, found, 253.5596.

Conclusions.

A novel pentapyrazine ligand scaffold, a first of its kind, has been developed and applied to cobalt-catalyzed hydrogen evolution from aqueous protons. The C_{2v} symmetric pentadentate ligand affords good stability for electrocatalytic hydrogen production over multiple hours at neutral pH with a measured Faradaic efficiency of nearly 100% for evolved hydrogen. A lower overpotential for catalysis is also observed for **1-Co** in comparison to its polypyridine predecessor. Indeed, the redox potentials of **1-Co** are consistent with a more electron-deficient cobalt centre relative to previous systems based on PY5Me₂. Indeed, the PZ5Me₂ framework provides a structural homologue to PY5Me₂ with considerably different electronics while maintaining a labile coordination site for metal-mediated reactivity.

CHAPTER 2: Selective Alkane C-H Bond Oxidation Catalyzed by a Nonheme Iron Complex Featuring a Robust Tetradentate Ligand

Adapted with the permission from **L. Chen**, X.-J. Su, J. W. Jurss,

Organometallics. **2018**, 37, 4535. Copyright (2019) American Chemical Society.

(see appendix for permission license)

This project is contributed by Xiaojun Su for his work in study the A/K ratios for cyclohexane and Fe-Oxo characterization.

Notably, iron-oxo complexes are capable of catalyzing *N*-dealkylation reactions,[45] which has particular relevance to catalyst stability as the majority of nonheme Fe-oxo catalysts employ alkylamine-type ligands. Prominent iron-based catalysts of this ilk are shown in Figure 12. Amine-based ligands are convenient to synthesize by S_N2 reactions, but are vulnerable to oxidative decomposition.[45,46] Likewise, C-H bonds of the ligand can also be oxidized through both inter- and intramolecular pathways.[46,47] De-metalation and individual donor dissociation from iron have also been observed with the flexible, polydentate ligands that are commonly used.[48,49]
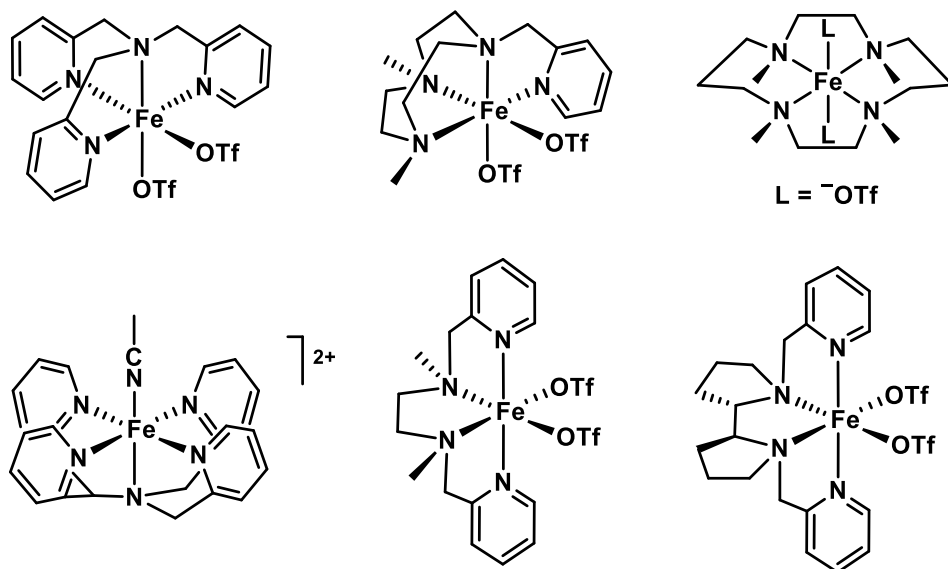
Figure 12. Representative nonheme iron complexes for C-H bond oxidation bearing alkylamine-type N-donor ligands.

Beyond stability, metal coordination geometry is another important factor as many of the champion iron catalysts applied to hydrocarbon oxidation feature *cis*-labile coordination sites.[50] The increased activity and selectivity observed with these catalysts is thought to arise from cooperativity between the adjacent sites as proposed in water- or acetic acid-assisted mechanisms for alkane oxidation.[12,51] It is worth noting that nonheme iron oxygenases also possess this structural motif.[51] While the protein environment around metalloenzyme active sites serves, in part, to protect the active site from degradation, synthetic catalysts do not have the luxury of a tightly controlled surrounding and must be designed to withstand the harsh oxidizing conditions of the reaction medium. Thus, we have turned our attention toward more rigid, preorganized frameworks devoid of weak C-H bonds and alkylamine-type donors as a starting point to enforcing desired active site configurations and improved catalyst stability.

Herein we report an iron(II) complex, [Fe^{II}(BpyPY2Me)(CH$_3$CN)$_2$](OTf)$_2$ (**1-Fe**, BpyPY2Me = 6-(1,1-di(pyridin-2-yl)ethyl)-2,2'-bipyridine, OTf = triflate), supported by an

21

oxidatively-rugged tetradentate scaffold that aims to minimize oxidative ligand decomposition while providing *cis*-labile coordination sites at the iron center. Literature procedures were followed to prepare BpyPY2Me.[21f] Complex **1-Fe** was prepared by reacting BpyPY2Me with 1 equivalent of Fe(OTf)$_2$ in methanol. The complex was subsequently crystallized from acetonitrile by diethyl ether diffusion and structurally characterized (Figure 13) by single-crystal X-ray crystallography. Selected bond lengths, provided in the caption, and the diamagnetic ^{1}H and ^{13}C NMR spectra of **1-Fe** are consistent with a low-spin iron(II) complex (Appendix Figures 51, 52).
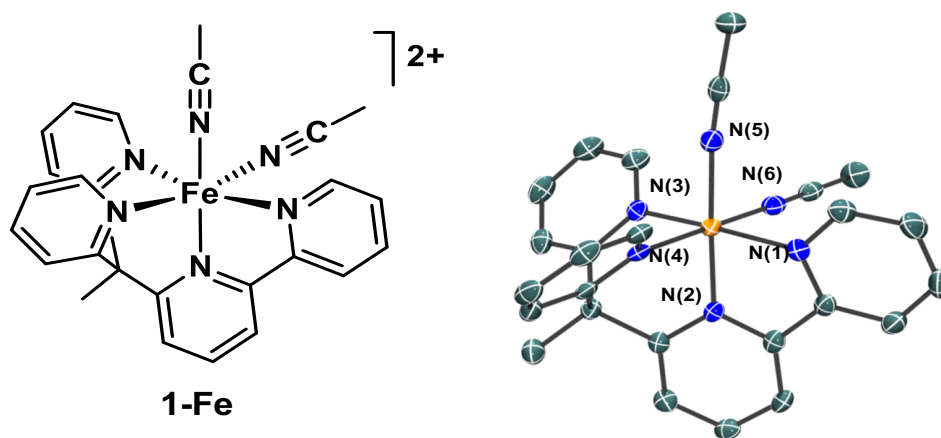
Figure 13. Curystal structure of the cation of [1-Fe](OTf)2 with thermal ellipsoids rendered at the 70% probability level. Hydrogen atoms have been omitted for clarity. Selected bond distances: Fe-N(1): 1.9948(19); Fe-N(2): 1.9054(19); Fe-N(3): 1.9691(19); Fe-N(4): 1.9509(19); Fe-N(5): 1.951(2); Fe-N(6): 1.950(2) Å.

With the addition of one equivalent of *m*-chloroperbenzoic acid (*m*CPBA) into the CH$_3$CN solution containing 1 mM **1-Fe**, the initial absorption at λ = 486 nm (ε = 2700 M^{-1}cm^{-1}) gives way to a new broad absorption band centered at 739 nm (ε ~ 100 M^{-1}cm^{-1}), a characteristic absorption feature of known Fe-oxo complexes (Figure 14).[40] High resolution electrospray ionization mass spectrometry (ESI-MS) confirmed its identity as a high-valent, molecular iron(IV)-oxo species

(Appendix Figure 53). A paramagnetic ^{1}H NMR spectrum was also obtained of the iron-oxo complex with proton signals spanning a range of 54 ppm (Appendix Figure 54). This intermediate is relatively stable ($t_{1/2} \sim 30$ min at 23 °C; Figures 15, 16) when monitoring self-degradation by the decrease in absorbance at 739 nm. We note that H_2O_2 addition to solutions of **1-Fe** did not generate the near-IR absorption band, which suggests that H_2O_2 is not a strong enough oxidant to form an iron-oxo species from **1-Fe**.
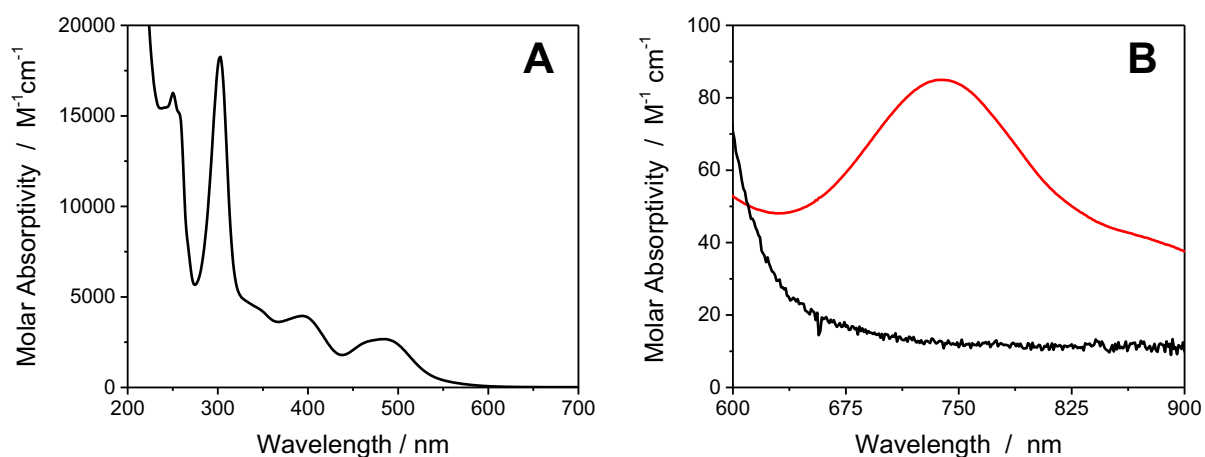
Figure 14. UV-vis spectra of **1-Fe** and iron(IV)-oxo intermediate. **A)** **1-Fe** (black) in anhydrous acetonitrile (λ_{max} = 250 nm (ε = 1.6×10^4 $M^{-1}cm^{-1}$), 302 nm (1.8×10^4 $M^{-1}cm^{-1}$), 395 nm (3.9×10^3 $M^{-1}cm^{-1}$), and 486 nm (2.7×10^3 $M^{-1}cm^{-1}$), and **B)** the iron(IV)-oxo intermediate (red) formed by adding 1 equivalent of *m*CPBA.
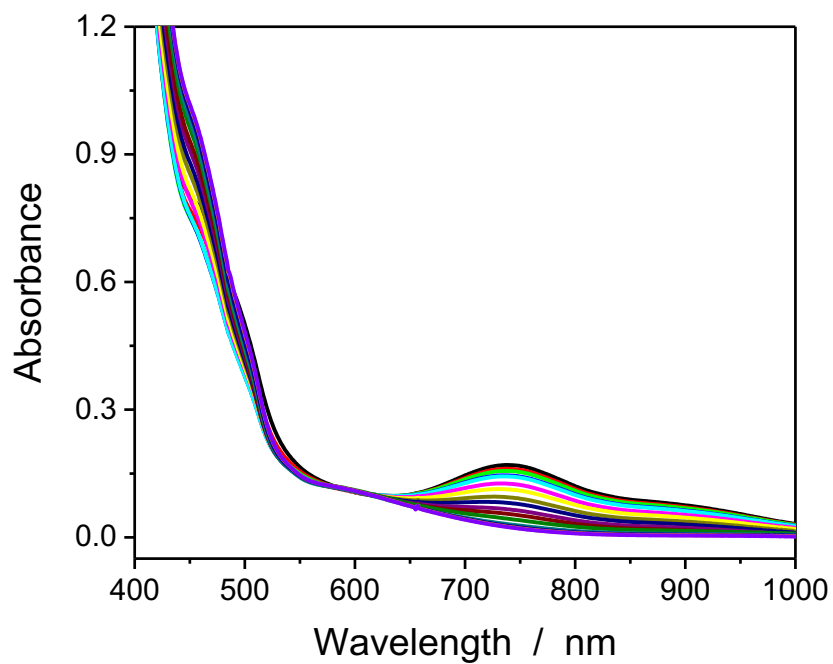
Figure 15. Decay of the iron(IV)-oxo intermediate. UV-vis spectra recorded every 10 s to follow decay of the iron(IV)-oxo intermediate generated by adding 1 equivalent of *m*CPBA to 2 mM **1-Fe** in CH₃CN.
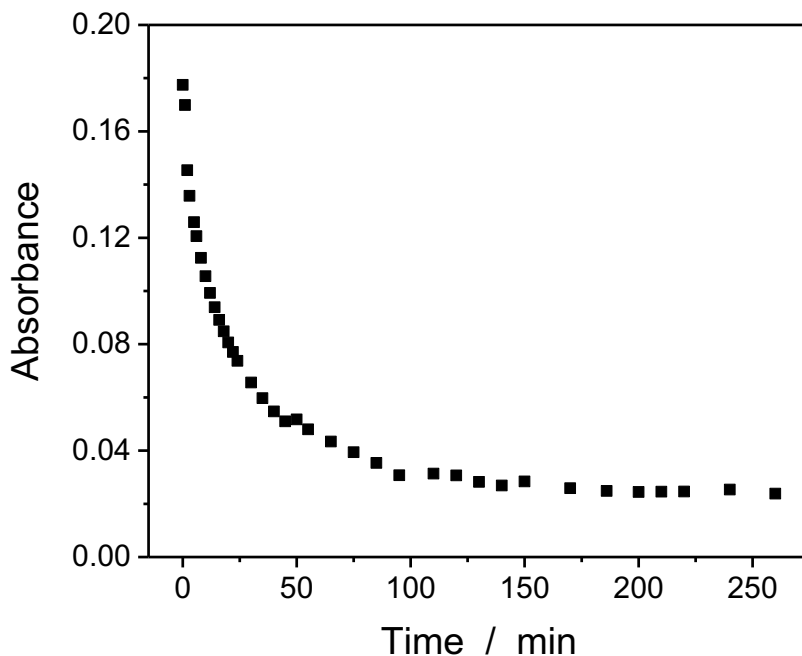
Figure 16. Plot of the decay of iron(IV)-oxo intermediate. absorbance at λ_{max} = 739 nm as a function of time from the data shown in Figure 15. Spectra were recorded at 10 s intervals.

Cyclic voltammetry (CV) of **1-Fe** was performed in CH$_3$CN solutions containing 0.1 M LiClO$_4$ as the supporting electrolyte (Figure 17). All reported potentials are referenced to the ferrocenium/ferrocene couple (Fc$^{+/0}$). In anhydrous CH$_3$CN, **1-Fe** undergoes a reversible (ΔE_p = 69 mV) one-electron redox process at $E_{1/2}$ = 0.89 V, consistent with an Fe^{III}(CH$_3$CN)$_2$/Fe^{II}(CH$_3$CN)$_2$ couple. No additional waves were observed when scanning to more positive voltages. At negative potentials, two quasi-reversible, overlapping reductions are found at $E_{p,c}$ = -1.66 and -1.83 V, which we assign to ligand-based reductions based on the CV of a reported Zn(II) complex bearing a very similar ligand that exhibits two closely-spaced reductions at similar potentials.[42b]
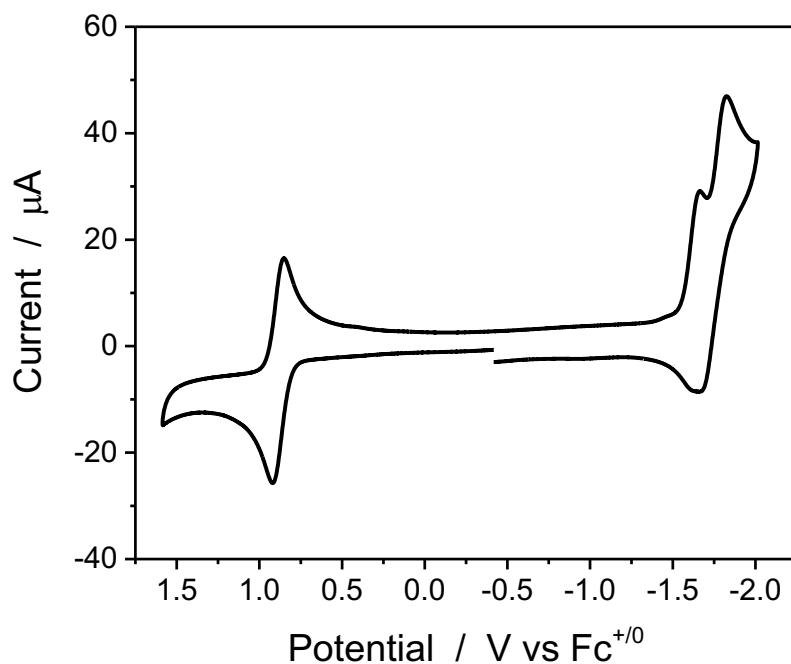
Figure 17. Cyclic voltammogram of 1 mM **1-Fe**. in anhydrous CH_3CN / 0.1 M $LiClO_4$ under N_2 atmosphere (v = 100 mV/s, glassy carbon disk).

Since **1-Fe** can be oxidized with *m*CPBA to generate an iron-oxo complex, its application as a catalyst for cyclohexane C-H bond oxidation was investigated (Appendix Figure 55). The ratio of cyclohexanol-to-cyclohexanone, i.e. the alcohol-to-ketone (A/K) ratio, has been used to differentiate between a likely radical-based mechanism or a metal-centered oxidation process.[6] The so-called radical mechanism typically proceeds through a long-lived radical formed *via* Fenton-type chemistry in which the oxidant, i.e. peroxide, is decomposed into radicals that oxidize the substrate directly. In this case, the cyclohexyl radical is susceptible to reactivity with O_2 to form cyclohexyl peroxide, which exhibits low selectivity in decomposing to equivalent amounts of cyclohexanol and cyclohexanone (with an A/K ratio of ~1). However, metal-centered C-H bond oxidations are often characterized by short radical lifetimes that allow higher A/K product ratios

and greater selectivity.[6] Here, a transient substrate radical is formed by H atom abstraction by the Fe-oxo catalyst and rebounds with the resulting Fe-OH species to form the C-O bond of the product.

All reactions were conducted in CH_3CN at room temperature with a large excess of substrate to avoid over-oxidation of cyclohexanol (A) to cyclohexanone (K). Catalytic reactions were repeated in triplicate, and products were quantified by gas chromatography. The conversion percentages with respect to oxidant, taking the reaction stoichiometry into account (A + 2K), are presented in Table 3. The results show that cyclohexanol is the main product for all entries. When using 10 equivalents of *m*CPBA and 1000 equivalents of cyclohexane, the highest conversion yield of 90% and largest A/K ratio (7.5) are observed, consistent with a metal-centered oxidation mechanism.[6] A small increase in the A/K ratio to 9 was observed in experiments conducted in the absence of O_2. In addition, a series of reactions were quenched with triphenylphosphine at different time points following the addition of *m*CPBA to measure the A/K ratio as a function of time. The A/K ratios are largely unaffected by the reaction time (Figure 18).

Table 3. Cyclohexane oxidation with *m*CPBA catalyzed by **1-Fe**.

Entry	1-Fe:*m*CPBA:substrate	A/K[a]	Overall Yield (%)[b]
1	1:10:100	2.5	48
2	1:10:500	5.6	79
3	1:10:800	5.8	80
4	1:10:1000	7.5	90
5	1:20:100	1.4	48
6	1:20:500	3.8	78
7	1:20:800	3.9	80
8	1:20:1000	4.8	84

Conditions: 1 mM **1-Fe**, 3 mL total volume. [a]moles of cyclohexanol / moles of cyclohexanone. [b]Yield with respect to *m*CPBA.

27
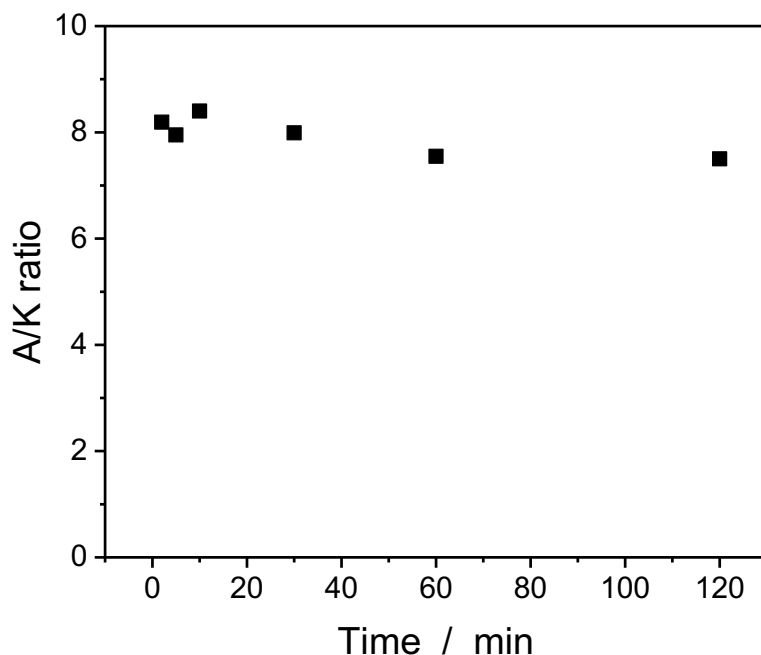
Figure 18. Time dependence of alcohol-to-ketone (A/K) ratios. A plot of alcohol-to-ketone (A/K) ratios measured for a series of reactions involving 1 mM **1-Fe**, 10 equivalents *m*CPBA, and 1000 equivalents cyclohexane that were quenched at different time points with excess triphenylphosphine.

Reaction kinetics for cyclohexane oxidation were also analyzed by monitoring the decay of the pre-formed Fe(IV)-oxo intermediate upon addition of different amounts of substrate (Figure 19). Pseudo-first-order rate constants (k_{obs}) were determined by fitting the kinetic traces, and were found to increase linearly with increasing cyclohexane concentration (Figure 20). From the slope of this plot, a second-order rate constant (k_2) of 1.4×10^{-2} M^{-1}s^{-1} at 23 °C was obtained. Using various ratios of cyclohexane to d_{12}-cyclohexane (Appendix Figure 56), a kinetic isotope effect (KIE) of 3.2 was calculated (Figure 21) in experiments carried out under the same conditions as Entry 4 of Table 3. The KIE value as well as the A/K ratios measured with **1-Fe** are similar to reported values for known nonheme iron-oxo complexes.[50a]
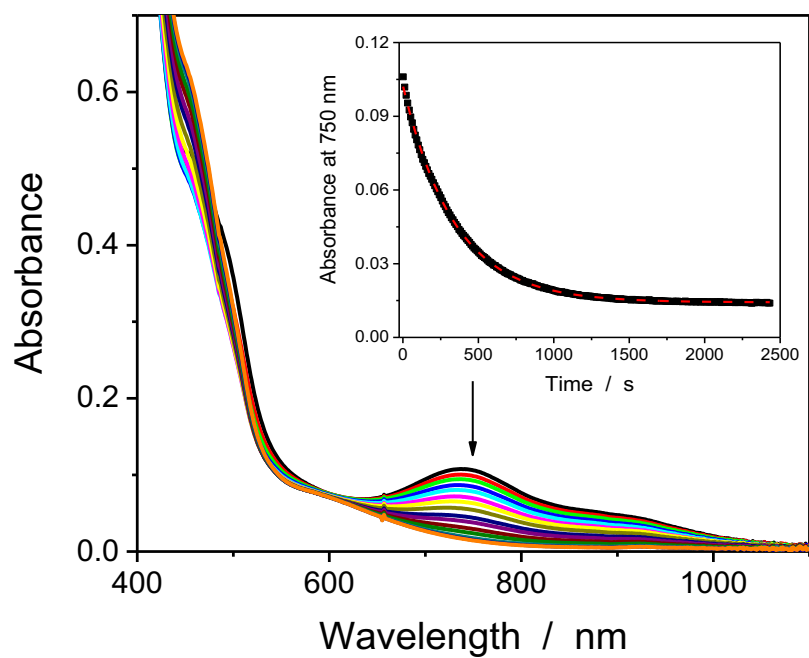
Figure 19. Representative time-resolved spectral changes during oxidation of 150 mM cyclohexane by 1 mM pre-formed Fe(IV)-oxo intermediate in CH₃CN. The inset shows absorbance at 750 nm versus time with the single-exponential fit shown in red.
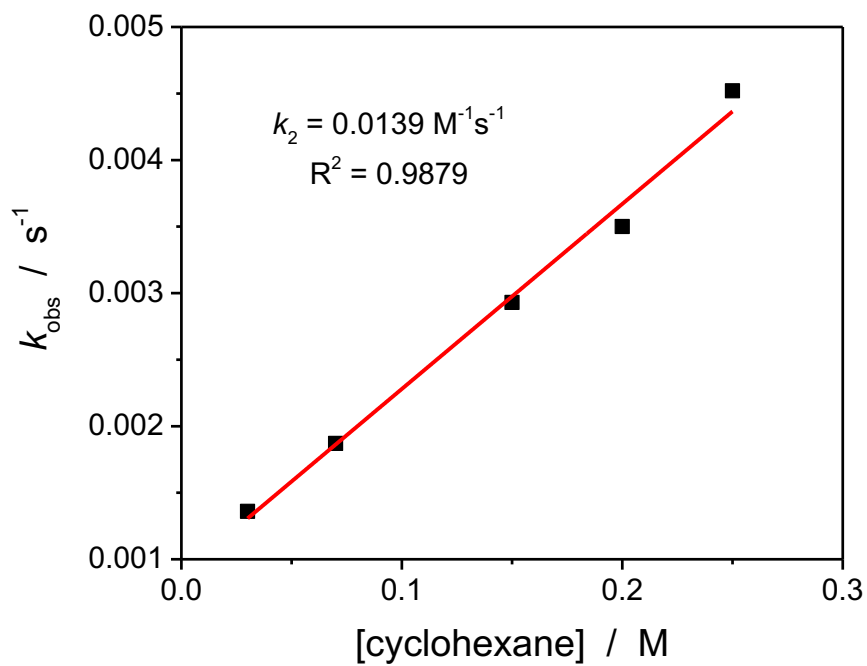
Figure 20. Plot of the pseudo-first-order rate constants, k_{obs} (s^{-1}), versus cyclohexane concentration.

The second-order rate constant, k_2 (M^{-1}s^{-1}), obtained from the slope is 1.4×10^{-2} M^{-1}s^{-1} at 23 °C.
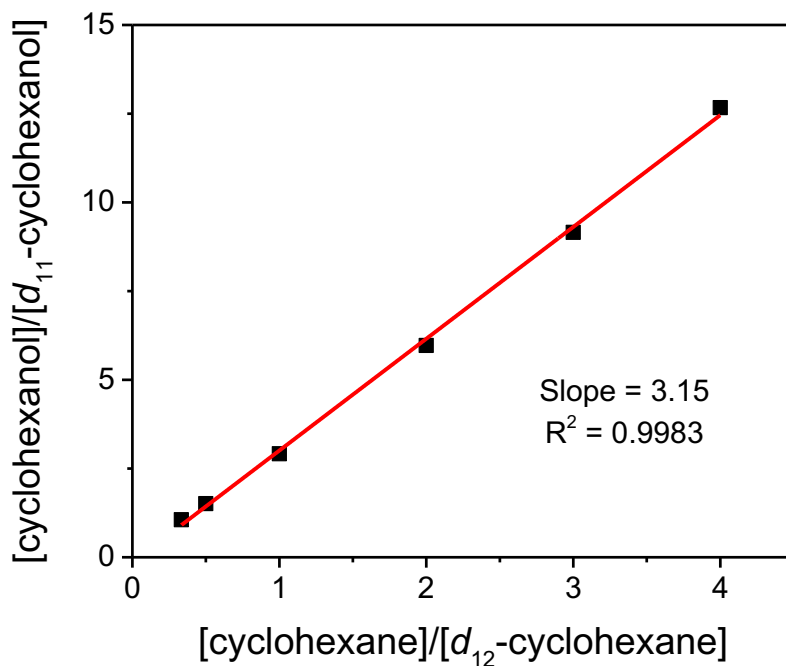
Figure 21. Plot of the integration ratios of cyclohexanol and d_{11}-cyclohexanol *versus* the ratio of cyclohexane and d_{12}-cyclohexane.

To address one of the primary aims of this work, the catalytic stability of **1-Fe** was also investigated by analyzing the amount of oxidized product relative to the amount of added mCPBA. Here, mCPBA (10 equivalents) was added every 10 minutes into a CH$_3$CN solution containing 1 mM **1-Fe** and 1000 equivalents of cyclohexane. As shown in Figure 22, the total amount of oxidized product (A + 2K) is close to the theoretical value up to 30 equivalents of mCPBA. At 100 total equivalents of mCPBA, the yield of oxidized products approaches 40%. A comparable conversion of 48% is observed with the same ratio of mCPBA to cyclohexane (Table 3, Entry 1). These results are consistent with slow deactivation of **1-Fe**. When added oxidant totals 50 equivalents, conversion to both cyclohexanol and cyclohexanone reaches a plateau indicating complete deactivation of the catalyst after 5 cycles of added mCPBA (10 equivalents/cycle). After

5 cycles, overall conversion is 70% with an alcohol-to-ketone ratio of 2.7 and a total turnover number (TON) of 35.
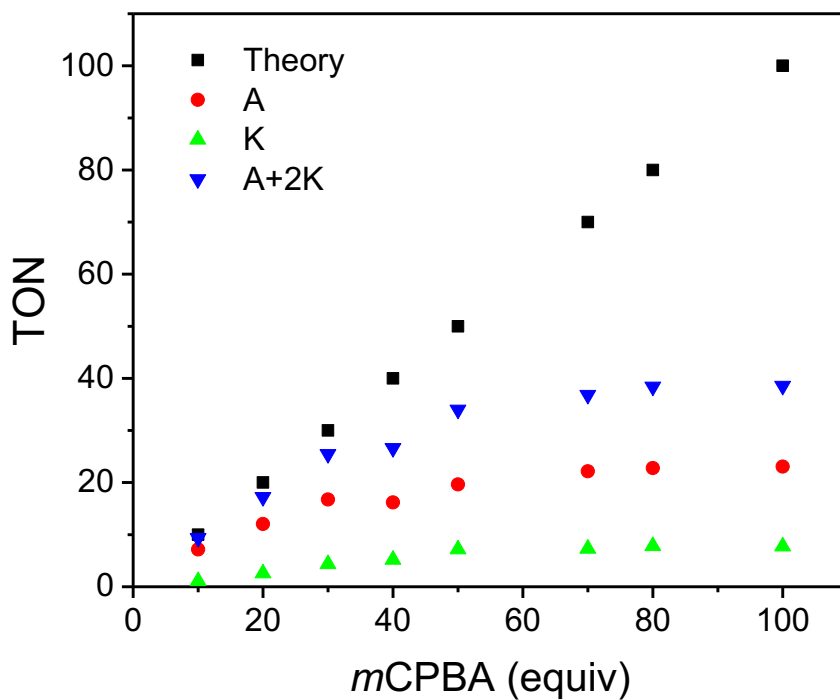
Figure 22. Plot of turnover number (TON) for each oxidized product versus equivalents of added *m*CPBA oxidant. The theoretical maximum TON is shown with black squares.

Encouraged by these results, the catalytic oxidation of adamantane (Appendix Figure 57) was investigated to assess the ability of **1-Fe** to select between its tertiary and secondary C-H bonds, which have reported bond dissociation energies of 96.2 and 100.2 kcal/mol, respectively.[53] Adding 10 equivalents of *m*CPBA into CH$_3$CN solutions containing 1 mM **1-Fe** and 10 equivalents of adamantane gives an 87% conversion yield with a regioselectivity ratio of 45 for tertiary sites (3°) to secondary sites (2°). Compared with other molecular iron-oxo catalysts, **1-Fe** exhibits high selectivity for tertiary C-H bonds in adamantane oxidation *with high conversion* (Table 4 and Figure 23). Moreover, with increasing amounts of *m*CPBA added to 500 equivalents of adamantane and 1 mM **1-Fe**, selectivity remains unchanged even as overall conversion begins to

plateau around 50% at higher oxidant-to-substrate ratios (Figure 24). Importantly, control experiments for both cyclohexane and adamantane oxidation were conducted under the same conditions but in the absence of catalyst; no conversion to products was observed after 2 hours from direct substrate oxidation by *m*CPBA.

Table 4. Comparison of selected iron catalysts for adamantane oxidation.

Catalysts[a]	Oxidant	3°/2°[b]	Yield (%)[c]	Reference
1-Fe	*m*CPBA	45	87	This work
Fe^{III}TPPCl	PhIO	48	14	20
2	*m*CPBA	110	29	21
3	H_2O_2	30	19	22
4	H_2O_2	25	31[d]	23
5	H_2O_2	28	-	24
6	H_2O_2	33	-	14a
7	*m*CPBA	17	50[d]	25

[a]Catalyst structures are shown in Figure 23. [b]3°/2° = 3 × [1-adamantanol / (2-adamantanol + 2-adamantanone)]. [c]Yield with respect to oxidant. [d]Calculated from data provided in cited work.
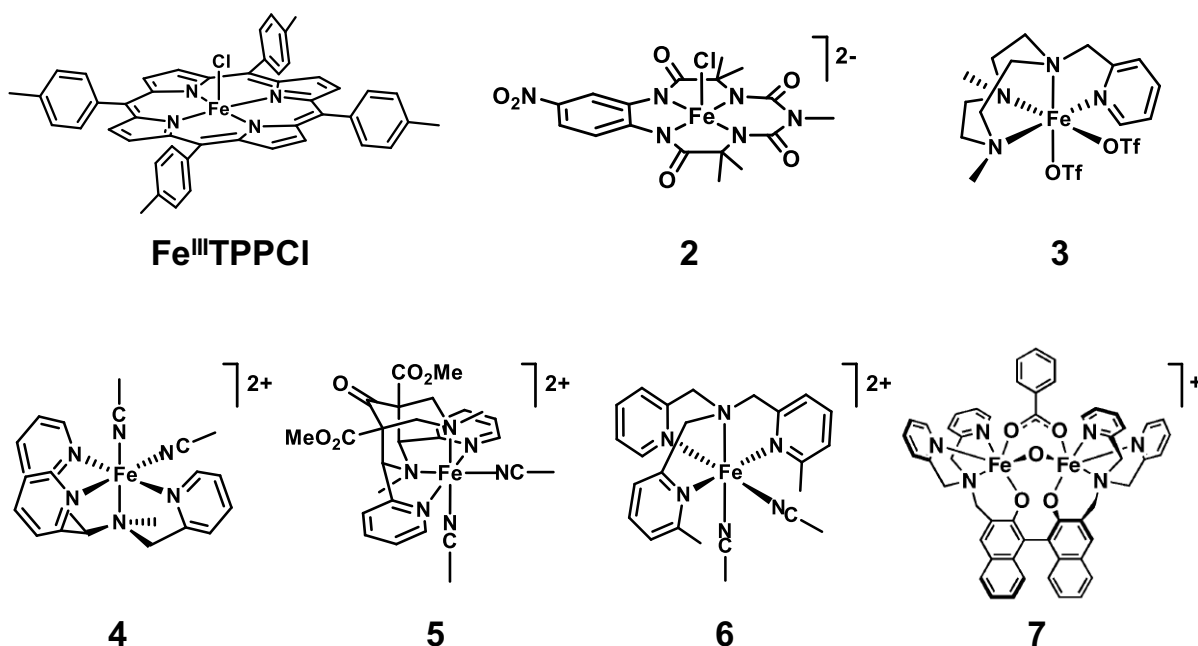
Figure 23. Line drawings of selected catalysts from the literature applied to adamantane oxidation as summarized in Table 4 of the main text.
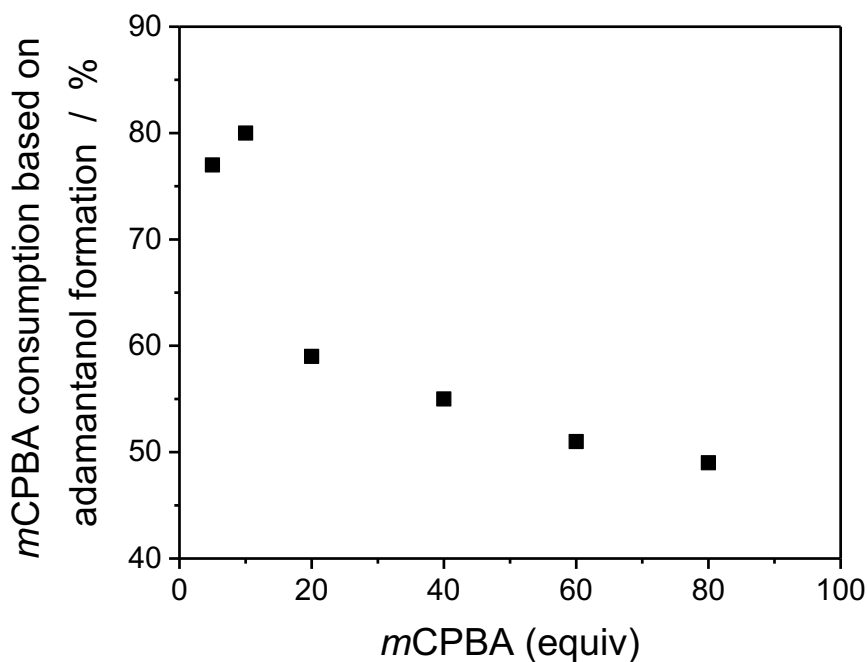
Figure 24. A plot of adamantanol generated based on productive consumption of *m*CPBA *versus* the total amount of *m*CPBA used in a series of reactions involving 1 mM **1-Fe** and 500 equivalents adamantane in CH$_3$CN with different amounts of added *m*CPBA.
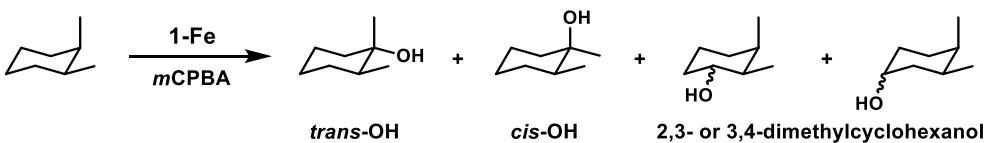
The selected iron complexes, summarized in Table 4 and shown in Figure 23, have some of the highest reported 3°/2° values for the regioselective oxidation of adamantane. Until recently, the highest selectivity for the tertiary C-H bond sites of adamantane was observed with an iron porphyrin-based catalyst (Fe^{III}TPPCl).[54] In 2017, Gupta and co-workers developed a more robust, nitro-substituted biuret-modified tetraamido macrocycle (bTAML) to obtain iron catalyst 2 with remarkable regioselectivity (3°/2° of 110), albeit with a 29% yield.[55] Notably, the unsubstituted Fe-bTAML catalyst produced a 3°/2° product ratio of 69 and a conversion yield of just ~2%, highlighting the importance of catalyst stability.[55] Indeed, **1-Fe** has comparable selectivity to Fe^{III}TPPCl, but *with 6-fold higher conversion at 87%*. In contrast to the macrocyclic examples, catalysts 3 through 6 of Table 4 and **1-Fe** possess *cis*-labile coordination sites.[50a,56-58] Relative to

these systems, **1-Fe** exhibits superior selectivity for adamantane tertiary C-H bonds and, to the best of our knowledge, affords the highest yield with respect to oxidant of all reported iron complexes for adamantane oxidation. The high regioselectivities obtained with **1-Fe** and macrocycles Fe[III]TPPCl and **2** also suggest that the relative orientation of open coordination sites is less important than other factors. Catalyst **7** is a dinuclear iron complex with two metal center active sites, which may account for its relatively high conversion yield of 50%.[59]

Next, the oxidation of *cis*-dimethylcyclohexane was examined to assess the ability of **1-Fe** to catalyze the stereospecific hydroxylation of its tertiary C-H bonds. Results summarizing the reactivity and stereoselectivity of **1-Fe** are given in Table 5. The degree to which stereoinformation is retained in the oxidation products also reports on the lifetime of alkyl radicals formed during the reaction.[60] Hydroxylation of the tertiary C-H bonds can occur with retention or inversion of configuration, which reflects the competition between C-O bond formation and epimerization of the tertiary alkyl radical intermediate. Very short radical lifetimes result in high stereospecificity where C-O bond formation is fast and the original configuration is preserved to yield *trans*-1,2-dimethylcyclohexanol (in which the methyl groups are *cis* to one another).[60a] In contrast, long-lived radicals should result in nearly equivalent amounts of *cis* and *trans* tertiary alcohol products.[60] With **1-Fe**, 100% retention of configuration (RC) is observed following the addition of 10 or 20 equivalents of *m*CPBA to 25 equivalents of *cis*-dimethylcyclohexane substrate (Appendix Figure 58). Accounting for the small amount of 2,3- and 3,4-dimethylcyclohexanol produced (2,3-OH and 3,4-OH, respectively), the regioselectivity for *trans*-OH is also as high as 77%. Only a minor loss in stereoretention is observed at lower catalyst loading (Entry 3, Appendix Figure 59), albeit with a drop in overall conversion. Addition of 0.5 equivalents of acetic acid has previously

been shown to improve conversion and selectivity for C-H bond oxidation with a nonheme iron catalyst;[7] however, there was no improvement with **1-Fe** in the presence of acetic acid.

Table 5. Regioselective oxidation of *cis*-dimethylcyclohexane.

Entry	1-Fe:substrate: *m*CPBA:AcOH	Conv. (%)[a]	RC (%)[b]	Selectivity (%)[c]
1	1:25:10	72	100	66
2	1:25:20	54	100	77
3	1:120:100	25	90	72
4	1:120:100:0.5	21	90	71

[a]Conversion efficiency with respect to *m*CPBA. [b]Retention of configuration, RC = [(*trans*-OH – *cis*-OH) / (*trans*-OH + *cis*-OH)] × 100. [c]Overall selectivity for *trans*-OH = [*trans*-OH / (*trans*-OH + *cis*-OH + 2,3-OH + 3,4-OH)] × 100.

Experimental procedures:

[Fe(BpyPY2Me)(CH₃CN)₂](OTf)₂ (1-Fe): In a round bottom flask were added Fe(OTf)$_2$ (0.11 g, 3.09 mmol) and BpyPY2Me[33f] (0.143 g, 3.09 mmol), which were subsequently dissolved in acetonitrile. After stirring overnight under nitrogen at room temperature, the reaction mixture was taken to dryness by rotary evaporation. Crystals of the resulting iron complex were grown from acetonitrile by slow diethyl ether diffusion. Yield = 0.24 g (95%). ^{1}H NMR (CD$_3$CN, 500 MHz): δ (ppm) 9.53 (d, J = 4.4 Hz, 1H), 9.22 (d, J = 4.9 Hz, 2H), 8.37 (d, J = 7.7 Hz, 1H), 8.23 (d, J = 7.7 Hz, 1H), 8.17 (td, J = 7.5, 3.0 Hz, 3H), 7.99 – 7.90 (m, 5H), 7.76 (t, J = 6.5 Hz, 1H), 7.37 (s, 2H), 2.76 (s, 3H). ^{13}C NMR (CD$_3$CN, 126 MHz): δ (ppm) 163.96, 162.40, 161.34, 160.63, 158.68, 157.49, 139.92, 139.71, 126.81, 124.45, 123.93, 123.65, 122.62, 121.93, 57.02, 20.76. HR-ESI-MS (M$^+$) m/z calc. for [**1-Fe**]$^+$, 543.0402, Found, 543.0400.

Alkane C-H Bond Oxidation by 1-Fe: In a typical reaction, to an anhydrous CH_3CN (3 mL) solution containing **1-Fe** (0.003 mmol) were added cyclohexane (3 mmol) (or adamantane (1.5 mmol)), *m*CPBA (0.03 mmol), and nitrobenzene (0.015 mmol). The reaction mixture was stirred vigorously for 2 hours at room temperature. After 2 hours, excess PPh_3 was added to 1 mL of the reaction mixture to quench the reaction before it was passed through a short silica column to remove the catalyst. An aliquot of the resulting solution was injected into a gas chromatograph (PerkinElmer Clarus 680, Column Elite-624, 30 meter, 0.25 mmID, 1.4 μm df) to analyze the products. Calibration curves were made using nitrobenzene as an internal standard to quantify products. Retention times of all peaks were compared to authentic samples.

Cyclohexane Oxidation Kinetics: The iron-oxo intermediate was generated in anhydrous acetonitrile by addition of 1 equivalent of *m*CPBA to a solution containing 1 mM **1-Fe**. Cyclohexane was then added to solutions of the pre-formed iron(IV)-oxo species resulting in substrate concentrations that ranged from 30 mM to 250 mM. The oxidation reaction was monitored over time at 23 °C by following the decay of the near-IR absorption band (λ_{max} = 739 nm) associated with the iron-oxo species (Figure 19). Kinetic traces were fit to a single-exponential function to afford pseudo-first-order rate constants (k_{obs}, s^{-1}), which were plotted versus cyclohexane concentration (Figure 20). From the slope of this plot, a second-order rate constant (k_2, $M^{-1}s^{-1}$) was determined.

Determination of kinetic isotope effect (KIE): To an anhydrous CH_3CN (3 mL) solution containing **1-Fe** (0.003 mmol) were added various ratios of cyclohexane and d_{12}-cyclohexane totaling 3 mmol, *m*CPBA (0.03 mmol), and nitrobenzene (0.015 mmol). The reaction mixture was stirred vigorously for 2 hours at room temperature. After 2 hours, excess PPh_3 was added to 1 mL of the reaction mixture to quench the reaction before it was passed through a short silica column,

eluting with CH_3CN, to remove the catalyst. An aliquot of the resulting solution was injected into a gas chromatograph to analyze the products.

Regioselectivity study with *cis*-dimethylcyclohexane: To an anhydrous CH_3CN solution containing **1-Fe** (0.006 mmol) were added 25 equivalents of *cis*-dimethylcyclohexane, 20 equivalents of *m*CPBA, and 10 equivalents of nitrobenzene. The reaction mixture was stirred vigorously for 2 hours at room temperature. After 2 hours, excess PPh_3 was added to 1 mL of the reaction mixture to quench the reaction before it was passed through a short silica column to remove the catalyst. An aliquot of the resulting solution was injected into a gas chromatograph to analyze the products.

Conclusions.

In closing, we have developed a new Fe(II) complex supported by a robust polypyridine ligand that engenders *cis*-labile coordination sites at iron. Using *m*CPBA as the terminal oxidant, we studied the catalytic activity of **1-Fe** in the functionalization of unactivated alkane C-H bonds with bond dissociation energies as high as 100 kcal/mol. Results from ESI-MS and UV-vis spectroscopy indicate that a molecular iron(IV)-oxo species is generated as the catalytically active species. The observed selectivity in cyclohexane and adamantane oxidation are consistent with a catalytic process mediated by a metal-centered oxidant rather than hydroxyl radicals. Several key observations demonstrate the high selectivity exhibited by **1-Fe**, which include high alcohol-to-ketone ratios in cyclohexane oxidation, the stereospecific hydroxylation of *cis*-1,2-dimethylcyclohexane, and the strong preference for tertiary C-H bonds in adamantane. The 3°/2° selectivity ratio of 45 for adamantane oxidation is among the highest reported for molecular iron-oxo catalysts. Moreover, high conversion yields with respect to oxidant attest to the improved stability of this iron catalyst in hydrocarbon oxygenation.

CHAPTER 3: High-Spin Enforcement in First-Row Metal Complexes of a Constrained Polyaromatic Ligand: Synthesis, Structure, and Properties

This project is a collaborate project between Dr. Jurss and Dr. F. R. Fronczek, where B. O. Wilkins from Dr. Fronczek lab contributed to study the spin crossover of the iron complexes. H. A. Dulaney for his effort in purifying the intermediates, S. Farmer for her preparing of ligands.

In this context, we sought to introduce strain remotely using a rigid polydentate scaffold as an underexplored approach to SCO compounds. Our laboratory has been interested in preorganized frameworks,[61] as in the present case which involves a tetradentate ligand that maximizes the chelate effect while dictating the metal coordination geometry through limited rotation about single bonds connecting rigid donor moieties. Herein we report a straightforward and improved synthesis of polyaromatic ligand 2,2'-di([2,2'-bipyridin]-6-yl)-1,1'-biphenyl[15] and its metalation with mid-to-late first-row transition metals. Metal complexes of Mn(II), Fe(II), Co(II), Ni(II), and Zn(II) were prepared to evaluate how the structural constraints of the ligand are balanced with the geometric and electronic preferences of the metal centers. Solid-state structures and optical, magnetic, and electrochemical properties of this series are described.

The seminal publication involving ligand **5** reported a synthesis (Figure 25A) with an overall yield of just 18%.[15] We have established an improved route to this compound as shown in Figure 25B. Briefly, a ruthenium-catalyzed homocoupling of 2-phenylpyridine affords precursor **1**.[68] Next, procedures for 2,2'-bipyridine functionalization were adapted,[69] beginning with the methylation of **1** to form intermediate **2** as a light yellow precipitate that is simply collected by filtration. Oxidation of **2** with potassium ferricyanide gives **3** in high yield, followed by bromination with phosphorus oxytribromide to produce **4**. Notably, compound **4** is a versatile intermediate for future substitution of electronically disparate donor moieties for ligand tunability. A palladium-catalyzed Stille coupling with 2-(tributylstannyl)pyridine gives the desired bipyridine-derivatized product **5** in 30% overall yield. We note that methylation of **1** gives a mixture of mono- and dimethylated (**2**) products. In practice, the product mixture is carried through the next two steps and undesired compounds are removed during purification of **4**, which was found to be easiest.

Complexation of metal ions Mn(II), Fe(II), Co(II), Ni(II), and Zn(II) was performed in acetonitrile or methanol solutions by stirring **5** with the appropriate metal precursor in a 1:1 ratio at room temperature overnight. Crystals were readily obtained from concentrated acetonitrile solutions by slow diethyl ether diffusion to give pure complexes in ~90% yield. The complexes are not sensitive to air and moisture.
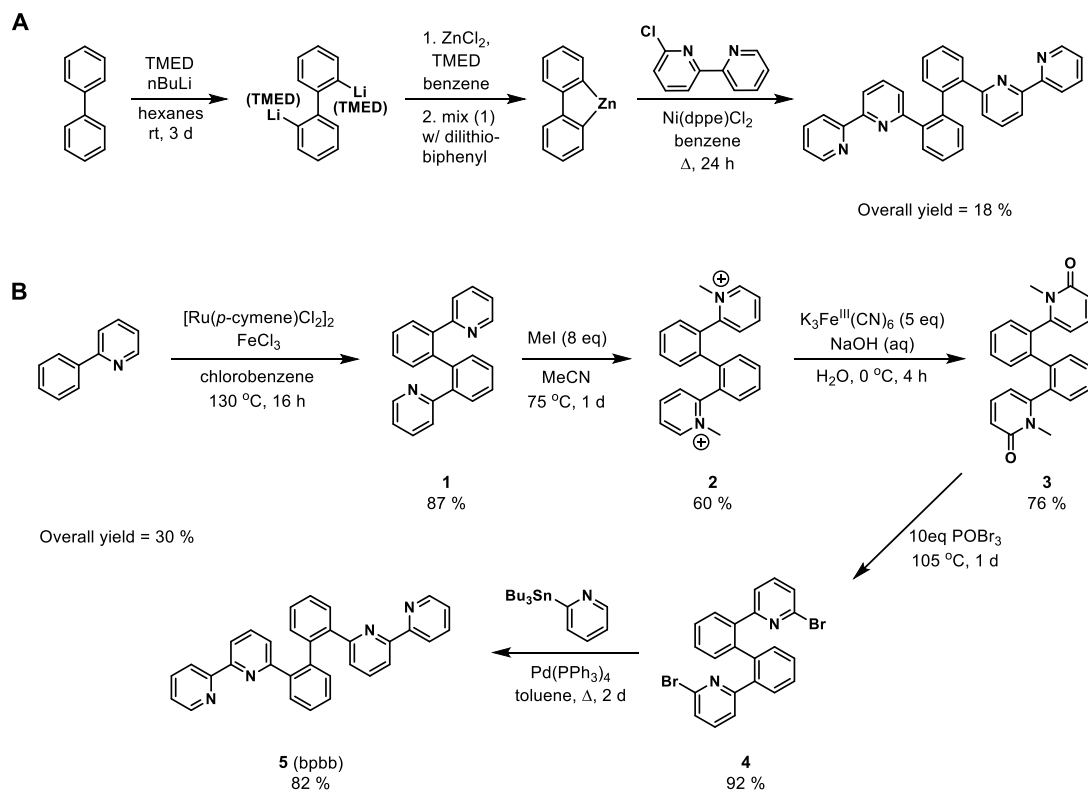
Figure 25. Synthesis of 2,2'-di([2,2'-bipyridin]-6-yl)-1,1'-biphenyl, **5**. A) Published route. B) New route to tetradentate polypyridine ligand.

Solid-state structures were obtained by X-ray crystallography as shown in Figure 26. The complexes all crystallize in the same space group (P-1) with similar unit cell parameters as presented in Table 6, along with details of data collection. The biphenyl bis(bipyridine) ligand **5** (also abbreviated bpbb) is tetradentate in each complex with its metal-nitrogen bond distances ranging from 1.981 to 2.275 Å (Table 7). From Mn(II) to Ni(II) across the series, distorted octahedral complexes are observed. The metal-ligand bond distances found in **5-Mn**, **5-Fe**, and **5-Co** are consistent with high-spin electronic states.[70] Crystal structures of Cu(I) and Cu(II) complexes with **5** were previously reported;[15] selected bond distances of the Cu(II) complex are also included in Table 7 for comparison with the M(II) complexes reported here. To clarify the

coordination configuration of each metal center, coordination polyhedra of the central transition metal atoms were also derived from the crystal structure of each complex as shown in Figure 26.

The Cu(II) and Zn(II) compounds are five-coordinate species. Using the geometric parameter τ introduced by Addison, Reedijk, and coworkers for five-coordinate structures, the degree of distortion from ideal geometries of square pyramidal and trigonal bipyramidal can be indexed.[71] A value of 1 is obtained for a perfect trigonal bipyramidal geometry while τ is zero for an ideal square pyramidal geometry.[71] Both five-coordinate compounds possess strongly distorted trigonal bipyramidal geometries as indicated by $\tau = 0.72$ for **5-Cu** and 0.60 for **5-Zn**.

Table 6. Crystallographic data for structures of first-row transition metal complexes supported by

5.

	5-Mn	5-Fe	5-Co	5-Ni	5-Zn
Formula	$C_{38}H_{30}F_6$ $MnN_5O_{6.5}S_2$	$C_{38}H_{30}F_6FeN_5$ $O_{6.5}S_2$	$C_{38}H_{30}CoF_6$ $N_5O_{6.5}S_2$	$C_{36}H_{28}Cl_2N_6$ NiO_8	$C_{34}H_{22}F_6N_4$ O_6S_2Zn
Formula Weight	893.73	894.64	897.72	802.25	826.04
Irradiation λ (Å), Temperature (K)	0.71073, 100(2)	0.71073, 100(2)	0.71073, 100(2)	0.71073, 100(2)	0.71073, 100(2)
Crystal System	Triclinic	Triclinic	Triclinic	Triclinic	Triclinic
Space Group	P-1	P-1	P-1	P-1	P-1
a (Å)	9.2068(3)	9.1892(2)	9.1905(5)	8.8345(3)	9.014(5)
b (Å)	13.8551(5)	13.9385(3)	13.9412(9)	13.4052(4)	13.854(5)
c (Å)	15.2249(5)	15.1654(3)	15.1233(9)	14.4981(5)	14.960(5)
α (°)	85.908(2)	86.1230(10)	86.292(2)	88.5640(10)	86.650(5)
β (°)	84.775(2)	84.0350(10)	83.904(3)	89.0040(10)	87.807(5)
γ (°)	81.762(2)	81.0590(10)	80.749(3)	88.179(2)	80.338(5)
V (Å^3)	1910.73(11)	1905.83(7)	1899.4(2)	1715.34(10)	1837.8(14)
Z	2	2	2	2	2
ρ_{calc} (g/cm^3)	1.553	1.559	1.570	1.553	1.493
μ (mm^{-1})	0.540	0.591	0.647	0.785	0.861
F(000)	912	914	916	824	886
Crystal Size (mm^3)	0.15 x 0.20 x 0.30	0.18 x 0.20 x 0.22	0.10 x 0.10 x 0.30	0.18 x 0.23 x 0.24	0.14 x 0.21 x 0.23
Theta range for collection (°)	1.345 to 24.406	1.35 to 25.36	1.356 to 25.458	1.52 to 25.50	1.36 to 25.38
Index ranges	$-9 \leq h \leq 10$ $-16 \leq k \leq 16$ $-17 \leq l \leq 16$	$-11 \leq h \leq 11$ $-16 \leq k \leq 16$ $-18 \leq l \leq 18$	$-11 \leq h \leq 11$ $-16 \leq k \leq 16$ $-18 \leq l \leq 18$	$-10 \leq h \leq 10$ $-16 \leq k \leq 16$ $-17 \leq l \leq 17$	$-10 \leq h \leq 10$ $-16 \leq k \leq 16$ $-17 \leq l \leq 18$
Reflctns collected	22804	49150	27618	38473	39220
Ind reflctns (R_{int})	5955 (0.0177)	6873 (0.0204)	6681 (0.0272)	6238 (0.0316)	6323 (0.0171)
Data/restr/params	5955 / 33 / 554	6873 / 2 / 550	6681 / 108 / 584	6238 / 0 / 480	6323 / 796 / 622
Final R indices [I >2σ(I)]	$R_1 = 0.0371$, $wR_2 = 0.0861$	$R_1 = 0.0270$, $wR_2 = 0.0730$	$R_1 = 0.0577$, $wR_2 = 0.1431$	$R_1 = 0.0248$, $wR_2 = 0.0682$	$R_1 = 0.0414$, $wR_2 = 0.1075$
R indices (all data)	$R_1 = 0.0417$, $wR_2 = 0.0897$	$R_1 = 0.0288$, $wR_2 = 0.0745$	$R_1 = 0.0641$, $wR_2 = 0.1464$	$R_1 = 0.0252$, $wR_2 = 0.0685$	$R_1 = 0.0445$, $wR_2 = 0.1100$
GOF	1.090	0.949	1.159	1.029	1.131
Largest diff. peak and hole (e Å^{-3})	0.728 and -0.348	0.559 and -0.352	1.012 and -0.395	0.327 and -0.440	1.169 and -0.783
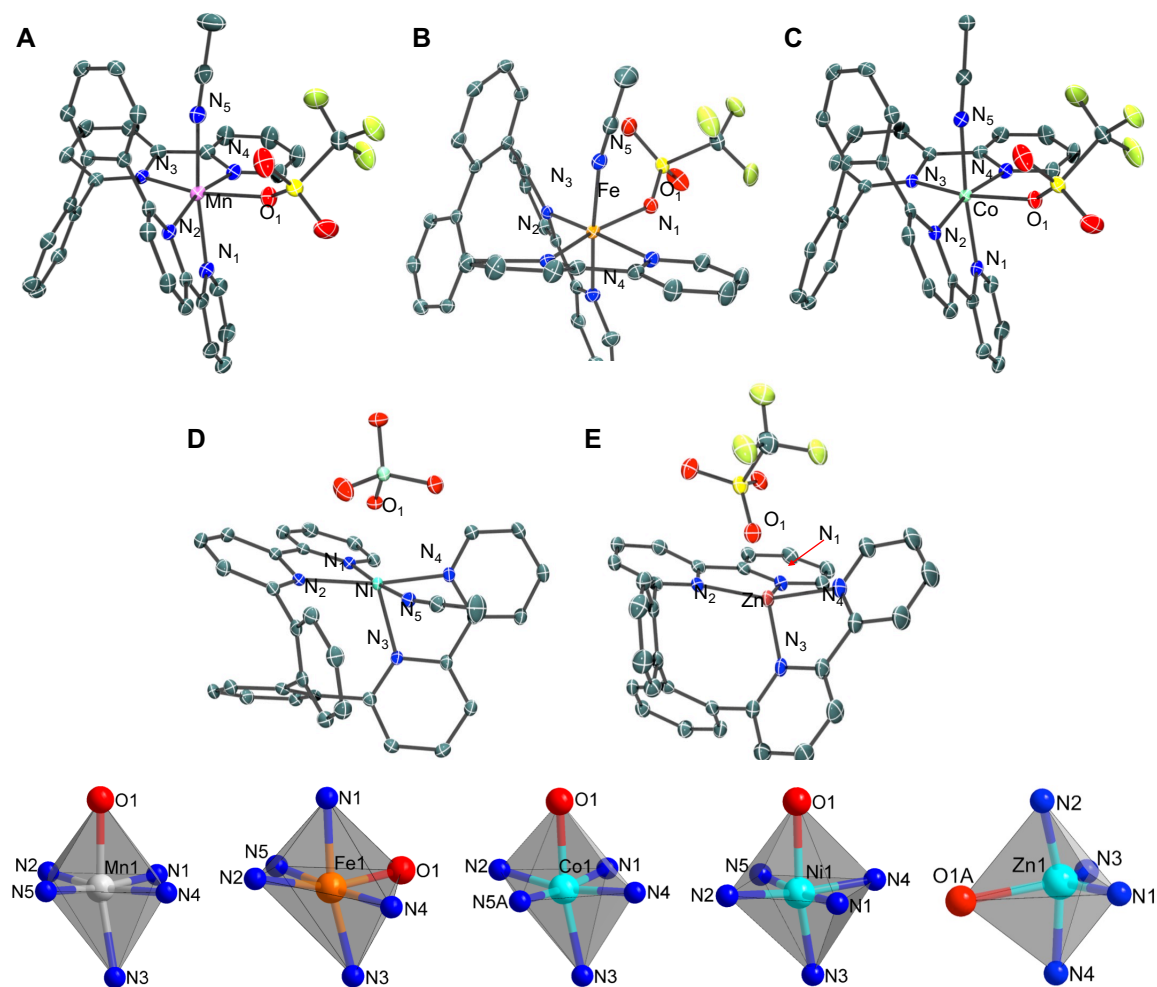
Figure 26. ORTEP diagrams of cations in **5-Mn** (A), **5-Fe** (B), **5-Co** (C), **5-Ni** (D) and **5-Zn** (E) with thermal ellipsoids rendered at the 50% probability level. Hydrogen atoms have been omitted for clarity. (Bottom) Coordination polyhedra constructed from the donor atoms that constitute the immediate coordination sphere around each transition metal ion.

Table 7. Selected bond distances of first-row metal complexes supported by **5**.

Bond Distance	Coordination Environment[a]					
	5-Mn	**5-Fe**	**5-Co**	**5-Ni**	**5-Cu′** [b]	**5-Zn**
M-N₁	2.238(2)	2.1748(13)	2.096(4)	2.0406(13)	1.981	2.060(2)
M-N₂	2.235(2)	2.2081(13)	2.157(4)	2.1366(13)	2.205	2.112(2)
M-N₃	2.275(2)	2.1967(13)	2.172(4)	2.1339(12)	2.037	2.086(2)
M-N₄	2.238(2)	2.1495(13)	2.131(4)	2.0622(13)	2.060	2.091(2)
M-N$_{avg}$	2.247	2.182	2.139	2.093	2.071	2.087
M-L	2.227(2) L = MeCN	2.1609(14) L = MeCN	2.134(8) L = MeCN	2.0585(14) L = MeCN	2.305 L = Cl	-
M-O[c]	2.2001(17)	2.1491(11)	2.181(3)	2.2208(11)	-	2.21(2)
Dihedral Angle[d]	121.4°	118.9°	117.0°	108.4°	119.4°	109.4°

a. All bond distances are reported in Angstroms (Å); *b*. From ref. 15 where **5-Cu′** is [Cu(bpbb)Cl](ClO₄)·MeCN; *c*. Bound oxygen donor of coordinated oxyanion, triflate or perchlorate; *d*. Dihedral angle of biphenyl backbone.

Ligated acetonitrile and an oxyanion complete the primary coordination sphere of the 6-coordinate Mn, Fe, Co, and Ni complexes. Analogous to observations reported of first-row metals supported by a pentadentate polypyridyl ligand,[70] M-N bond distances involving **5** decrease from left to right across the row in the octahedral complexes as expected from the periodic trend for effective ionic radii.[72] This trend is shown graphically in Figure 27. It is worth noting that the dihedral angle of the biphenyl backbone also decreases as the size of the metal ion becomes smaller in the 6-coordinate complexes. Although composed entirely of interconnected aromatic rings, the global flexibility in torsion angles enables **5** to accommodate metals of different size.
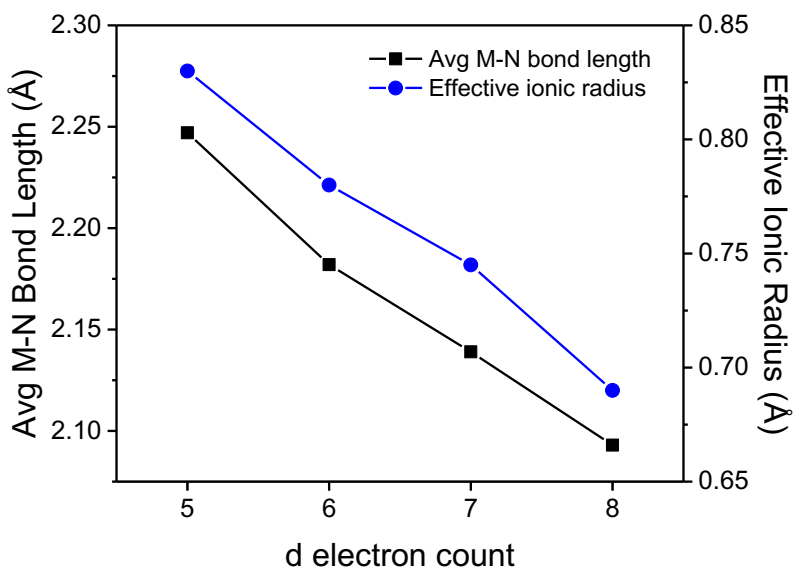
Figure 27. Plot of average metal-nitrogen bond length (Å) involving **5** and the effective ionic radius (Å) as a function of d electron count for the six-coordinate metals (**5-Mn**, **5-Fe**, **5-Co**, and **5-Ni**).

A comparison of bond distances of the pyridine donors adjacent to the biphenyl (M-N_2, M-N_3) versus the distal pyridine donors of each bipyridine unit (M-N_1, M-N_4) reveals that, in general, the former have longer bond distances than the latter, indicating that the interior donors are more constrained by the demands of the ligand and bind less strongly to the metal center. The impact of the biphenyl bridge on the bipyridine (bpy) coordination chemistry of these complexes was assessed further by comparison to relevant metal bis(bipyridine) complexes from the literature. Tables 8-13 are grouped by each metal from Mn(II) to Zn(II) and contain the metal-ligand bond distances of selected compounds, their associated references, and CCDC deposition numbers.

As typically found for d^5 manganese compounds, **5-Mn** and the Mn(II) complexes listed in Table 8 have bond distances that are consistent with high-spin electronic states. Interestingly, the average Mn-N (bpy) bond distance observed in **5-Mn** is shorter (by ~0.01 to 0.02 Å) than that

of the related Mn(II) ions comprised of two unsubstituted 2,2'-bipyridine ligands and carrying an overall charge of +1.[73-77] This result is in contrast to the remaining complexes supported by ligand **5** which tend to have longer M-N (bpy) bond distances relative to the unsubstituted 2,2'-bipyridine donors. Given the collective preference for the high-spin electron configuration, the relatively shorter M-N (bpy) bond distances observed in **5-Mn** suggests that **5** is suitably matched to Mn(II), which has the largest effective ionic radius of the M(II) ions investigated here, allowing stronger metal-ligand bonding interactions.

Table 8. Selected Bond Distances of **5-Mn** and Related Manganese(II) Compounds Containing Two Unsubstituted 2,2'-Bipyridine (bpy) Ligands.

Mn(bpy)$_2$ Complexes	Mn-N^{a,b}	Mn-N^{a,c}	Mn-O	Mn-L	Avg Mn-N (bpy)	Ref.	CCDC Deposition #
[Mn(bpbb)(OTf)(MeCN)](OTf)	2.238 **2.275**	**2.235** 2.238	2.200	2.227	2.247	*This work*	1837621
[Mn(bpy)$_2$(OH$_2$)(tipba)](ClO$_4$)^d	2.252 2.290	2.265 2.242	2.186	2.126	2.262	26	765619
[Mn(bpy)$_2$(OH$_2$)(sac)](sac)^e	2.253 2.249	2.273 2.259	2.127	2.229	2.259	27	131045
[Mn(bpy)$_2$(OH$_2$)(N$_3$)](ClO$_4$)	2.269 2.269	2.254 2.254	2.178	2.129	2.262	28	623967
[Mn(bpy)$_2$(OH$_2$)(ONO$_2$)](NO$_3$)	2.334 2.266	2.283 2.257	2.156	2.251	2.285	29	254464
[Mn(bpy)$_2$(OH$_2$)Cl](ClO$_4$)	2.235 2.292	2.260 2.268	2.167	2.447	2.264	30	1294032

a. Mn-N bond distances that are side-by-side in adjacent columns indicate that these nitrogen donors are from the same bipyridine (or bipyridine unit in the case of bpbb). *b*. Bipyridine-based nitrogen donor *trans* to a monodentate ligand. *c*. Bipyridine-based nitrogen donor *trans* to another bipyridine-based nitrogen donor. *d*. tipba = 2,4,6-triisopropylbenzoate. *e*. sac = 1,2-benzisothiazol-3(2*H*)-onate 1,1-dioxide. Bold bond distances correspond to the pyridine donors that are closest to the biphenyl backbone.

Only a limited comparison of **5-Fe** was possible with iron(II) bis(bipyridine) complexes.[78,79] Indeed, [Fe(bpy)$_2$L$_2$]$^{n+}$ complexes (where L is a labile monodentate ligand) are

very rare due to formation of the thermodynamically favored d^6 spin-paired $[Fe(bpy)_3]^{2+}$ complex.[78,79] However, crystal structures with mononuclear $Fe(bpy)_2$ cores were found with anionic donors Cl^-, CN^-, and NCS^- completing the octahedral coordination spheres (Table 9).[80-82] Despite the overall +1 positive charge of **5-Fe**, its average Fe-N (bpy) bond distance is longer than that of the neutral compounds $Fe(bpy)_2Cl_2$,[80] $Fe(bpy)_2(CN)_2$,[81] and $Fe(bpy)_2(NCS)_2$.[82] The longer bond lengths observed with **5-Fe** are consistent with a high-spin electronic state and highlight the weaker ligand field afforded by the rigid biphenyl-based ligand **5**. In addition, a strong temperature dependence was reported for $Fe(bpy)_2(NCS)_2$ in solid-state structures determined at 110 and 298 K, which have average Fe-N (bpy) bond lengths of 1.967 and 2.174 Å, respectively, indicating a change from low-spin (110 K) to high-spin (298 K).[82] This behavior is not observed with **5-Fe**, which has an average Fe-N (bpy) bond length of 2.183 Å in the solid-state at 100 K.

Table 9. Selected Bond Distances of **5-Fe** and Related Iron(II) Compounds Containing Two Unsubstituted 2,2'-Bipyridine (bpy) Ligands.

Fe(bpy)$_2$ Complexes	Fe-N^{a,b}	Fe-N^{a,c}	Fe-L	Fe-L	Avg Fe-N (bpy)	Ref.	CCDC Deposition #
[Fe(bpbb)(OTf)(MeCN)](OTf)^d	2.150 **2.208**	**2.197** 2.175	2.149	2.161	2.183	*This work*	1837622
Fe(bpy)$_2$Cl$_2$ (220 K)	2.180 2.180	2.159 2.159	2.409	2.409	2.170	80	248214
Fe(bpy)$_2$(CN)$_2$ (123 K)	1.992 2.000	1.957 1.959	1.912	1.901	1.977	81	1015599
Fe(bpy)$_2$(NCS)$_2$ (110 K)	1.964 1.964	1.969 1.969	1.945	1.945	1.967	82	1153555
Fe(bpy)$_2$(NCS)$_2$ (298 K)	2.181 2.181	2.166 2.166	2.053	2.053	2.174	82	1153557

a. Fe-N bond distances that are side-by-side in adjacent columns indicate that these nitrogen donors are from the same bipyridine (or bipyridine unit in the case of bpbb). *b*. Bipyridine-based nitrogen donor *trans* to a monodentate ligand. *c*. Bipyridine-based nitrogen donor *trans* to another bipyridine-based nitrogen donor. *d*. Data collected at a temperature of 100 K. Bold bond distances correspond to the pyridine donors that are closest to the biphenyl backbone.

Crystal structures of selected cobalt(II) complexes were also compared with **5-Co** (Table 10). Again, the average cobalt-pyridine bond distance of **5-Co** (2.139 Å) was found to be longer relative to other monocationic Co(II) ions,[83,84] reflecting the structural constraints of the tetradentate ligand. Nearly equivalent average Co-N (bpy) bond distances were observed between **5-Co** and neutral Co(bpy)$_2$Cl$_2$ (2.142 Å),[85] which are ~0.08 Å longer than that of [Co(bpy)$_2$(OH$_2$)$_2$]$^{2+}$ as expected on the basis of overall charge.[86] Similar observations were made for **5-Ni** with respect to relevant octahedral nickel(II) compounds featuring two unsubstituted 2,2'-bipyridine donors.[87-91] As summarized in Table 11, average Ni-N (bpy) bond lengths ranged from 2.059 Å for [Ni(bpy)$_2$(OH$_2$)(ONO$_2$)]$^+$ to 2.091 Å for Ni(bpy)$_2$Cl$_2$, while the average nickel-pyridine bond distance for **5-Ni** was 2.094 Å.

Table 10. Selected Bond Distances of **5-Co** and Related Cobalt(II) Compounds Containing Two Unsubstituted 2,2'-Bipyridine (bpy) Ligands.

Co(bpy)$_2$ Complexes	Co-N^{a,b}	Co-N^{a,c}	Co-L	Co-L	Avg Co-N (bpy)	Ref.	CCDC Deposition #
[Co(bpbb)(OTf)(MeCN)](OTf)	2.096 **2.171**	**2.157** 2.131	2.181	2.134	2.139	*This work*	1837623
[Co(bpy)$_2$(O$_2$NO)](NO$_3$)^d	1.939 1.939	1.924 1.924	1.898	1.898	1.932	83	1568416
Co(bpy)$_2$(OH$_2$)(O$_2$C-R-CO$_2$)^e	2.104 2.103	2.081 2.091	2.125	2.106	2.095	84	251573
Co(bpy)$_2$Cl$_2$	2.152 2.152	2.131 2.131	2.430	2.430	2.142	86	820066
[Co(bpy)$_2$(OH$_2$)$_2$]$^{2+}$ (complex anion)	2.058 2.065	2.064 2.059	2.047	2.093	2.062	85	654576

a. Co-N bond distances that are side-by-side in adjacent columns indicate that these nitrogen donors are from the same bipyridine (or bipyridine unit in the case of bpbb). *b*. Bipyridine-based nitrogen donor *trans* to a monodentate ligand. *c*. Bipyridine-based nitrogen donor *trans* to another bipyridine-based nitrogen donor. *d*. Nitrato ligand is bidentate (κ^2). *e*. O$_2$C-R-CO$_2$ = benzene-1,4-dioxyacetate. Bold bond distances correspond to the pyridine donors that are closest to the biphenyl backbone.

Table 11. Selected Bond Distances of **5-Ni** and Related Nickel(II) Compounds Containing Two

Unsubstituted 2,2'-Bipyridine (bpy) Ligands.

Ni(bpy)$_2$ Complexes	Ni-N^{a,b}	Ni-N^{a,c}	Ni-O	Ni-L	Avg Ni-N (bpy)	Ref.	CCDC Deposition #
[Ni(bpbb)(ClO$_4$)(MeCN)](ClO$_4$)	2.041 **2.134**	**2.137** 2.062	2.221	2.058	2.094	*This work*	1837624
[Ni(bpy)$_2$(OH$_2$)(O$_2$C-R)](R-CO$_2$)^d	2.095 2.096	2.079 2.065	2.075	2.078	2.084	87	717183
[Ni(bpy)$_2$(OH$_2$)(ONO$_2$)](NO$_3$)	2.065 2.081	2.045 2.044	2.058	2.151	2.059	88	1524290
[Ni(bpy)$_2$(OH$_2$)$_2$](CdBr$_4$)	2.081 2.078	2.079 2.061	2.113	2.103	2.075	89	116631
[Ni(bpy)$_2$(OH$_2$)$_2$](ClO$_4$)$_2$	2.075 2.061	2.066 2.062	2.084	2.094	2.066	90	133580
Ni(bpy)$_2$Cl$_2$	2.101 2.101	2.080 2.080	2.413	2.413	2.091	91	1237075

a. Ni-N bond distances that are side-by-side in adjacent columns indicate that these nitrogen donors

are from the same bipyridine (or bipyridine unit in the case of bpbb). *b.* Bipyridine-based nitrogen

donor *trans* to a monodentate ligand. *c.* Bipyridine-based nitrogen donor *trans* to another

bipyridine-based nitrogen donor. *d.* R-CO$_2$ = 1*H*-indole-2-carboxylate. Bold bond distances

correspond to the pyridine donors that are closest to the biphenyl backbone.

Next, the five-coordinate copper(II) and zinc(II) complexes were compared to related

bis(bipyridine) compounds (Table 12).[92-94] Copper compound (**5-Cu′**) bearing **5** and a chloro

ligand has an average Cu-N (bpy) bond distance of 2.071 Å.[15] Consistent with the bridled

coordination of **5** noted above, this average bond distance is longer by ~0.02 to 0.03 Å relative to

the average Cu-N (bpy) bond distances found in crystal structures of several [Cu(bpy)$_2$Cl]$^+$ salts.[92-94] In the same vein, **5-Zn**, ligated by the biphenyl-based polypyridine and a triflato donor, has an

average zinc-pyridine bond distance of 2.088 Å which is longer than that of both [Zn(bpy)$_2$Cl]$^+$

and [Zn(bpy)$_2$(OH$_2$)]$^{2+}$ (Table 13).[95,96] Together these results indicate that the biphenyl bridge

restrains bipyridine coordination to mid-to-late first-row metal centers.

Table 12. Selected Bond Distances of Previously Reported Copper Complex (**5-Cu′** in the main text) and Related Copper(II) Compounds Containing Two Unsubstituted 2,2'-Bipyridine (bpy) Ligands.

Cu(bpy)$_2$ Complexes	Cu-N^{a,b}	Cu-N^{a,c}	Cu-L	Cu-Cl	Avg Cu-N (bpy)	Ref.	CCDC Deposition #
[Cu(bpbb)Cl](ClO$_4$)	2.061 **2.204**	**2.037** 1.981	-	2.305	2.071	15	1162810
[Cu(bpy)$_2$Cl](R-SO$_3$)	2.104 2.110	1.978 1.990	-	2.280	2.046	80	749881
[Cu(bpy)$_2$Cl](ClO$_4$)	2.127 2.067	1.985 1.981	-	2.260	2.040	93	926638
[Cu(bpy)$_2$Cl](BF$_4$)	2.079 2.142	2.006 1.982	-	2.285	2.052	94	1259100

a. Cu-N bond distances that are side-by-side in adjacent columns indicate that these nitrogen donors are from the same bipyridine (or bipyridine unit in the case of bpbb). *b*. Bipyridine-based nitrogen donor *trans* to a monodentate ligand. *c.* Bipyridine-based nitrogen donor *trans* to another bipyridine-based nitrogen donor. Bold bond distances correspond to the pyridine donors that are closest to the biphenyl backbone.

Table 13. Selected Bond Distances of **5-Zn** and Related Zinc(II) Compounds Containing Two Unsubstituted 2,2'-Bipyridine (bpy) Ligands.

Zn(bpy)$_2$ Complexes	Zn-N^{a,b}	Zn-N^{a,c}	Zn-O	Zn-L	Avg Zn-N (bpy)	Ref.	CCDC Deposition #
[Zn(bpbb)(OTf)](OTf)	2.061 **2.085**	**2.112** 2.092	2.231	-	2.088	*This work*	1837625
[Zn(bpy)$_2$Cl](BF$_4$)	2.124 2.072	1.984 1.985		2.255	2.041	95	271110
[Zn(bpy)$_2$(OH$_2$)](ClO$_4$)$_2$	2.069 2.077	2.090 2.079	2.029	-	2.079	96	702343

a. Zn-N bond distances that are side-by-side in adjacent columns indicate that these nitrogen donors are from the same bipyridine (or bipyridine unit in the case of bpbb). *b*. Bipyridine-based nitrogen donor *trans* to a monodentate ligand. *c.* Bipyridine-based nitrogen donor *trans* to another

bipyridine-based nitrogen donor. Bold bond distances correspond to the pyridine donors that are closest to the biphenyl backbone.

Cyclic voltammetry was conducted in anhydrous acetonitrile with the title compounds (Figure 28). Multiple redox processes were observed in the cyclic voltammograms (CVs) over a wide potential range (> 3 V); $E_{1/2}$ values and peak potentials for the irreversible redox features are summarized in Table 14. All potentials are reported in volts versus the ferrocenium/ferrocene couple (V vs Fc$^{+/0}$). Irreversible to quasi-reversible metal-based oxidations occur at 0.67 V (**5-Mn**), 0.95 V (**5-Fe**), 0.74 V (**5-Co**), each of which is a M$^{III/II}$ process, and at 0.09 V (**5-Cu**) which we assign to a Cu$^{II/I}$ couple. Similar oxidations were not observed with **5-Ni** and **5-Zn**. As expected, **5-Zn** is electrochemically silent at potentials positive of -1.4 V. The zinc complex, featuring a redox-inactive metal center, is useful in identifying ligand-based redox events and has redox couples at -1.47, -1.58, and -2.17, followed by an irreversible reduction at -2.45 V. Consistent with previous observations,[15] **5-Cu** exhibits two ligand-based reductions at -2.07 and -2.26 V. Upon scanning positive, a sharp return oxidation is observed at -0.71 V, which is likely due to adsorption on the electrode surface given the reversible behavior previously reported with this compound in acetonitrile using Bu$_4$NClO$_4$ as the supporting electrolyte.[15] Compound **5-Ni** has three reversible redox processes at -1.03, -1.57, and -2.38 V that are tentatively assigned to Ni$^{II/I}$ and Ni$^{I/0}$ metal-based couples followed by a ligand-localized reduction, respectively. For **5-Co**, an irreversible feature at -1.03 V is assigned to a Co$^{II/I}$ reduction with two reversible couples at -1.69 and -1.96 V occurring that are likely ligand centered. Similarities in the CVs of **5-Fe** and **5-Mn** are apparent. Each complex has a two-electron reduction at -1.53 V (**5-Fe**) and -1.71 V (**5-Mn**), which are at

similar potentials to the initial overlapping one-electron reductions of **5-Zn**. On this basis, we

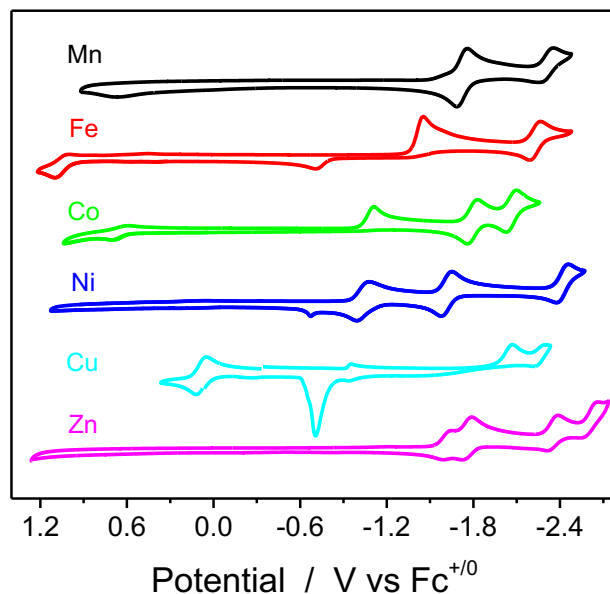assign these events as ligand-based reductions and the most negative waves to $M^{II/I}$ couples.

Figure 28. CVs of **5-Mn**, **5-Fe**, **5-Co**, **5-Ni**, **5-Cu**, and **5-Zn** (at 1 mM concentrations) in anhydrous

acetonitrile / 0.1 M Bu$_4$NPF$_6$ solutions using a glassy carbon disk electrode, $\nu = 100$ mV/s.

Table 14. Redox properties of **5-Mn**, **5-Fe**, **5-Co**, **5-Ni**, **5-Cu**, and **5-Zn** (in acetonitrile with 0.1

M Bu$_4$NPF$_6$, $\nu = 100$ mV/s).

Complex	Redox Potentials (V vs Fc$^{+/0}$)				
5-Mn	0.67[b]	-1.71	-2.30	-	-
5-Fe	0.95[b]	-1.53[c]	-2.30	-	-
5-Co	0.74	-1.03[c]	-1.69	-1.96	-
5-Ni	-	-1.03	-1.57	-2.38	-
5-Cu[a]	0.09	-0.71[b]	-2.07[c]	-2.26[c]	-
5-Zn	-	-1.47	-1.58	-2.17	-2.45[c]

a. **5-Cu** is [Cu(bpbb)](ClO$_4$)$_2$·MeCN·H$_2$O as reported in ref. 15; *b*. Irreversible ($E_{p,a}$); *c*.

Irreversible ($E_{p,c}$).

To assess the influence of the biphenyl backbone on redox potentials, the electrochemical

data summarized in Table 14 was compared to related first-row metal bis- and tris-bipyridine

complexes (Table 15).[83,97-105] Here, bipyridine-based reductions were generally found from

approximately -1.3 to -2.3 V vs $Fc^{+/0}$. Interestingly, metal-based redox couples of the complexes supported by **5** are typically more positive than those of the corresponding $[M(bpy)_3]^{2+}$ complexes, with the exception of **5-Mn**. The processes assigned to the $Fe^{III/II}$ couples of **5-Fe** and $[Fe(bpy)_3]^{2+}$ occur at 0.95 and 0.69 V, respectively,[98] whereas the $Mn^{III/II}$ couples of **5-Mn** and $[Mn(bpy)_3]^{2+}$ appear at 0.67 and 0.93 V, respectively.[97] Likewise, the $Cu^{II/I}$ couple of **5-Cu** is observed at 0.09 V, or nearly 600 mV more positive than for $[Cu(bpy)_3]^{2+}$.[104] These metal-based redox potentials are consistent with the observed metal-pyridine bond distances. Stronger Lewis acid-base bonding interactions are observed in **5-Mn** compared to related Mn(II) compounds, which results in greater electron density at the metal and a cathodic shift of the $Mn^{III/II}$ couple. However, weaker bonds to each metal center are present for the remaining compounds relative to their $[M(bpy)_3]^{2+}$ counterparts, which give rise to anodic shifts in the metal-based redox couples.

Table 15. Electrochemical data for selected *bis*(2,2'-bipyridine) and *tris*(2,2'-bipyridine) complexes of Mn, Fe, Co, Ni, Cu, and Zn.[a]

M(bpy)$_n$ Complex	Redox Potentials (V vs Fc$^{+/0}$)				Reference (Conditions)
	E_1	E_2	E_3	E_4	
5-Mn	0.67	-1.71	-2.30	-	*This work*
[Mn(bpy)$_3$]$^{2+}$	0.93	-1.74	-1.92	-2.13	97 (*b*)
5-Fe	0.95	-1.53	-2.30	-	*This work*
[Fe(bpy)$_3$]$^{2+}$	0.69	-1.72	-1.91	-2.16	98 (*c*)
[Fe(bpy)$_2$(MeCN)$_2$]$^{2+}$	1.02	-1.47	-	-	99 (*b*)
5-Co	0.74	-1.03	-1.69	-1.96	*This work*
[Co(bpy)$_3$]$^{2+}$	-0.04	-1.33	-1.95 (2e$^-$)	-	97 (*b*)
[Co(bpy)$_2$(κ^2-O$_2$NO)]$^+$	-	-1.20	-1.78	-	83 (*b*)
Co(bpy)$_2$Cl$_2$	-0.07	-1.26	-1.46	*ca.* -1.84	100 (*d*)
5-Ni	-	-1.03	-1.57	-2.38	*This work*
[Ni(bpy)$_3$]$^{2+}$	1.08	-1.93 (2e$^-$)	-	-	101, 102 (*b*)
Ni(bpy)$_2$Br$_2$	0.43	-0.08	-1.90	-2.66	103 (*e*)
5-Cu (ref. 15)	0.09	-0.71	-2.07	-2.26	*This work*
[Cu(bpy)$_3$]$^{2+}$	-0.49	-	-	-	104 (*c*)
[Cu(bpy)$_2$Br]$^+$	-0.62	-1.26	-	-	105 (*c*)
5-Zn	-	-1.47	-1.58	-2.17	*This work*
[Zn(bpy)$_3$]$^{2+}$	>1.92	-1.75 (2e$^-$)	-2.23	-	97 (*b*)

a. Reported potentials were converted to the ferrocenium/ferrocene (Fc$^{+/0}$) couple when necessary using conversions provided in the source reference or in reference 24; *b*. MeCN / 0.1 M R$_4$NClO$_4$ (where R is ethyl or *n*-butyl); *c*. MeCN / 0.1 M Bu$_4$NPF$_6$; *d*. 4:1 MeCN:H$_2$O / 0.1 M Bu$_4$NClO$_4$; *e*. DMF / 0.1 M Bu$_4$NBF$_4$.

UV-visible spectra of the compounds in acetonitrile are shown in Figure 29; associated absorption maxima and molar extinction coefficients are presented in Table 16. An intense π-to-π* transition at around 310 nm (~22000 M^{-1}cm^{-1}) is observed for all five metal complexes. Given the high-spin electronic states afforded by the constrained biphenyl bis(bipyridine) ligand, the complexes have little-to-no absorbance in the visible region. The iron complex **5-Fe** has a weak absorption band at 410 nm (660 M^{-1}cm^{-1}) that is ascribed to a metal-to-ligand charge transfer (MLCT) transition. Broad, low-intensity bands assigned to Laporte-forbidden d-d transitions are

observed at 815 nm (**5-Fe**), 482 nm (**5-Co**), and 550 and 923 nm (**5-Ni**) consistent with the solid-state structures and distorted octahedral compounds in solution. Likewise, two broad bands at 677 and 960 nm are characteristic of **5-Cu**.
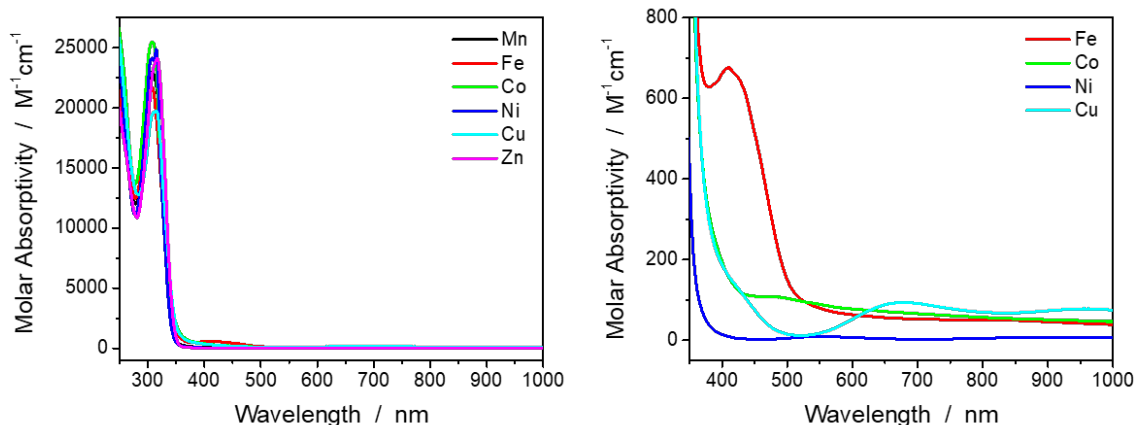

Figure 29. UV-visible spectra of Mn(II), Fe(II), Co(II), Ni(II), Cu(II), and Zn(II) complexes with ligand **5** in acetonitrile.

Table 16. UV-vis spectral properties and solution magnetic susceptibility of metal complexes bearing **5**.

5-Mn	5-Fe	5-Co	5-Ni	5-Cu	5-Zn
UV-Vis					
308 (22827)	307 (22100) 410 (660) 815 (50)	308 (25100) 482 (110)	307 (23800) 550 (10) 923 (10)	315 (19000) 677 (100) 960 (100)	317 (23500)
μ_{eff} at 298 K (μ_B)					
5.9	5.2	4.5	2.7	1.5	-

The Evans method was used to determine solution magnetic susceptibilities across the series as summarized in Table 16. The experimental magnetic moments are close to the theoretical values expected for high-spin electronic states and/or the d^n electron configuration of each M(II) ion, for example, as in d^9 Cu(II) which will have one unpaired electron regardless of geometry or spin state. The deviation in the measured value (4.5 μ_B) for **5-Co** from the anticipated theoretical

spin-only magnetic moment (3.87 μ_B) is common of cobalt complexes, including a previously reported high-spin Co(II) polypyridyl complex,[70] and indicative of an overall magnetic moment with significant orbital contribution.[106]

Intrigued by the work of Petzold and coworkers who have developed iron(II) compounds supported by hexadentate and dinucleating biphenyl-based N-donor ligands that exhibit spin crossover behavior,[18] we prepared a bis(thiocyanato) derivative **5-Fe(NCS)₂**, in addition to **5-Fe**. Their temperature-dependent magnetic behavior was investigated by solid-state SQUID magnetometry. For compounds **5-Fe** and **5-Fe(NCS)₂**, the plots of DC susceptibility vs. temperature exhibited room temperature $\chi_m T$ values of 3.98 emu·K/mol and 3.76 emu·K/mol (indicative of electron g-factors greater than 2.00), which steadily decreased to final $\chi_m T$ values of 2.70 emu·K/mol and 1.64 emu·K/mol respectively (Figure 30). Room temperature $\chi_m T$ values for high-spin Fe(II) complexes are generally in the range of 3 – 3.5,[107] but higher values have been reported as well.[108] This steady decrease in $\chi_m T$ can be attributed to zero-field splitting in the complexes and/or thermal depopulation of excited electronic states. Spin crossover behavior was not observed as the compounds maintained high-spin electron configurations over the entire temperature range, as indicated by the absence of a precipitous drop of the $\chi_m T$ values at lower temperatures.
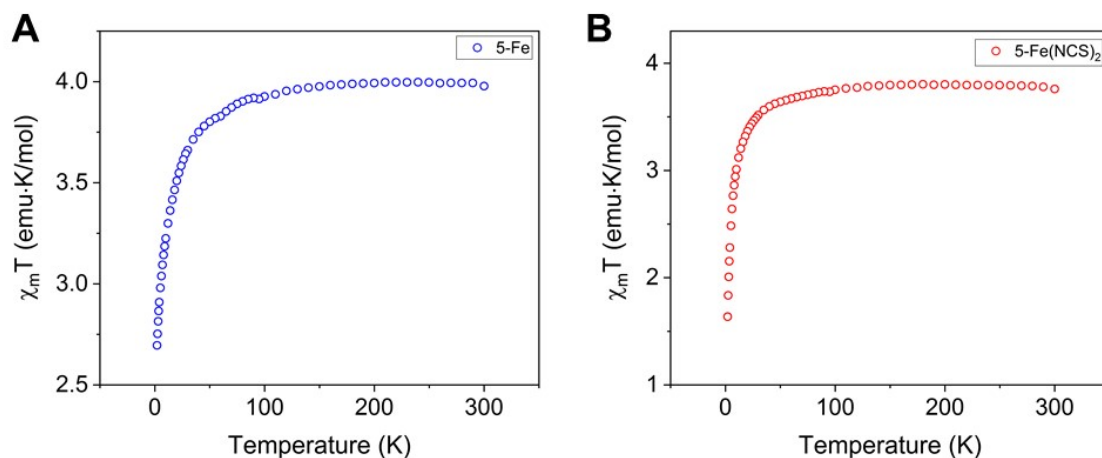
Figure 30. Temperature dependence of $\chi_M T$ for **5-Fe (A)** and **5-Fe(NCS)$_2$ (B)**.

Experimental procedures:

A literature procedure was used for the preparation of 2,2'-di(pyridin-2-yl)-1,1'-biphenyl, precursor **1**.[68] A different synthetic route to ligand **5** (bpbb) has been reported previously.[15]

2,2'-([1,1'-biphenyl]-2,2'-diyl)bis(1-methylpyridin-1-ium) iodide, **2:** To a solution of **1** (0.50 g, 1.6 mmol) in acetonitrile (10 mL), iodomethane (1.5 mL, 24.1 mmol) was added dropwise under nitrogen and the solution was refluxed for 2 days. A yellow suspension forms over the course of the reaction. The reaction mixture is allowed to cool to room temperature before diethyl ether (25 mL) is added and the precipitate is collected by vacuum filtration, washed with diethyl ether, and dried to yield a light yellow solid (1.05 g, 60%). ^{1}H NMR (MeOD, 500 MHz): δ 9.13 (d, $J =$ 6.3 Hz, 2H), 8.41 (t, $J =$ 7.9 Hz, 2H), 8.07 (t, $J =$ 1.6 Hz, 2H), 7.8 (dd, $J =$ 8.0, 7.6 Hz, 4H), 7.62 (t, $J =$ 7.6, 2H), 7.56 – 7.49 (bt, 2H), 7.12 (s, 2H). ^{13}C NMR (MeOD, 126 MHz): δ 148.878 (s), 146.75 (s), 138.81 (s), 133.60 (s), 133.03 (s), 132.56 (s), 132.17 (s), 131.84 (s), 130.86 (s), 130.35 (s), 128.82 (s), 128.37 (s). HR-ESI-MS (M$^+$) m/z calc. for [**2**]$^{2+}$, 169.0891, Found, 169.0901.

6,6'-([1,1'-biphenyl]-2,2'-diyl)bis(1-methylpyridin-2(1H)-one), **3:** This reaction is performed under air. $K_3Fe(CN)_6$ (2.48 g, 7.54 mmol) was dissolved in water (10.3 mL) and cooled to 0 °C. Next, NaOH (2.51 g, 62.8 mmol) in water (9.4 mL) and **2** (0.93 g, 1.57 mmol) in water (4.7 mL) were added dropwise to the first solution, simultaneously, *via* two dropping funnels over a period of 1.5 h. The reaction mixture was then stirred for 3 h at 0 °C before it was heated at 40 °C overnight. Saturated aqueous NaCl (28 mL) was added before dichloromethane (3 x 50 mL) was used to extract the product. The organic phase was dried over anhydrous Na_2SO_4 and taken to dryness by rotary evaporation. The resulting solid was dissolved in 8:2 ethyl acetate:methanol, filtered through neutral alumina to remove impurities and taken to dryness. Finally, the solid was dissolved in a minimum amount of dichloromethane to which hexanes was added to produce a light yellow solid that was collected by vacuum filtration to yield pure product (0.33 g, 76%). ^{1}H NMR (CDCl$_3$, 500 MHz): δ 7.51 (dt, *J* = 1.4 Hz, *J* = 7.5 Hz, 2H), 7.44 (dd, *J*=1.4 Hz, *J* = 7.5 Hz, 2H), 7.39 (dd, *J* = 1.5 Hz, *J* = 7.4 Hz, 2H), 7.20 (dd, *J* = 1.4 Hz, *J* = 7.6 Hz, 2H), 7.12 (t, *J* = 7.15 Hz, 2H), 6.48 (dd, *J* = 1.4 Hz, *J* = 9.2 Hz, 2H), 5.45 (d, *J* = 6.9 Hz, 2H), 3.0 (s, 6H). ^{13}C NMR (CDCl$_3$, 126 MHz): δ 139.59 (s), 138.44 (s), 133.70 (s), 132.26 (s), 130.48 (s), 129.88 (s), 129.62 (s), 128.45 (s), 128.31 (s), 118.90 (s), 118.79 (s), 34.59 (s). HR-ESI-MS (M$^+$) m/z calc. for [**3**+Cs$^+$], 501.0579, Found, 501.0574.

2,2'-bis(6-bromopyridin-2-yl)-1,1'-biphenyl, **4:** In an oven-dried flask, 10 equivalents of phosphorus(V) oxybromide (1.95 g, 6.8 mmol) was added to **3** (0.25 g, 0.68 mmol) and heated to 105 °C overnight with stirring under nitrogen atmosphere. The reaction was allowed to cool to room temperature and quenched with aqueous NH$_4$OH until strongly basic. The resulting precipitate was collected by filtration and washed with water. Dichloromethane was used to dissolve the solid before it was washed three times with water in a separatory funnel. The organic

phase was dried over anhydrous sodium sulfate and evaporated to dryness to afford a light yellow

solid (0.29 g, 92%). ^{1}H NMR (CDCl$_3$, 500 MHz): δ 7.53 (m, 2H), 7.49 – 7.44 (m, 2H), 7.45 – 7.39

(m, 4H), 7.27 (dd, J = 0.9 Hz, J = 7.8 Hz, 2H), 7.20 (t, J = 7.7 Hz, 2H), 6.68 (dd, J = 0.85 Hz, J =

7.6, 0.9 Hz, 2H). ^{13}C NMR (CDCl$_3$, 126 MHz): δ 158.70 (s), 141.59 (s), 139.54 (s), 138.47 (s),

137.83 (s), 131.29 (s), 130.41(s), 129.39 (s), 128.28 (s), 125.87 (s), 123.34 (s). HR-ESI-MS (M$^+$)

m/z calc. for [**4**+Cs$^+$], 596.8578, Found, 596.8571.
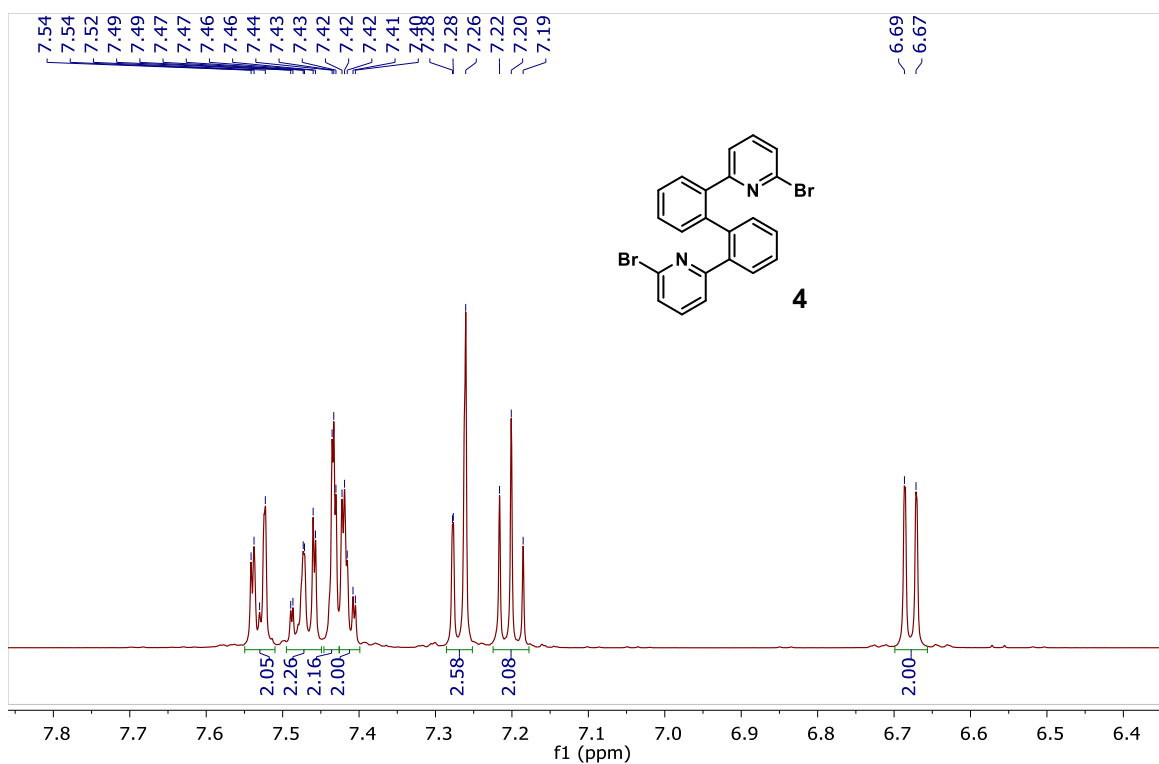
Figure 31. ^{1}H NMR spectrum (500 MHz, CDCl$_3$) of compound **4**.
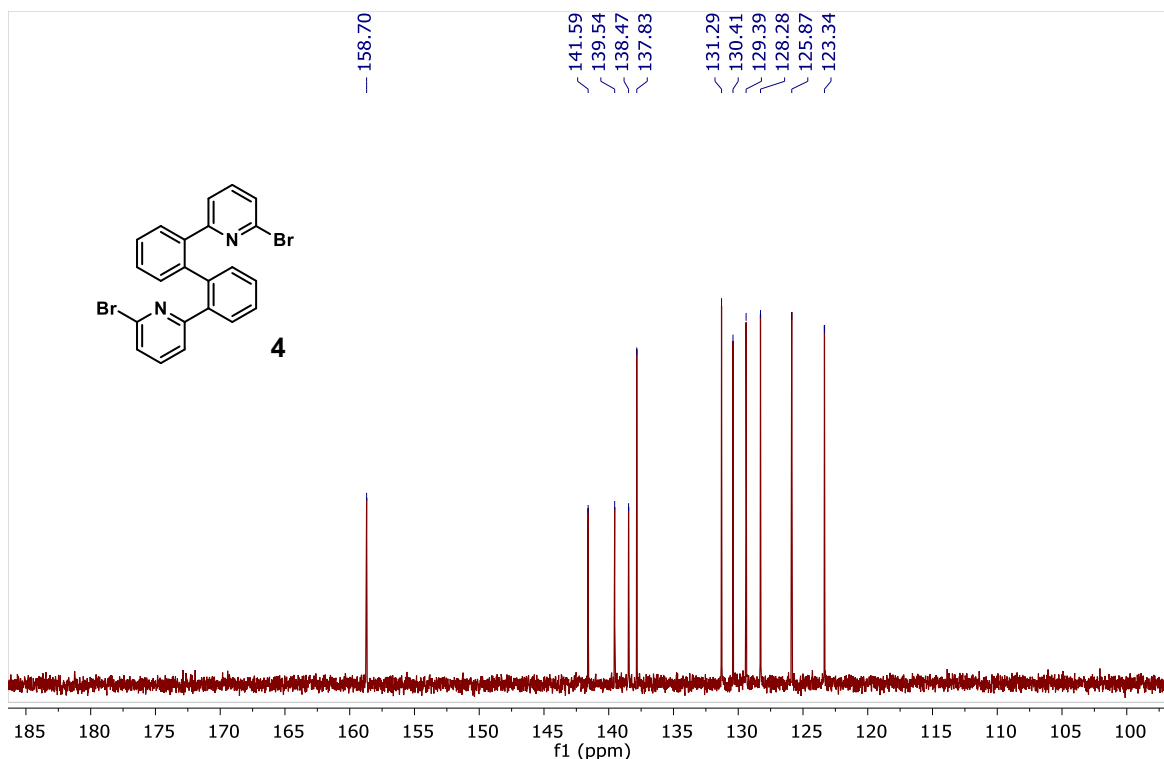
Figure 32. ^{13}C NMR spectrum (126 MHz, CDCl$_3$) of compound **4**.

***2,2'-di([2,2'-bipyridin]-6-yl)-1,1'-biphenyl,* 5** (bpbb)**:** In an oven-dried flask, **4** (0.25 g, 0.50 mmol) was dissolved in anhydrous toluene to which a solution of 2-tributylstannylpyridine (0.49 g, 1.33 mmol) in anhydrous toluene was added dropwise. Then, 0.8 mol % of Pd(PPh$_3$)$_4$ (4.9 mg, 0.004 mmol) was added and the reaction mixture was refluxed for 72 hours. After it was cooled to room temperature, the solvent was removed, and purification was achieved by silica gel column chromatography eluting with 1:1:0.1 ethyl acetate:hexanes:dichloromethane to yield a white solid (0.143 g, 82%). ^{1}H NMR (500 MHz, CDCl$_3$): δ 8.58 (d, *J* = 4.8 Hz, 1H), 8.06 (d, *J* = 7.8 Hz, 1H), 7.65 – 7.57 (m, 2H), 7.53 (d, *J* = 7.4 Hz, 2H), 7.47 (t, *J* = 7.2 Hz, 1H), 7.43 – 7.24 (m, 2H), 7.25 – 7.20 (m, 1H), 6.84 (d, *J* = 7.8 Hz, 1H). ^{13}C NMR spectra matched previously reported data.[2] HR-ESI-MS (M$^+$) m/z calc. for [**5**+H$^+$], 463.1923, Found, 463.1917.
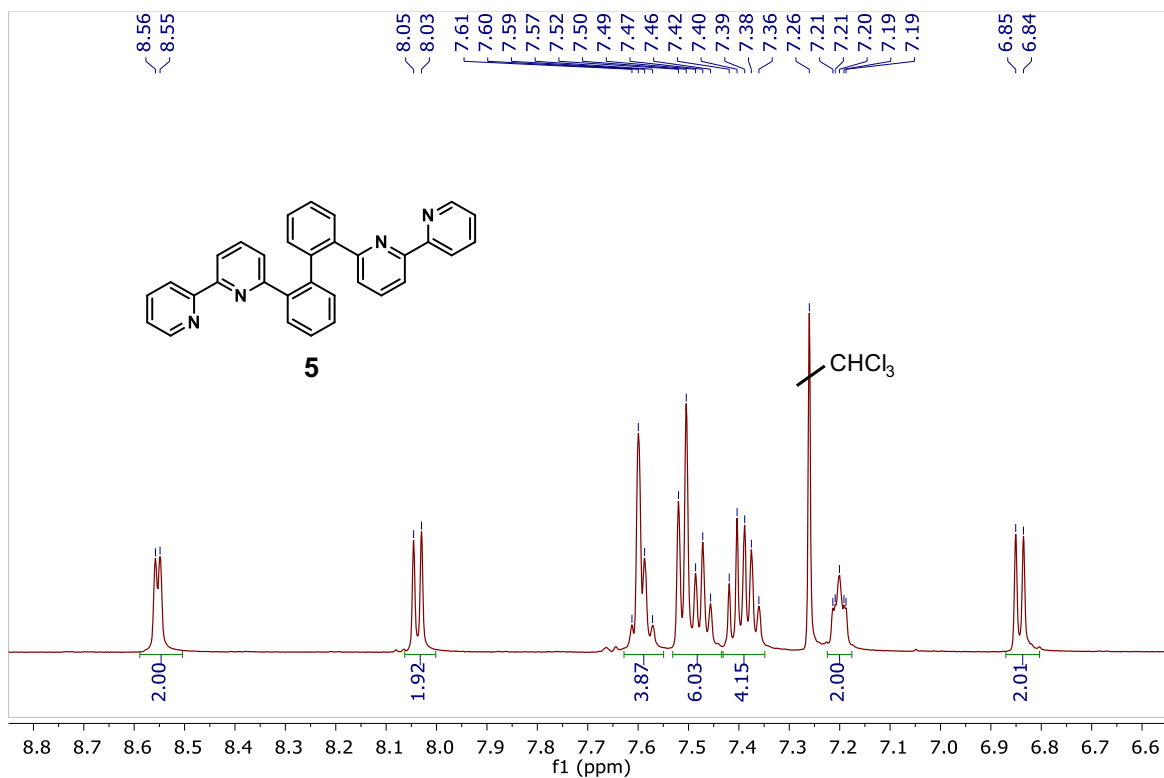
Figure 33. ^{1}H NMR spectrum (500 MHz, CDCl$_3$) of compound **5**.
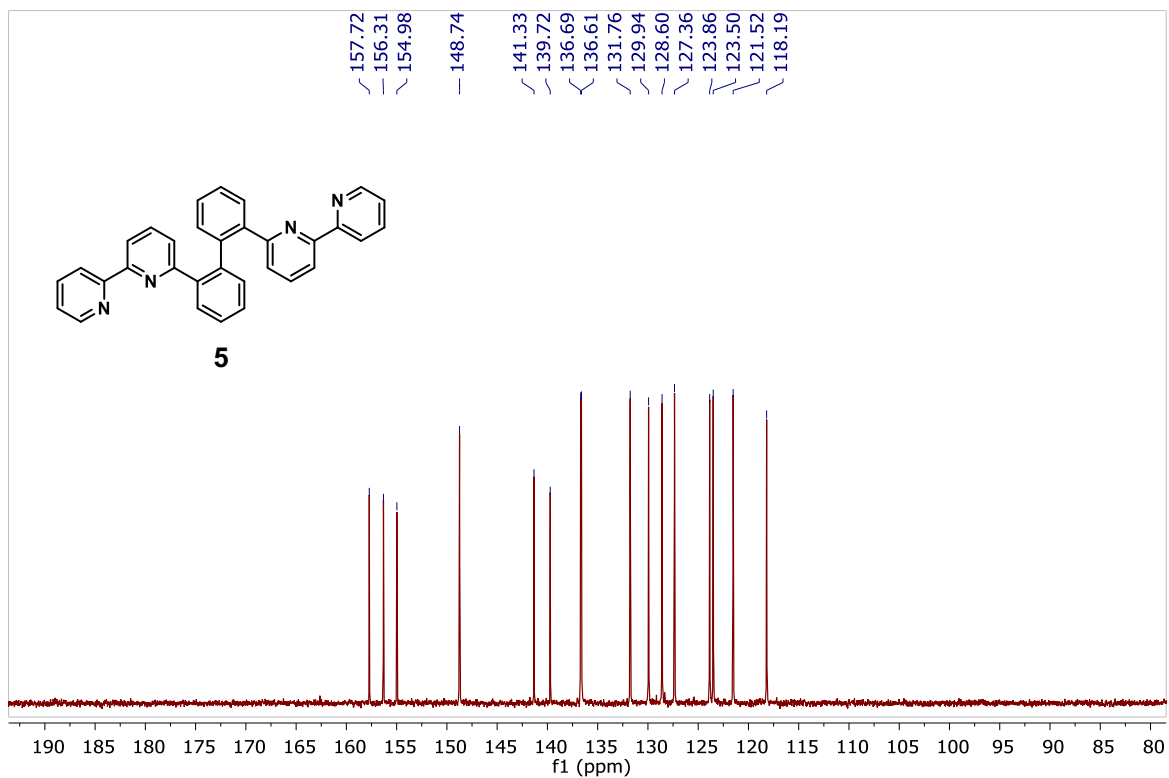
Figure 34. ^{13}C NMR spectrum (126 MHz, CDCl$_3$) of compound **5**.

5-Mn, *[Mn(bpbb)(OH₂)(OTf)](OTf)*: In a round bottom flask, $[Mn(MeCN)_2(OTf)_2]_n$ (47 mg, 0.11 mmol) and **5** (50 mg, 0.11 mmol) were added and subsequently dissolved in acetonitrile. After stirring under nitrogen at room temperature overnight, the reaction mixture was taken to dryness by rotary evaporation. The manganese complex was recrystallized from acetonitrile with slow diethyl ether diffusion. Crystals were collected, dried under vacuum, and exposed to air to give the compound as indicated. Yield = 94 mg (90%). Elem. Anal. calc. for $C_{34}H_{24}F_6MnN_4O_7S_2$: C, 48.99; H, 2.90; N, 6.72. Found: C, 49.08; H, 3.01; N, 6.67. HR-ESI-MS (M⁺) m/z calc. for $[Mn(bpbb)(OTf)]^+$, 666.0745, Found, 666.0731.

5-Fe, *[Fe(bpbb)(MeCN)(OTf)](OTf)*: In a round bottom flask, $Fe(OTf)_2$ (0.11 g, 3.1 mmol) and **5** (0.14 g, 3.1 mmol) were added and subsequently dissolved in methanol. The mixture was stirred under nitrogen at room temperature overnight. The solvent was subsequently removed by rotary evaporation, and the solid was re-dissolved in acetonitrile. Crystals were obtained by slow diffusion of diethyl ether into the concentrated solution. Yield = 93 mg (89%). Elem. Anal. calc. for $C_{36}H_{25}F_6FeN_5O_6S_2 \cdot (H_2O)_{1.5} \cdot (C_4H_{10}O)_{0.5}$: C, 49.52; H, 3.61; N, 7.60. Found: C, 49.27; H, 3.57; N, 7.20. HR-ESI-MS (M⁺) m/z calc. for $[Fe(bpbb)(OTf)]^+$, 667.0715, Found, 667.0717.

5-Co, *[Co(bpbb)(MeCN)(OTf)](OTf)*: In a round bottom flask, $Co(MeCN)_2(OTf)_2$ (48 mg, 0.11 mmol) and **5** (50 mg, 0.11 mmol) were added and subsequently dissolved in acetonitrile. After stirring under nitrogen at room temperature overnight, the pink orange reaction mixture was concentrated. Crystals of the cobalt complex were obtained by slow diethyl ether diffusion into the solution, collected, dried under vacuum. Yield = 95 mg (90%). Elem. Anal. calc. for $C_{36}H_{25}CoF_6N_5O_6S_2 \cdot (H_2O)_{1.5} \cdot (C_4H_{10}O)_{0.5}$: C, 49.36; H, 3.60; N, 7.57. Found: C, 49.14; H, 3.49; N, 7.23. HR-ESI-MS (M⁺) m/z calc. for $[Co(bpbb)(OTf)]^+$, 670.0696, Found, 670.0615.

5-Ni, *[Ni(bpbb)(MeCN)(ClO₄)](ClO₄)*: **Warning**: *Perchlorate salts are potentially explosive and should be handled in small amounts with care!* In a round bottom flask, Ni(ClO₄)₂·6H₂O (40 mg, 0.11 mmol) and **5** (50 mg, 0.11 mmol) were added and subsequently dissolved in acetonitrile (10 mL). After stirring under nitrogen at room temperature overnight, the light violet reaction mixture was taken to dryness by rotary evaporation. Crystals of the resulting nickel complex were grown from acetonitrile with slow diethyl ether diffusion. Yield = 84 mg (91%). Elem. Anal. calc. for $C_{34}H_{25}Cl_2N_5NiO_8$·$(H_2O)_{0.5}$·$(MeCN)_{0.5}$: C, 53.16; H, 3.51; N, 9.74. Found: C, 53.12; H, 3.50; N, 9.76. HR-ESI-MS (M⁺) m/z calc. for $[Ni(bpbb)(ClO_4)]^+$, 619.0683, Found, 619.0670.

5-Zn, *[Zn(bpbb)(OTf)](OTf)*: In a round bottom flask, Zn(OTf)₂ (39 mg, 0.11 mmol) and **5** (50 mg, 0.11 mmol) were added and subsequently dissolved in acetonitrile. After stirring under nitrogen at room temperature overnight, the colorless reaction mixture was taken to dryness by rotary evaporation. Crystals of the resulting zinc complex were grown from acetonitrile with slow diethyl ether diffusion. Yield = 91 mg (90%). ¹H NMR (CD₃CN, 500 MHz): δ 8.47 (m, 3H), 8.29 (dt, *J* = 1.65, 7.9 Hz, 1H), 8.22 (dd, *J* = 1.3, 5 Hz, 1H), 8.10 (dd, *J* = 2.45, 6.5 Hz, 1H), 7.65 (dt, *J* = 1.01, 5.4 Hz, 1H), 7.50 (d, *J* = 7.6 Hz, 1H), 7.31 (t, *J* = 7.5 Hz, 1H), 7.24 (dt, *J* = 0.8, 8.4 Hz, 1H), 6.91 (d, *J* = 7.65 Hz, 1H). Elem. Anal. calc. for $C_{34}H_{22}F_6N_4O_6S_2Zn$: C, 49.44; H, 2.68; N, 6.78. Found: C, 49.71; H, 2.81; N, 6.73. HR-ESI-MS (M⁺) m/z calc. for $[Zn(bpbb)]^+$, 675.0656, Found 675.0629.
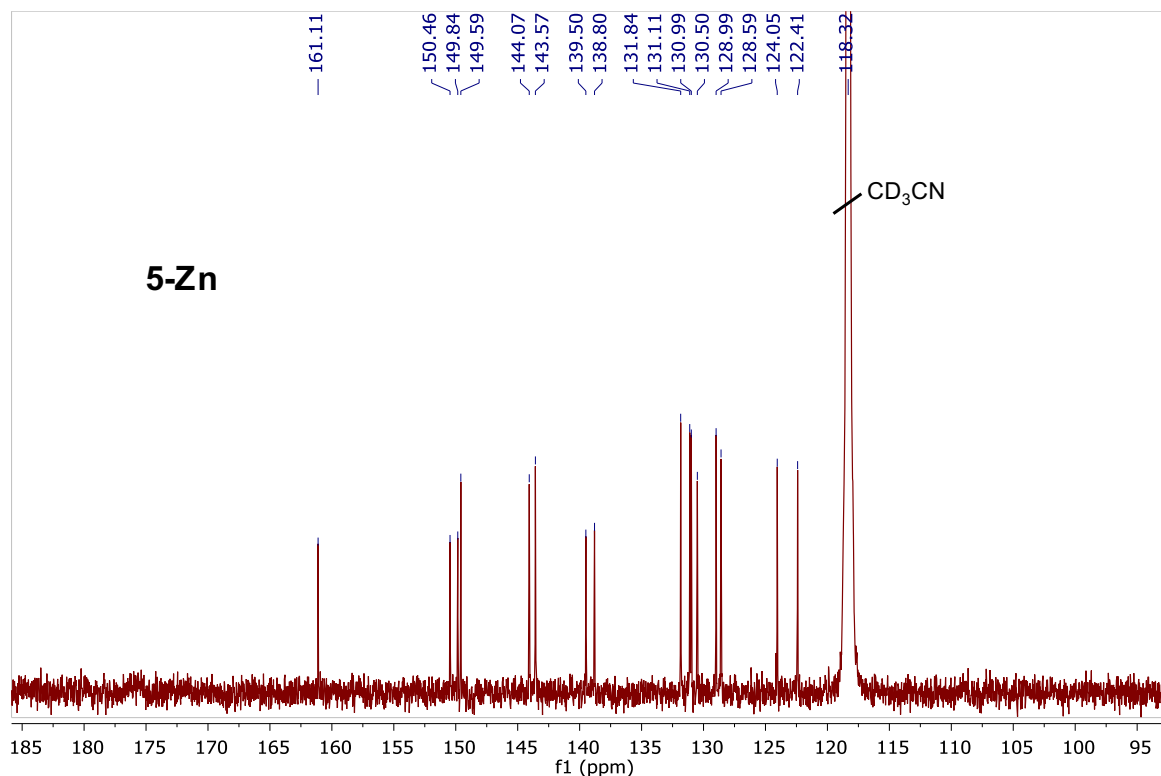
Figure 35. ^{13}C NMR spectrum (126 MHz, CD$_3$CN) of zinc complex **5-Zn**.

5-Fe(NCS)$_2$, *Fe(bpbb)(NCS)$_2$*: In a round bottom flask, FeSO$_4$·7H$_2$O (50 mg, 0.18 mmol) and NaSCN (29 mg, 0.39 mmol) were added in methanol. The mixture was stirred under nitrogen at room temperature. The mixture immediately formed a white precipitate. The mixture was filtered through Celite. Ligand **5** (83 mg, 0.18 mmol) was added to the colorless filtrate which turned purple immediately and was stirred overnight under nitrogen. The solvent was then removed by rotary evaporation. The resulting solid was dissolved in acetonitrile, and crystals were obtained by slow diffusion of diethyl ether into the concentrated solution. Yield = 108 mg (95%). Elem. Anal. calc. for C$_{34}$H$_{22}$FeN$_6$S$_2$: C, 64.36; H, 3.49; N, 13.24. Found: C, 64.62; H, 3.64; N, 13.05. HR-ESI-MS (M$^+$) m/z calc. for [Fe(bpbb)(NCS)]$^+$, 576.0946, Found, 576.0925.

Conclusions

In closing, we report an improved synthesis of a rigid polyaromatic N_4-donor ligand and have greatly expanded its known coordination chemistry. Structural, electrochemical, spectroscopic, and magnetic properties of a series of mid-to-late first-row transition metal complexes supported by the tetradentate polypyridine scaffold have been investigated. From X-ray crystallography, the ligand field around each metal ion is noticeably constrained by the limited flexibility (confined to rotation about the single bonds connecting each aromatic unit) afforded by the biphenyl backbone. High spin electronic states, based in part on the metal-ligand bond lengths, and distorted octahedral geometries are observed for the Mn(II), Fe(II), and Co(II) complexes. Distorted trigonal bipyramidal geometries are found in solid-state structures of the Cu(II) and Zn(II) derivatives. Indeed, the optical spectra, solution magnetic susceptibility measurements, and temperature-dependent SQUID magnetometry data are consistent in both the solid-state and solution analyses, confirming the structural integrity of the dissolved complexes remains intact.

Notably, **5-Fe** represents a rare example of an iron bis(bipyridine) complex possessing two labile monodentate ligands. Synthetic routes to $[Fe(bpy)_2L_2]^{n+}$ complexes are elusive due to the favored formation of the tris(bpy) complex, which is a consequence of a change from high spin to low spin between $[Fe(bpy)_2L_2]^{n+}$ to the more stable spin-paired $[Fe(bpy)_3]^{2+}$ ion.[31,32] We hypothesize that the biphenyl-linked bis(bipyridine) ligand may prevent this spin change and negate the thermodynamic driving force that would otherwise favor the tris(bpy) derivative. Spin crossover behavior was not observed in the iron(II) compounds **5-Fe** and **5-Fe(NCS)₂**. These results indicate that **5** weakens the ligand field strength around iron and, due to its limited flexibility, may be less accommodating to the changes in metal-ligand bond distances that accompany a spin transition from high-to-low. Moreover, few experiements have been conducted

to verify the reactivity of the rigid 5-Fe complex, unfortunately the extreme rigid complex haven't result a hight reactive behavior towards C-H oxidation, water oxidation or CO2 reduction. Therefore, design of the complex should not be only concern about the rigidity of the complex, but also needs to take the reactivity in consideration.

LIST OF REFERENCES

REFERENCES

1. N. S. Lewis and D. G. Nocera, *Proc. Natl. Acad. Sci. U. S. A.*, 2006, **103**, 15729.

2. https://ourworldindata.org/grapher/global-primary-energy.

3. R. A. Feely, C. L. Sabine, K. Lee, W. Berelson, J. Kleypas, V. J. Fabry and F. J. Millero, *Science*, 2004, **305**, 362; (b) J. Houghton, *Rep. Prog. Phys.*, 2005, **68**, 1343; (c) IPCC, 2014: Climate Change 2014: Synthesis Report. Contribution of Working Groups I, II and III to the Fifth Assessment Report of the Intergovernmental Panel on Climate Change [Core Writing Team, R. K. Pachauri and L. A. Meyer (eds.)]. IPCC, Geneva, Switzerland, 151 pp.

4. H. Kim, S. Bae, D. Jeon and J. Ryu, *Green Chem.*, 2018, **20**, 3732.

5. A. J. Esswein and D. G. Nocera, *Chem. Rev.*, 2007, **107**, 4022; (b) V. Artero, M. Chavarot- Kerlidou and M. Fontecave, *Angew. Chem., Int. Ed.*, 2011, **50**, 7238; (c) P. Du and R. Eisenberg, *Energy Environ. Sci.*, 2012, **5**, 6012; (d) M. Wang, L. Chen and L. Sun, *Energy Environ. Sci.*, 2012, **5**, 6763; (e) V. S. Thoi, Y. Sun, J. R. Long and C. J. Chang, *Chem. Soc. Rev.*, 2013, **42**, 2388; (f) W. T. Eckenhoff, W. R. McNamara, P. Du and R. Eisenberg, *Biochim. Biophys. Acta*, 2013, **1827**, 958; (g) R. M. Bullock, A. M. Appel and M. L. Helm, *Chem. Commun.*, 2014, **50**, 3125; (h) N. Queyriaux, R. T. Jane, J. Massin, V. Artero and M. Chavarot-Kerlidou, *Coord. Chem. Rev.*, 2015, **304-305**, 3; (i) D. Z. Zee, T. Chantarojsiri, J. R. Long and C. J. Chang, *Acc. Chem. Res.*, 2015, **48**, 2027.

6. A. C. Lindhorst, S. Haslinger and F. E. Kühn, *Chem. Commun*. 2015, **51**, 17193.

7. K. Chen, M. Costas, J. Kim, A. K. Tipton and Jr. L. Que, *J. Am. Chem. Soc*. 2002, **124**, 3026.

8. H. Bae, M. S. Seo, Y.-M. Lee, K.-B. Cho, W.-S. Kim and W. Nam, *Angew. Chem. Int. Ed*. 2016, **55**, 8027.

9. W. Nam, Y.-M. Lee and S. Fukuzumi, *Acc. Chem. Res*. 2014, **47**, 1146.

10. W. Nam, *Acc. Chem. Res*. 2007, **40**, 522.

11. M. S. Seo, N. H. Kim, K.-B. Cho, J. E. So, S. K. Park, M. Clémancey, R. Garcia-Sierres, J.-M. Latour, S. Shaik and W. Nam, *Chem. Sci*. 2011, **2**, 1039.

12. M. S. Chen and M. C. White, *Science* 2007, **318**, 783.

13. J. England, R. Gondhia, L. Bigorra-Lopez, A. R. Petersen, A. J. P.White and G. J. P. Britovsek, *Dalton Trans*. 2009, **27**, 5319.

14. (a) T. J. Collins, *Acc. Chem. Res.,* 1994, **27**, 279-285; (b) P. Comba, *Coord. Chem. Rev.,* 1999, **182**, 343-371; (c) R. D. Hancock, *Chem. Soc. Rev.,* 2013, **42**, 1500.

15. E. Müller, C. Piguet, G. Bernardinelli and A. F. Williams, *Inorg. Chem.,* 1988, **27**, 849.

16. (a) O. P. Anderson, J. Becher, H. Frydendahl, L. F. Taylor and H. Toftlund, *J. Chem. Soc., Chem. Commun.,* 1986, 699-701; (b) S. Knapp, T. P. Keenan, X. Zhang, R. Fikar, J. A. Potenza and H. J. Schugar, *J. Am. Chem. Soc.,* 1990, **112**, 3452; (c) E. Müller, G. Bernardinelli and J. Reedijk, *Inorg. Chem.,* 1996, **35**, 1952; (d) M. R. Malachowski, M. Adams, N. Elia, A. L. Rheingold and R. S. Kelly, *J. Chem. Soc., Dalton Trans.,* 1999, 2177.

17. (a) M. Réglier, C. Jorand and B. Waegell, *J. Chem. Soc., Chem. Commun.,* 1990, 1752; (b) M. R. Malachowski, A. S. Kasto, M. E. Adams, A. L. Rheingold, L. N. Zakharov, L. D. Margerum and M. Greaney, *Polyhedron,* 2009, **28**, 393.

18. (a) H. Petzold and S. Heider, *Eur. J. Inorg. Chem.,* 2011, 1249; (b) S. Heider, H. Petzold and G. Teucher, *Eur. J. Inorg. Chem.,* 2013, 2382.

19. (a) M. Kettunen, C. Vedder, F. Schaper, M. Leskelä, I. Mutikainen and H.-H. Brintzinger, *Organometallics,* 2004, **23**, 3800; (b) C. Vedder, F. Schaper, H.-H. Brintzinger, M. Kettunen, S. Babik and G. Fink, *Eur. J. Inorg. Chem.,* 2005, 1071; (c) G. J. P. Britovsek, J. England and A. J. P. White, *Dalton Trans.,* 2006, 1399; (d) T. Chen, X.-G. Liu and M. Shi, *Tetrahedron,* 2007, **63**, 4874.

20. M. A. Halcrow, *Polyhedron,* 2007, **26**, 3523.

21. P. Gütlich, Y. Garcia and H. A. Goodwin, *Chem. Soc. Rev.,* 2000, **29**, 419.

22. S. O. Schmidt, S. Kisslinger, C. Würtele, S. Bonnet, S. Schindler and F. Tuczek, *Z. Anorg. Allg. Chem.,* 2013, **639**, 2774.

23. P. Gütlich, A. B. Gaspar and Y. Garcia, *Beilstein J. Org. Chem.,* 2013, **9**, 342.

24. (a) A. Bousseksou, G. Molnár, L. Salmon and W. Nicolazzi, *Chem. Soc. Rev.,* 2011, **40**, 3313; (b) S. Brooker, *Chem. Soc. Rev.,* 2015, **44**, 2880; (c) M. A. Halcrow, *Crystals,* 2016, **6**, 58.

25. E. C. Constable, G. Baum, E. Bill, R. Dyson, R. van Eldik, D. Fenske, S. Kaderli, D. Morris, A. Neubrand, M. Neuburger, D. R. Smith, K. Wieghardt, M. Zehnder and A. D. Zuberbühler, *Chem. Eur. J.,* 1999, **5**, 498.

26. E. D. McKenzie, *Coord. Chem. Rev.,* 1971, **6**, 187.

27. D. Onggo and H. A. Goodwin, *Aust. J. Chem.,* 1991, **44**, 1539.

28. (a) C. V. Krishnan and N. Sutin, *J. Am. Chem. Soc.*, 1981, **103**, 2141; (b) W. M. Singh, T. Baine, S. Kudo, S. Tian, X. A. N. Ma, H. Zhou, N. J. DeYonker, T. C. Pham, J. C. Bollinger, D. L. Baker, B. Yan, C. E. Webster and X. Zhao, *Angew. Chem., Int. Ed.*, 2012, **51**, 5941; (c) M. Guttentag, A. Rodenberg, C. Bachmann, A. Senn, P. Hamm and R. Alberto, *Dalton Trans.*, 2013, **42**, 334; (d) M. Nippe, R. S. Khnayzer, J. A. Panetier, D. Z. Zee, B. S. Olaiya, M. Head-Gordon, C. J. Chang, F. N. Castellano and J. R. Long, *Chem. Sci.*, 2013, **4**, 3934; (e) P. Zhang, M. Wang, F. Gloaguen, L. Chen, F. Quentel and L. Sun, *Chem. Commun.*, 2013, **49**, 9455; (f) W. M. Singh, M. Mirmohades, R. T. Jane, T. A. White, L. Hammarstrom, A. Thapper, R. Lomoth and S. Ott, *Chem. Commun.*, 2013, **49**, 8638; (g) L. Tong, R. Zong and R. P. Thummel, *J. Am. Chem. Soc.*, 2014, **136**, 4881.

29. J. W. Jurss, R. S. Khnayzer, J. A. Panetier, K. A. El Roz, E. M. Nichols, M. Head-Gordon, J. R. Long, F. N. Castellano and C. J. Chang, *Chem. Sci.*, 2015, **6**, 4954.

30. A. J. Canty, N. J. Minchin, B. W. Skelton and A. H. White, *J. Chem. Soc., Dalton Trans.*, 1986, 2205.

31. C. R. Goldsmith, A. P. Cole and T. D. P. Stack, *J. Am. Chem. Soc.*, 2005, **127**, 9904.

32. (a) C. R. Goldsmith, R. T. Jonas and T. D. P. Stack, *J. Am. Chem. Soc.*, 2002, **124**, 83; (b) T. Chantarojsiri, Y. Sun, J. R. Long and C. J. Chang, *Inorg. Chem.*, 2015, **54**, 5879.

33. (a) Y. Sun, J. P. Bigi, N. A. Piro, M. L. Tang, J. R. Long and C. J. Chang, *J. Am. Chem. Soc.*, 2011, **133**, 9212; (b) D. J. Wasylenko, R. D. Palmer, E. Schott and C. P. Berlinguette,

Chem. Commun., 2012, **48**, 2107; (c) Y. Sun, J. Sun, J. R. Long, P. Yang and C. J. Chang, *Chem. Sci.*, 2013, **4**, 118; (d) C. Bachmann, M. Guttentag, B. Springler and R. Alberto, *Inorg. Chem.*, 2013, **52**, 6055; (e) E. Deponti, A. Luisa, M. Natali, E. Iengo and F. Scandola, *Dalton Trans.*, 2014, **43**, 16345; (f) R. S. Khnayzer, V. S. Thoi, M. Nippe, A. E. King, J. W. Jurss, K. A. El Roz, J. R. Long, C. J. Chang and F. N. Castellano, *Energy Environ. Sci.*, 2014, **7**, 1477; (g) B. Das, A. Orthaber, S. Ott and A. Thapper, *Chem. Commun.*, 2015, **51**, 13074.

34. L. Wang, L. Duan, R. B. Ambre, Q. Daniel, H. Chen, J. Sun, B. Das, A. Thapper, J. Uhlig, P. Dinér and L. Sun, *J. Catal.*, 2016, **335**, 72.

35. (a) H. I. Karunadasa, C. J. Chang and J. R. Long, *Nature*, 2010, **464**, 1329; (b) H. I. Karunadasa, E. Montalvo, Y. Sun, M. Majda, J. R. Long and C. J. Chang, *Science*, 2012, **335**, 698.

36. S. Ohzu, T. Ishizuka, H. Kotani and T. Kojima, *Chem. Commun.*, 2014, **50**, 15018.

37. L. J. Kershaw Cook, F. Tuna and M. A. Halcrow, *Dalton Trans.*, 2013, **42**, 2254.

38. (a) I. Nenner and G. J. Schulz, *J. Chem. Phys.*, 1975, **62**, 1747; (b) J. K. Song, N. K. Lee and S. K. Kim, *J. Chem. Phys.*, 2002, **117**, 1589.

39. H. C. Brown, *et al.*, in E. A. Braude and F. C. Nachod, Determination of Organic Structures by Physical Methods, Academic Press, New York, 1955.

40. (a) M. Darabantu, L. Boully, A. Turck and N. Plé, *Tetrahedron* 2005, **61**, 2897; (b) C. Berghian, E. Condamine, N. Plé, A. Turck, I. Silaghi-Dumitrescu, C. Maiereanu and M. Darabantu, *Tetrahedron* 2006, **62**, 7339.

41. B. Klein and P. E. Spoerri, *J. Am. Chem. Soc.*, 1951, **73**, 2949.

42. (a) R. M. Kellett and T. G. Spiro, *Inorg. Chem.*, 1985, **24**, 2373; (b) J. P. Bigi, T. E. Hanna, W. H. Harman, A. Chang and C. J. Chang, *Chem. Commun.*, 2010, **46**, 958; (c) B. D. Stubbert, J. C. Peters and H. B. Gray, *J. Am. Chem. Soc.*, 2011, **133**, 18070.

43. D. J. Wasylenko, C. Ganesamoorthy, J. Borau-Garcia and C. P. Berlinguette, *Chem. Commun.*, 2011, **47**, 4249.

44. (a) A. Rodenberg, M. Orazietti, B. Probst, C. Bachmann, R. Alberto, K. K. Baldridge and P. Hamm, *Inorg. Chem.*, 2015, **54**, 646; (b) A. Lewandowska-Andralojc, T. Baine, X. Zhao, J. T. Muckerman, E. Fujita and D. E. Polyansky, *Inorg. Chem.*, 2015, **54**, 4310.

45. K. Nehru, M. S. Seo, J. Kim and W. Nam, *Inorg. Chem.* 2007, **46**, 293.

46. M. Grau, A. Kyriacou, F. C. Martinez, I. M. de Wispelaere, A. J. P. White and G. J. P. Britovsek, *Dalton Trans.* 2014, **43**, 17108.

47. (a) J. England, M. Martinho, E. R. Farquhar, J. R. Frisch, E. L. Bominaar, E. Münck and Jr. L. Que, *Angew. Chem. Int. Ed.* 2009, **48**, 3622. (b) J. P. Bigi, W. H. Harman, B. Lassalle-Kaiser, D. M. Robles, T. A. Stich, J. Yano, R. D. Britt and C. J. Chang, *J. Am. Chem. Soc.* 2012, **134**, 1536.

48. A. Draksharapu, Q. Li, H. Logtenberg, T. A. van den Berg, A. Meetsma, J. S. Killeen, B. L. Feringa, R. Hage, G. Roelfes and W. R. Browne, *Inorg. Chem.* 2012, **51**, 900.

49. J. England, G. J. P. Britovsek, N. Rabadia and A. J. P. White, *Inorg. Chem.* 2007, **46**, 3752.

50. (a) K. Chen and Jr. L. Que, *J. Am. Chem. Soc.* 2001, **123**, 6327; (b) S. Hong, Y.-M. Lee, K.-B. Cho, K. Sundaravel, J. Cho, M. J. Kim, W. Shin and W. Nam, *J. Am. Chem. Soc.* 2011, **133**, 11876.

51. (a) Jr. L. Que and W. B. Tolman, *Nature* 2008, **455**, 333; (b) K. P. Bryliakov and E. P. Talsi, *Coord. Chem. Rev.* 2014, **276**, 73.

52. A. R. McDonald and Jr. L. Que, *Coord. Chem. Rev.* 2013, **257**, 414.

53. Y. Hitomi, K. Arakawa, T. Funabiki and M. Kodera, *Angew. Chem. Int. Ed.* 2012, **51**, 3448.

54. J. T. Groves, T. E. Nemo and R. S. Myers, *J. Am. Chem. Soc.* 1983, **105**, 6243.

55. M. Ghosh, S. Pattanayak, B. B. Dhar, K. K. Singh, C. Panda and S. S. Gupta, *Inorg. Chem.* 2017, **56**, 10852.

56. A. Company, L. Gómez, M. Güell, X. Ribas, J. M. Luis and Jr. L. Que, *J. Am. Chem. Soc.* 2007, **129**, 15766.

57. M. Klopstra, G. Roelfes, R. Hage, R. M. Kellogg and B. L. Feringa, *Eur. J. Inorg. Chem.* 2004, 846.

58. P. Comba, M. Maurer and P. Vadivelu, *Inorg. Chem.* 2009, **48**, 10389.

59. T. Nagataki, Y. Tachi and S. Itoh, *J. Mol. Catal. A: Chem.* 2005, **225**, 103.

60. M. Costas, K. Chen and Jr. L. Que, *Coord. Chem. Rev.* 2000, **200-202**, 517.

61. (a) L. Chen, A. Khadivi, M. Singh and J. W. Jurss, *Inorg. Chem. Front.,* 2017, **4**, 1649; (b) X. Su, K. M. McCardle, J. A. Panetier and J. W. Jurss, *Chem. Commun.,* 2018, **54**, 3351;

(c) W. Yang, S. Sinha Roy, W. C. Pitts, R. Nelson, F. R. Fronczek and J. W. Jurss, *Inorg. Chem.,* 2018, **57**, 9564.

62. (a) D. F. Evans, *J. Chem. Soc.,* 1959, 2003-2005; (b) G. A. Bain and J. F. Berry, *J. Chem. Ed.,* 2008, **85**, 532.

63. APEX2, v. 2009; Bruker Analytical X-Ray Systems, Inc: Madison, WI, 2009.

64. G. M. Sheldrick, SADABS, Version 2.03; Bruker Analytical X-ray Systems, Inc: Madison, WI, 2000.

65. (a) G. M. Sheldrick, *Acta Crystallogr., Sect. A: Found. Crystallogr.,* 1990, **46**, 467; (b) G. M. Sheldrick, *Acta Crystallogr., Sect. A: Found Crystallogr.,* 2008, **64**, 112; (c) G. M. Sheldrick, SHELXL-2014/7: Program for crystal structure determination, University of Göttingen: Göttingen, Germany, 2014.

66. (a) A. L. Spek, PLATON - A Multipurpose Crystallographic Tool, Utrecht University, Utrecht, The Netherlands, 2007; (b) A. L. Spek, PLATON SQUEEZE: A tool for the calculation of the disordered solvent contribution to the calculated structure factors. *Acta Crystallogr., Sect. C: Struct. Chem.,* 2015, **71**, 9.

67. H. Putz and K. Bradenburg, *Diamond - Crystal and Molecular Structure Visualization*, Crystal Impact: GbR, Kreuzherrenstr. 102, 53227 Bonn, Germany, http://www.crystalimpact.com/diamond.

68. X. Guo, G. Deng, C.-J. Li, *Adv. Synth. Catal.,* 2009, **351**, 2071.

69. M. Böttger, B. Wiegmann, S. Schaumburg, P. G. Jones, W. Kowalsky and H.-H. Johannes, *Beilstein J. Org. Chem.,* 2012, **8**, 1037.

70. R. J. M. Klein Gebbink, R. T. Jonas, C. R. Goldsmith and T. D. P. Stack, *Inorg. Chem.*, 2002, **41**, 4633.

71. A. W. Addison, T. N. Rao, J. Reedijk, J. van Rijn and G. C. Verschoor, *J. Chem. Soc., Dalton Trans.,* 1984, 1349.

72. R. D. Shannon, *Acta Crystallogr.,* 1976, **A32**, 751.

73. N. Palanisami and R. Murugavel, *Inorg. Chim. Acta*, 2011, **365**, 430.

74. K. B. Dillon, C. Bilton, J. A. K. Howard, V. J. Hoy, R. M. K. Deng and D. T. Sethatho, *Acta Crystallogr., Sect. C: Cryst. Struct. Commun.*, 1999, **C55**, 330.

75. M. Shao, Z.-X. Miao and M.-X. Li, *Acta Crystallogr., Sect. E: Struct. Rep. Online*, 2006, **E62**, m2575.

76. G. Fernández, M. Corbella, M. Alfonso, H. Stoeckli-Evans and I. Castro, *Inorg. Chem.*, 2004, **43**, 6684.

77. X.-M. Chen, K.-L. Shi, T. C. W. Mak and B.-S. Luo, *Acta Crystallogr., Sect. C: Cryst. Struct. Commun.*, 1995, **C51**, 358.

78. H. Irving and D. H. Mellor, *J. Chem. Soc.,* 1962, 5222.

79. M.-N. Collomb, A. Deronzier, K. Gorgy and J.-C. Leprêtre, *New J. Chem.,* 2000, **24**, 455.

80. S. Parsons, R. Winpenny and P. A. Wood, *CCDC 248214: Experimental Crystal Structure Determination*, 2014, DOI: 10.5517/cc8b8xr.

81. Y. Wang, X. Ma, S. Hu, Y. Wen, Z. Xue, X. Zhu, X. Zhang, T. Sheng and X. Wu, *Dalton Trans.*, 2014, **43**, 17453.

82. M. Konno and M. Mikami-Kido, *Bull. Chem. Soc. Jpn.*, 1991, **64**, 339.

83. S.-P. Luo, L.-Z. Tang and S.-Z. Zhan, *Inorg. Chem. Commun.,* 2017, **86**, 276.

84. S. Gao, J.-W. Liu, L.-H. Huo and H. Zhao, *Acta Crystallogr., Sect. E: Struct. Rep. Online,* 2004, **E60**, m1202.

85. V. Ciornea, L. Mingalieva, J.-P. Costes, G. Novitchi, I. Filippova, R. T. Galeev, S. Shova, V. K. Voronkova and A. Gulea, *Inorg. Chim. Acta*, 2008, **361**, 1947.

86. K. A. Kumar, M. Amuthaselvi and A. Dayalan, *Acta Crystallogr., Sect. E: Struct. Rep. Online*, 2011, **E67**, m468.

87. B.-S. Zhang, Z.-X. Liu, L.-H. Liu, T. Pan and S.-F. Ye, *Acta Crystallogr., Sect. E: Struct. Rep. Online*, 2009, **E65**, m48.

88. M. Garai, D. Dey, H. R. Yadav, A. R. Choudhury, N. Kole and B. Biswas, *Polyhedron*, 2017, **129**, 114.

89. D. J. Chesnut, R. C. Haushalter and J. Zubieta, *Inorg. Chim. Acta*, 1999, **292**, 41.

90. Y. Rodríguez-Martín, J. González-Platas and C. Ruiz-Pérez, *Acta Crystallogr., Sect. C*, 1999, **C55**, 1087.

91. B. Hipler, M. Döring, C. Dubs, H. Görls, T. Hübler and E. Uhlig, Z. *Anorg. Allg. Chem.,* 1998, **624**, 1329.

92. M. A. Sharif, M. Tabatabaee, V. Beik and H. R. Khavasi, *CCDC 749881: Experimental Crystal Structure Determination*, 2014, DOI: 10.5517/cct59qz.

93. A. Jayamani, N. Sengottuvelan, S. K. Kang and Y.-I. Kim, *Polyhedron*, 2015, **98**, 203.

94. P. Nagle, E. O′Sullivan, B. J. Hathaway and E. Müller, *J. Chem. Soc., Dalton Trans.*, 1990, **0**, 3399.

95. J.-C. Yao, F.-J. Yao, J.-B. Guo, W. Huang, S.-H. Gou, *CCDC 271110: Experimental Crystal Structure Determination*, 2014, DOI: 10.5517/cc933hz.

96. G. Singh, I. P. S. Kapoor, D. Kumar, U. P. Singh and N. Goel, *Inorg. Chim. Acta*, 2009, **362**, 4091.

97. S. A. Richert, P. K. S. Tsang and D. T. Sawyer, *Inorg. Chem.,* 1989, **28**, 2471.

98. J. P. F. Rebolledo-Chávez, M. Cruz-Ramírez, R. Patakfalvi, F. J. Tenorio Rangel and L. Ortiz-Frade, *Electrochimica Acta,* 2017, **247**, 241.

99. M.-N. Collomb, A. Deronzier, K. Gorgy and J.-C. Leprêtre, *New J. Chem.,* 2000, **24**, 455.

100. M. A. W. Lawrence and A. A. Holder, *Inorg. Chim. Acta,* 2016, **441**, 157.

101. R. Prasad and D. B. Scaife, *J. Electroanal. Chem.,* 1977, **84**, 373.

102. P. N. Bartlett and V. Eastwick-Field, *Electrochimica Acta,* 1993, **38**, 2515.

103. S. Fomina, Y. A. Kislitsyn, V. M. Babaev, I. K. Rizvanov, O. G. Sinyashin, J. W. Heinicke and D. G. Yakhvarov, *Russian J. Electrochem.,* 2015, **51**, 1069.

104. R. R. Ruminski, *Inorg. Chim. Acta,* 1985, **103**, 159.

105. R. J. Crutchley, R. Hynes and E. J. Gabe, *Inorg. Chem.,* 1990, **29**, 4921.

106. F. A. Cotton and G. Wilkinson, *Advanced Inorganic Chemistry*, 5th edition; Wiley-Interscience: New York, 1988.

107. S. Kisslinger, H. Kelm, S. Zheng, A. Beitat, C. Würtele, R. Wortmann, S. Bonnet, S. Herres-Pawlis, H.-J. Krüger and S. Schindler, *Z. Anorg. Allg. Chem.,* 2012, **638**, 2069.

108. Kimura and T. Ishida, *Inorganics,* 2017, **5**, 52.

APPENDIX
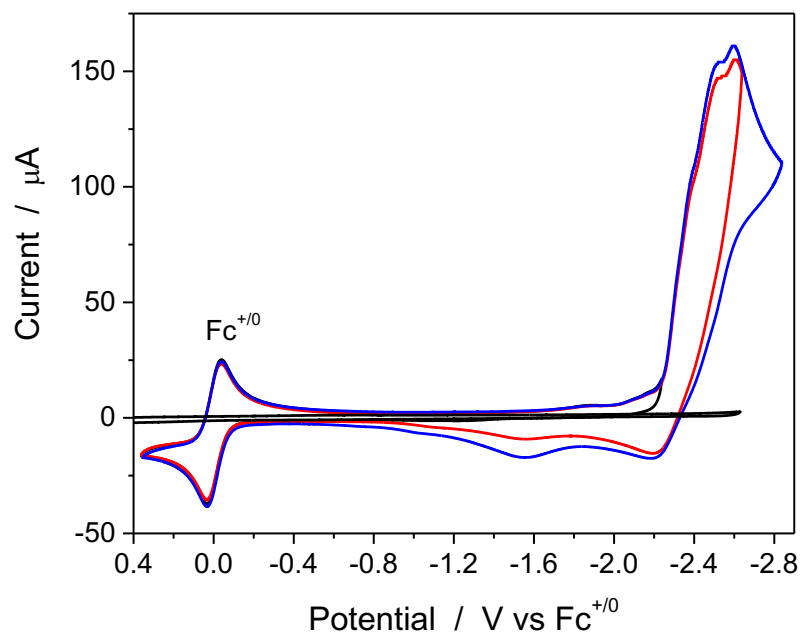
Figure 36. Cyclic voltammograms of free ligand, PZ5Me$_2$ (1 mM concentration), in 0.1 M Bu$_4$NPF$_6$ CH$_3$CN with the ferrocene peak included as the internal reference, scan rate = 100 mV/s. The background is shown in black under the same conditions.
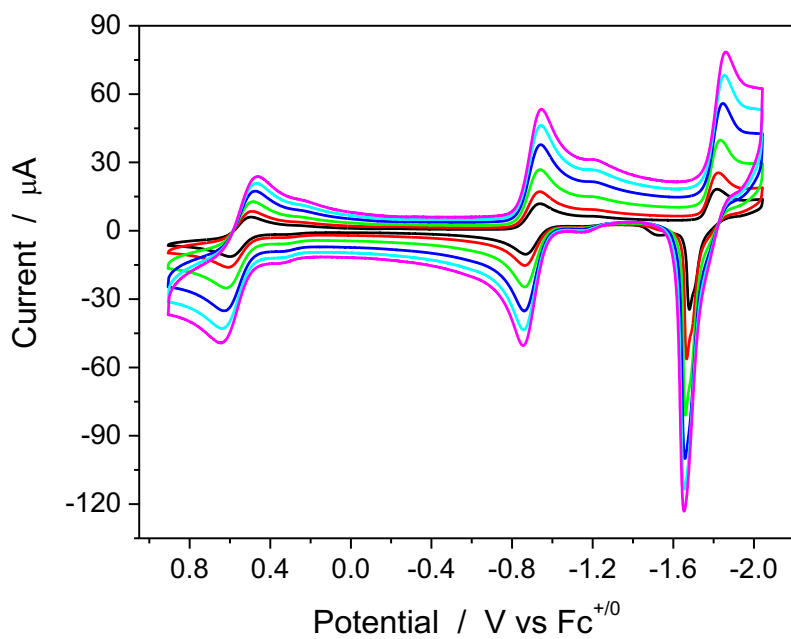
Figure 37. Cyclic voltammograms of 1 mM $[(PZ5Me_2)Co(OH_2)](OTf)_2$ in 0.1 M Bu_4NPF_6 CH_3CN referenced to ferrocene, scan rates = 50 to 1000 mV/s.

A

$R^2 = 0.9999$

B

$R^2 = 1.0000$
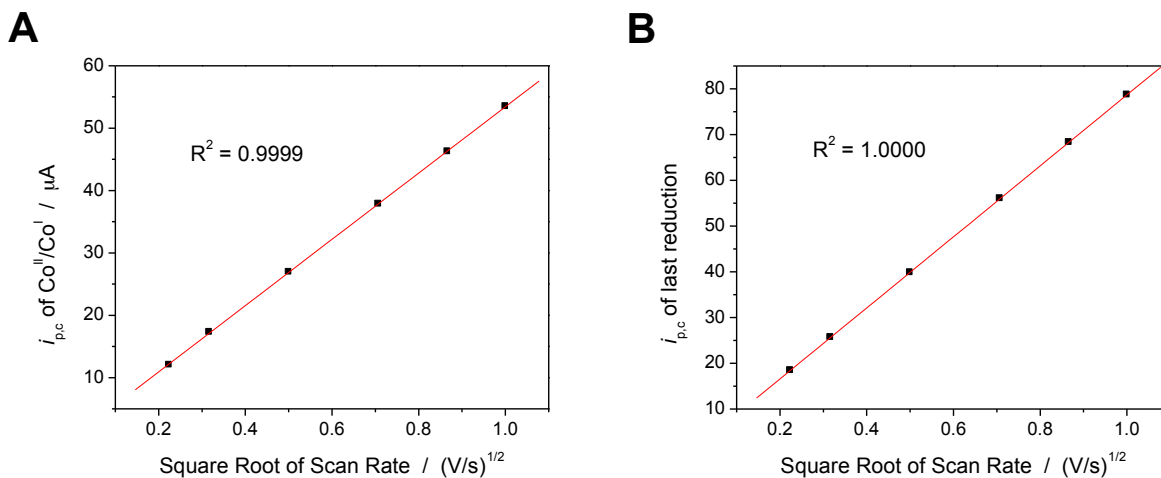
Figure 38. Scan rate dependence of cyclic voltammograms shown in Figure 37. **A)** Reductive peak current of Co(II/I) couple versus the square root of scan rate. **B)** Reductive peak current of last reduction versus square root of scan rate.
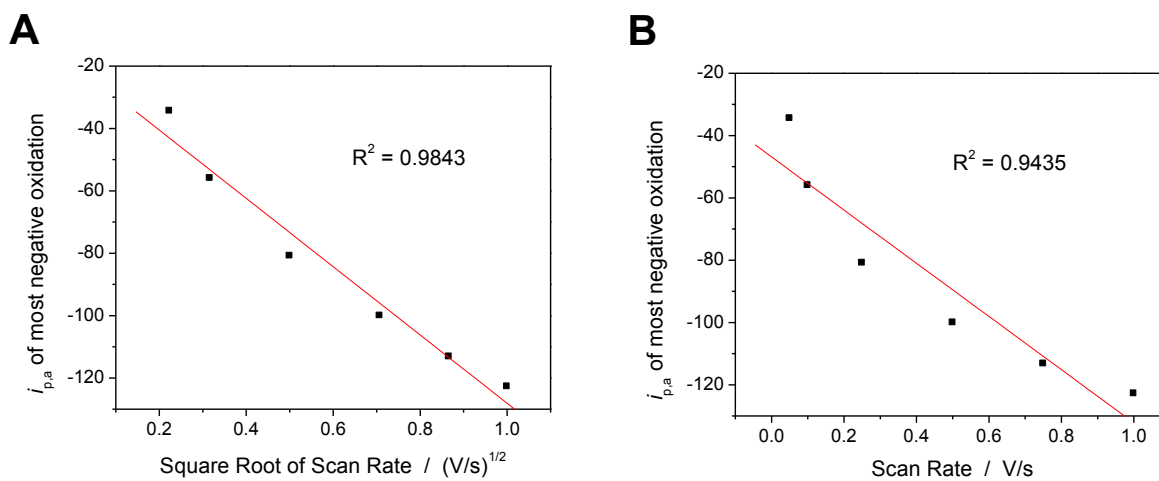
Figure 39. Scan rate dependence of cyclic voltammograms shown in Figure 37. **A)** Oxidative peak current of most negative redox couple versus the square root of scan rate. **B)** Oxidative peak current of most negative redox couple versus scan rate.
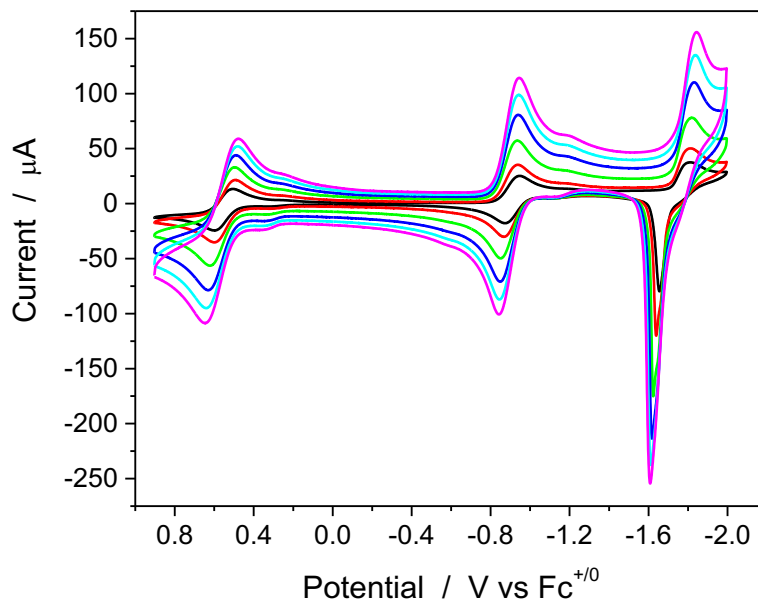
Figure 40. Scan rate dependence of 1-Co in MeCN. Cyclic voltammograms of 2 mM $[(PZ5Me_2)Co(CH_3CN)](OTf)_2$ in 0.1 M Bu_4NPF_6 CH_3CN referenced to ferrocene, scan rates = 50 to 1000 mV/s, with glassy carbon working electrode (3 mm dia.). This solution was prepared by metalating **1** with $Co(CH_3CN)_2(OTf)_2$ in anhydrous CH_3CN and using the crude reaction mixture to form the indicated solution for cyclic voltammetry. HR-ESI-MS (M^+) m/z calc. $[(PZ5Me_2)Co(CH_3CN)^{2+}]$, 274.0730, found, 274.0729. Further characterization was not performed.
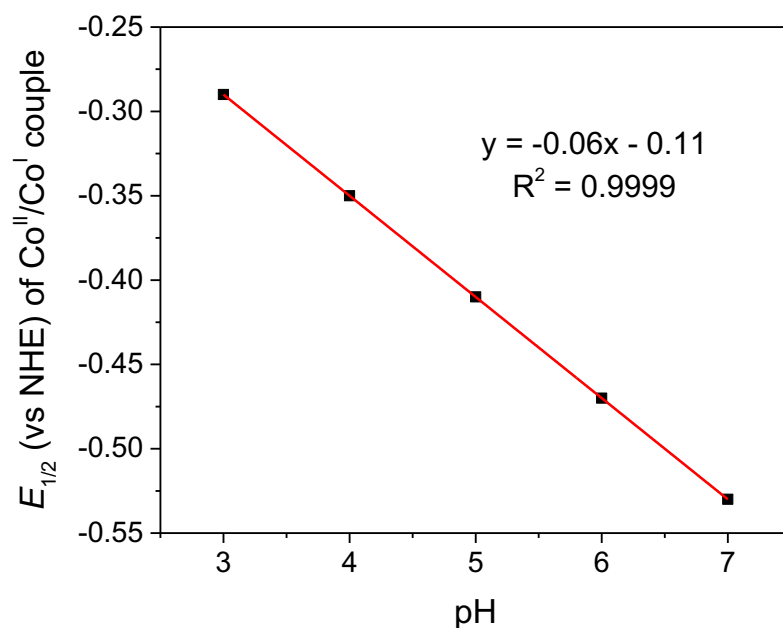
Figure 41. $E_{1/2}$ of Co(II/I) couple versus pH for 1 mM **1-Co** in 25 mM KHP buffer, glassy carbon disc (3 mm dia.). A slope of 60 mV/pH unit is observed from cyclic voltammograms shown in Figure 9.
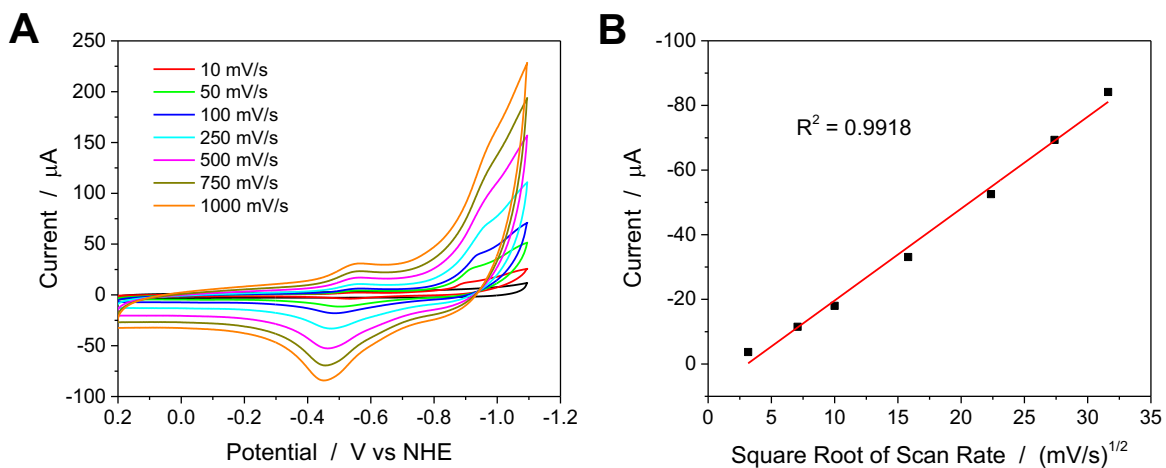
Figure 42. Scan rate dependence for 1-Co in KHP buffer. **A)** Scan rate dependent cyclic voltammograms of 1 mM **1-Co** in 0.025 M pH 7 KHP buffer with 0.1 M KNO$_3$, scan rates from 10 to 1000 mV/s, glassy carbon disc working electrode. **B)** Oxidative peak current of first wave plotted versus the square root of scan rate.
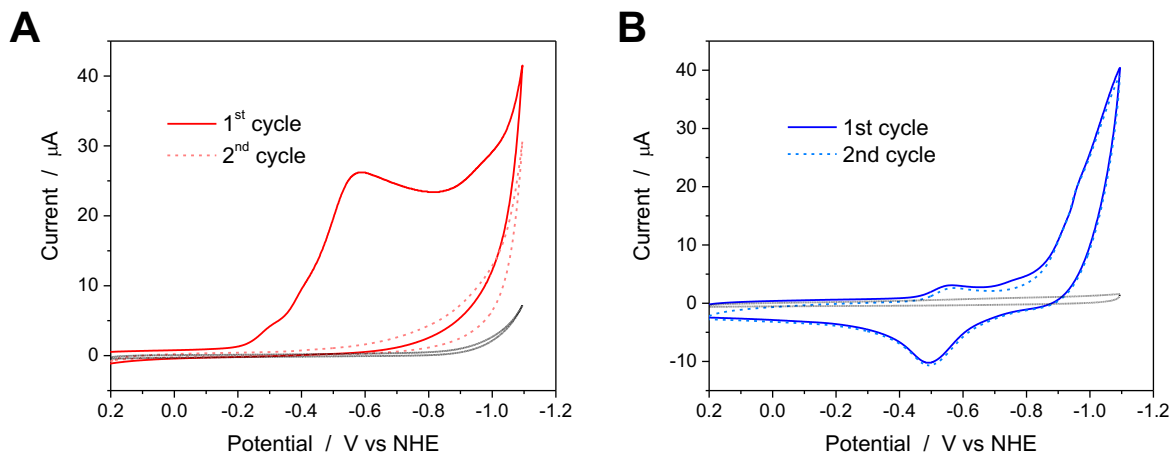
Figure 43. Stability study of 1-Co in pH 3 and pH 7. Cyclic voltammograms of 1 mM **1-Co** in 25 mM KHP buffer at **A)** pH 3 (red) and **B)** pH 7 (blue) with glassy carbon working electrode, $v =$ 50 mV/s. Successive cycles are shown with the second cycle displayed as a dashed line. The background at each pH is shown in black.
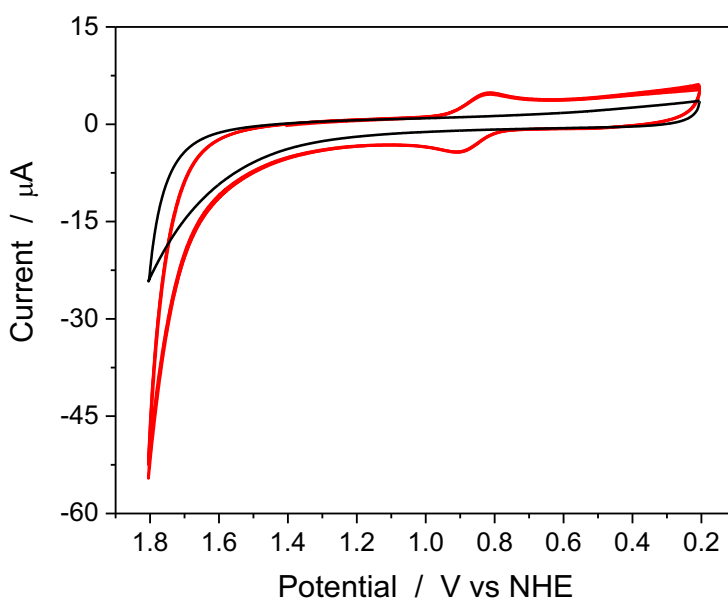
Figure 44. Multi-cycles of CVs for **1-Co**. Cyclic voltammograms of 1 mM **1-Co** in 0.1 M pH 2.5 phosphate buffer showing 10 successive, overlaying cycles with a glassy carbon working electrode, $v = 100$ mV/s. A background CV is shown in black under the same conditions.
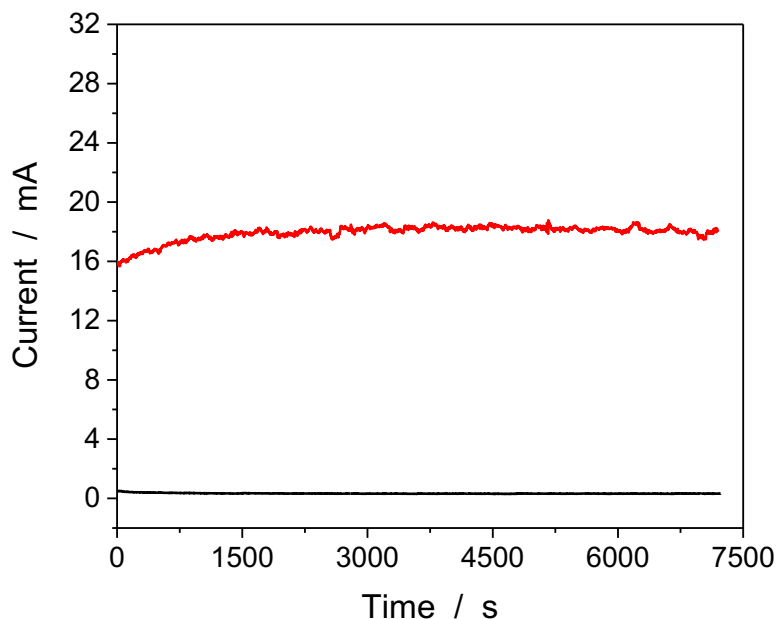
Figure 45. Current vs time plot corresponding to evolved H_2 measurement in Figure 10B with (red line) and without (black line) 10 μM catalyst **1-Co** in 1 M pH 7 phosphate buffer at an applied potential of -1.3 V vs NHE with a Hg pool electrode (A = 12.57 cm^2).
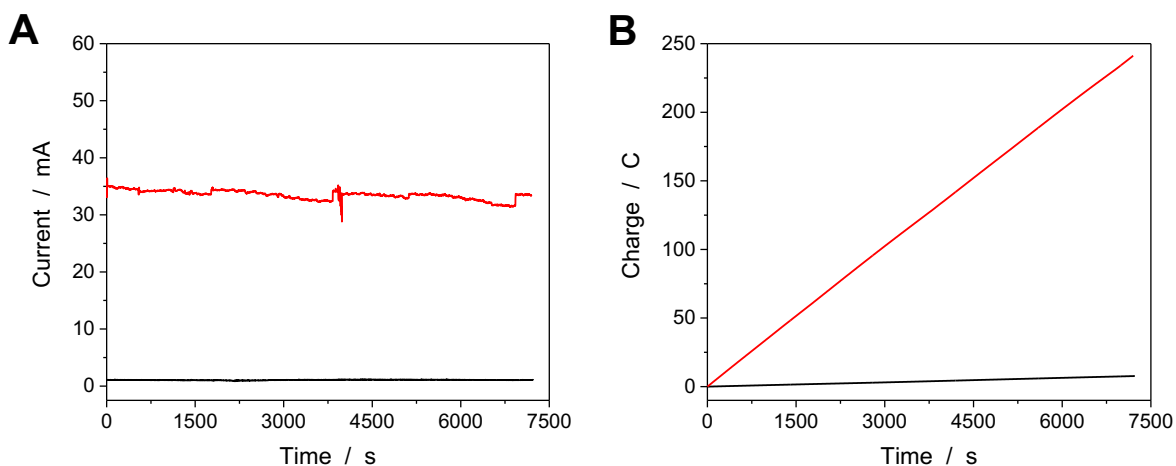
Figure 46. Current (**A**) and charge (**B**) vs time plots from controlled potential electrolyses with (red line) and without (black line) 10 μM catalyst **1-Co** in 1 M pH 7 phosphate buffer at an applied potential of -1.4 V vs NHE with a Hg pool electrode (A = 12.57 cm^2).
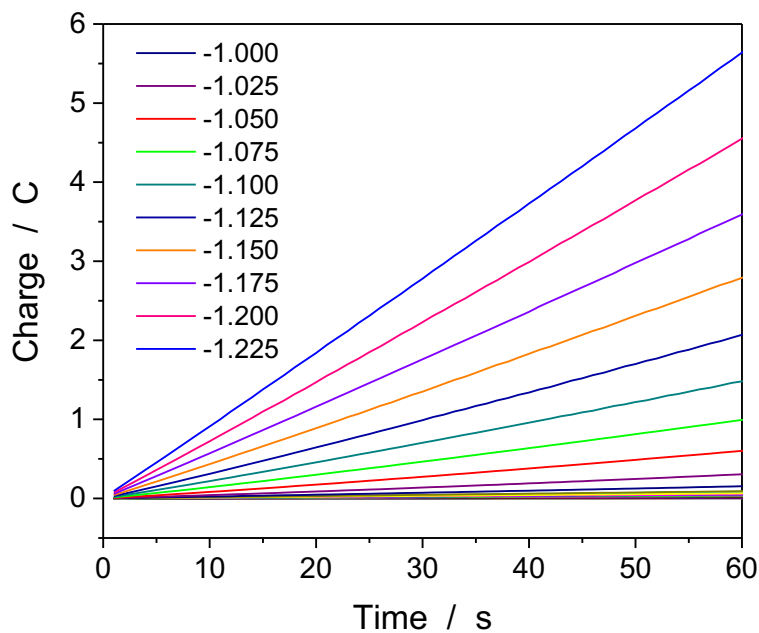
Figure 47. A series of 60-second controlled potential electrolyses at different applied potentials (vs NHE) of 38 μM **1-Co** in 1 M pH 7 phosphate buffer with Hg pool working electrode. The accumulated charge (in Coulombs) is plotted versus time.
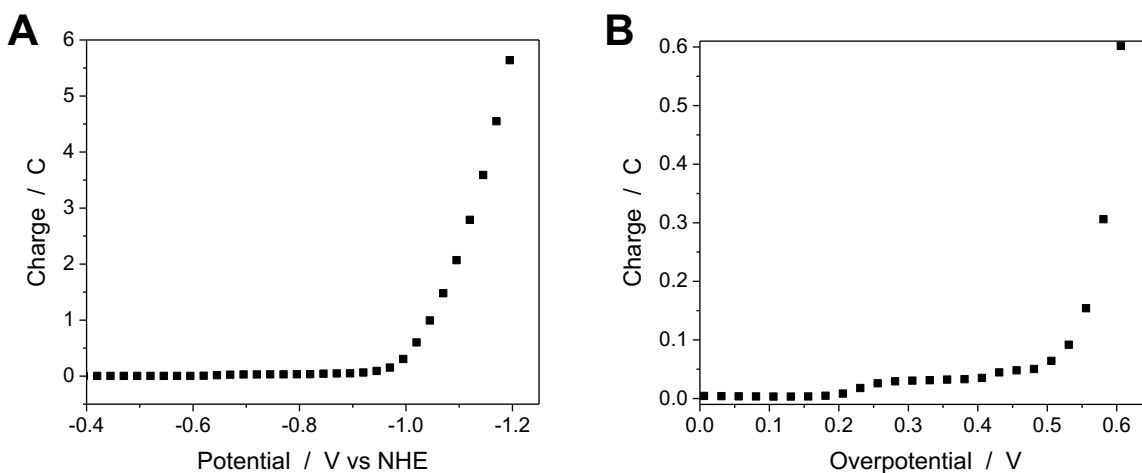
Figure 48. A) Charge build-up versus applied potential, and **B)** charge build-up versus overpotential for water reduction at pH 7, from controlled potential electrolyses in Figure 47. The thermodynamic potential for H_2O reduction at pH 7 was taken to be -0.414 V vs NHE.
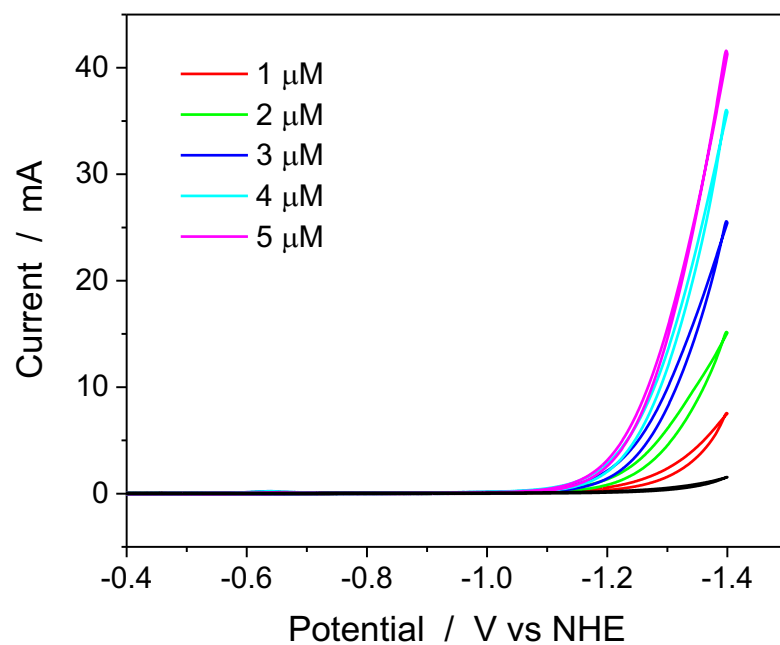
Figure 49. Cyclic voltammograms as different catalyst concentrations of **1-Co** in pH 7 phosphate buffer with a Hg pool working electrode (A = 12.57 cm^2), scan rate = 100 mV/s. A background scan is shown in black.
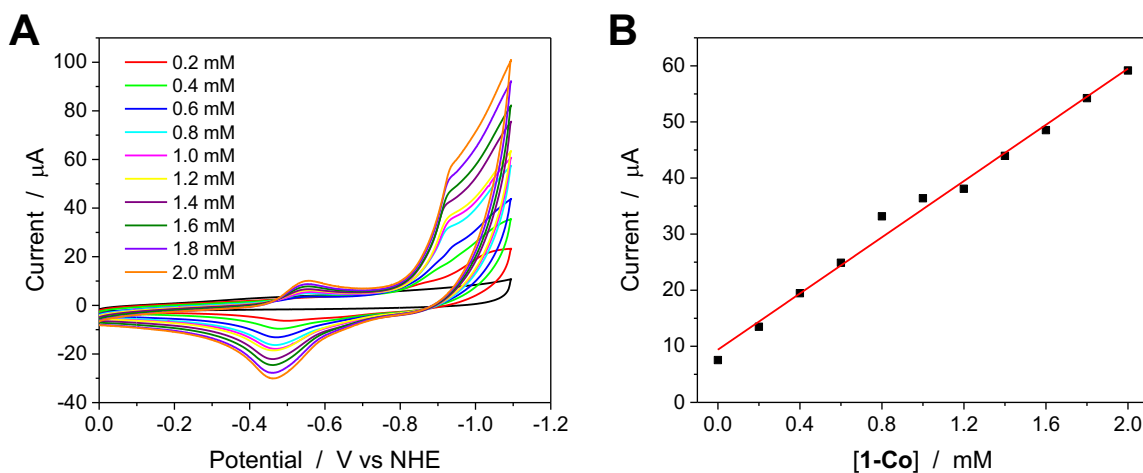
Figure 50. A) Cyclic voltammograms as different catalyst concentrations of **1-Co** in pH 7 KHP buffer with a glassy carbon working electrode, scan rate = 100 mV/s. The background is shown in black under the same conditions. **B**) Catalytic current at -0.95 V versus catalyst concentration.

Table 17. Crystallographic Data for Complex **1-Fe**.

Empirical Formula	$C_{30}H_{27}F_6FeN_7O_6S_2$
Formula Weight	815.56 g/mol
T (K)	100(2)
λ (Å)	0.71073
Crystal System	Monoclinic
Space Group	P2(1)/c
a (Å)	12.1935(3)
b (Å)	12.1099(3)
c (Å)	22.6160(6)
α (°)	90
β (°)	94.494(2)
γ (°)	90
V (Å^3)	3329.26(15)
Z	4
ρ_{calc} (g/cm^3)	1.627
μ (mm^{-1})	0.668
F(000)	1664
θ range for data collection	1.81 to 25.43°
Index ranges	$-14 \leq h \leq 14$ $-14 \leq k \leq 14$ $-27 \leq l \leq 26$
Reflections collected	51528
Independent reflections	6101 [R(int) = 0.0468]
Completeness to $\theta = 67.00°$	99.3%
Max. and min. transmission	0.8893 and 0.8248
Data / restraints / parameters	6101 / 0 / 473
GOF on F^2	1.031
Final R indices [I > 2σ(I)]	$R_1 = 0.0357$, $wR_2 = 0.0685$
R indices (all data)	$R_1 = 0.0570$, $wR_2 = 0.0755$
Largest diff. peak and hole (e Å^{-3})	0.397 and -0.383
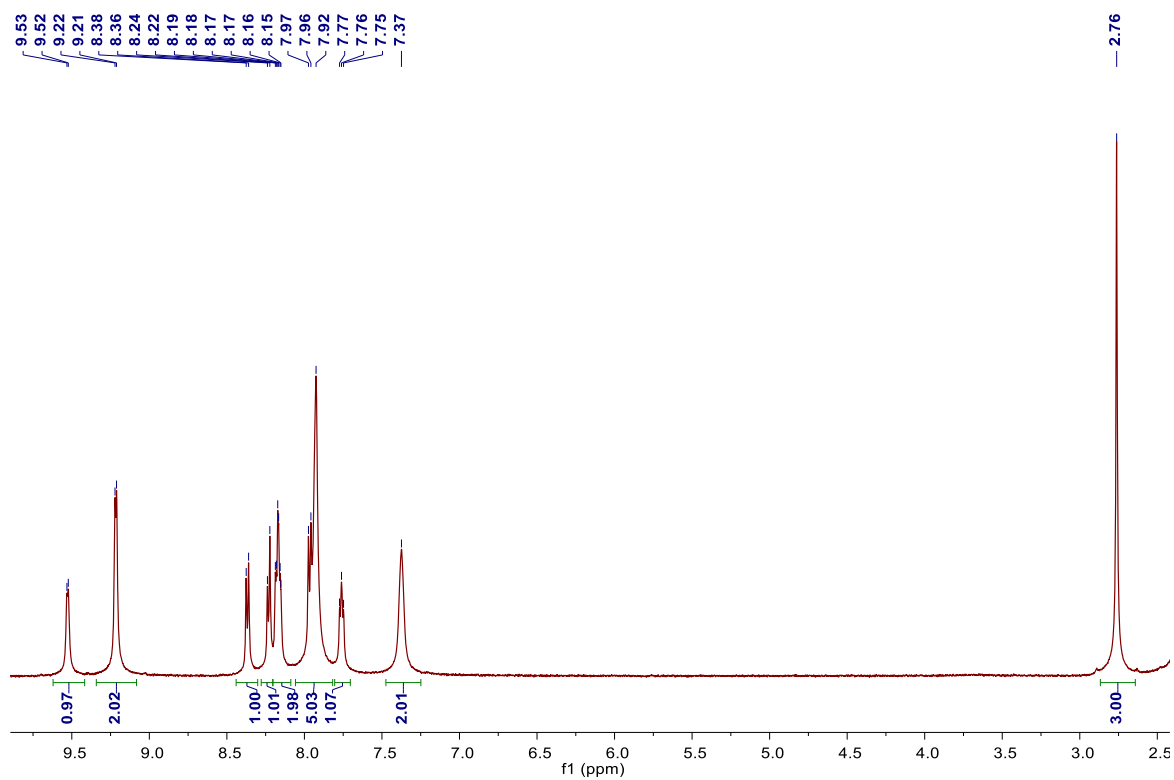
Figure 51. ^{1}H NMR of **1-Fe** (CD$_3$CN, 500 MHz).
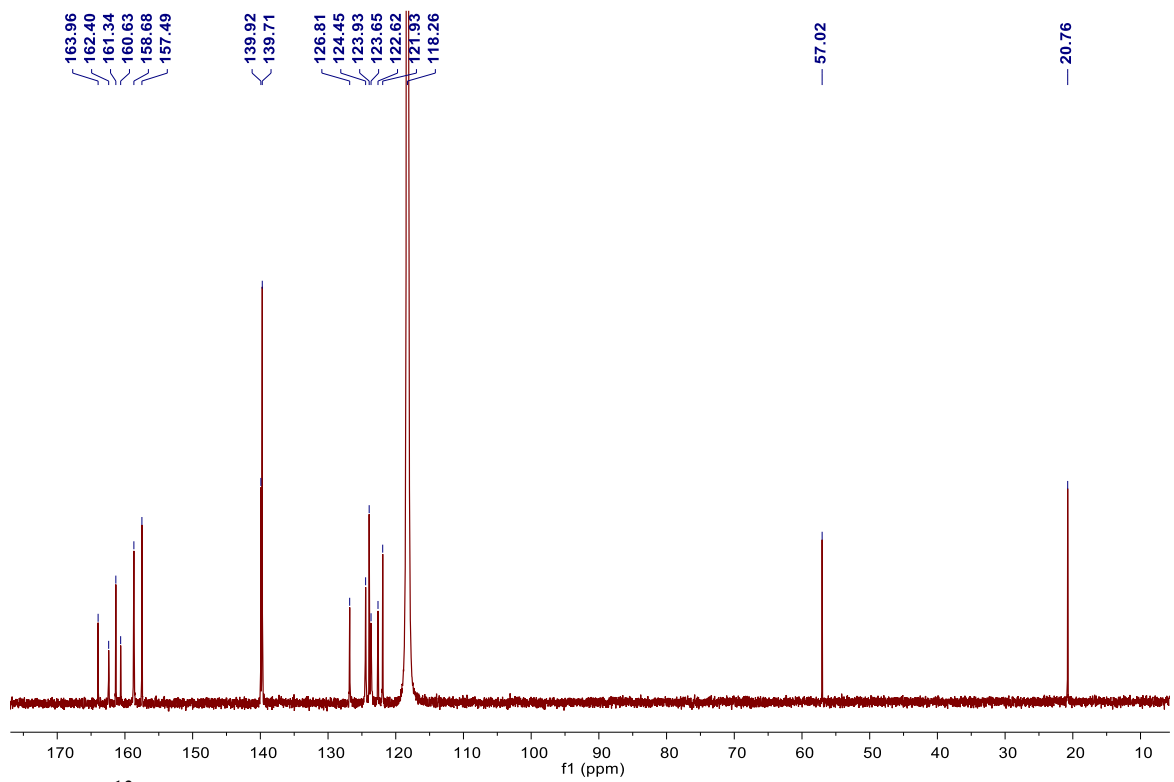
Figure 52. ^{13}C NMR of **1-Fe** (CD$_3$CN, 126 MHz).
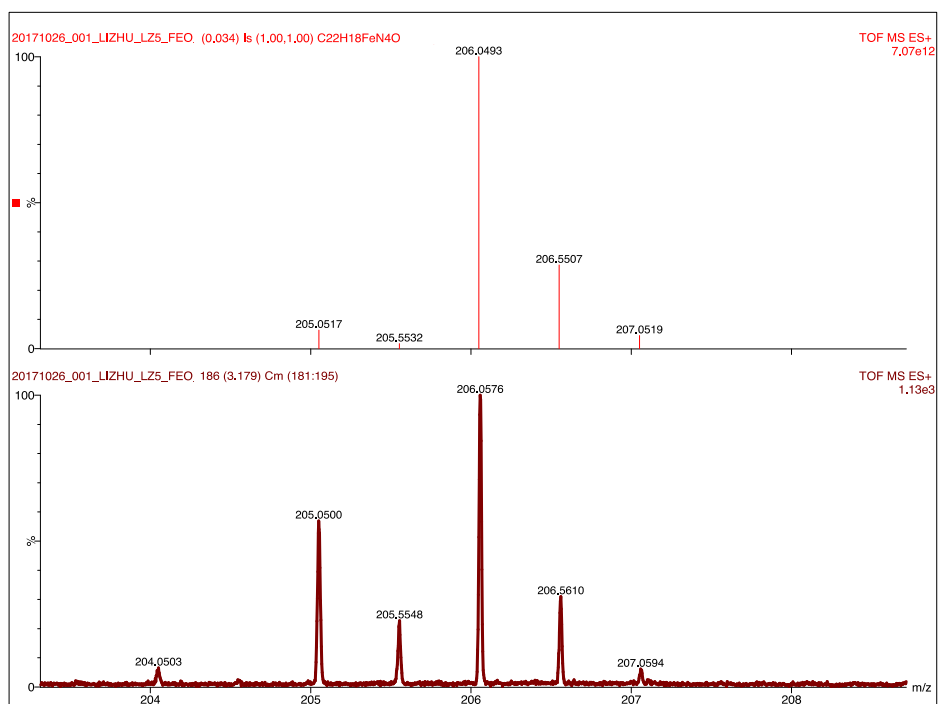
Figure 53. High resolution ESI-MS of Fe(IV)-oxo intermediate, $[(BpyPY2Me)Fe^{IV}(O)]^{2+}$. The intermediate was generated by reacting **1-Fe** with 10 equivalents of *m*CPBA, which was analyzed immediately after addition of the oxidant.
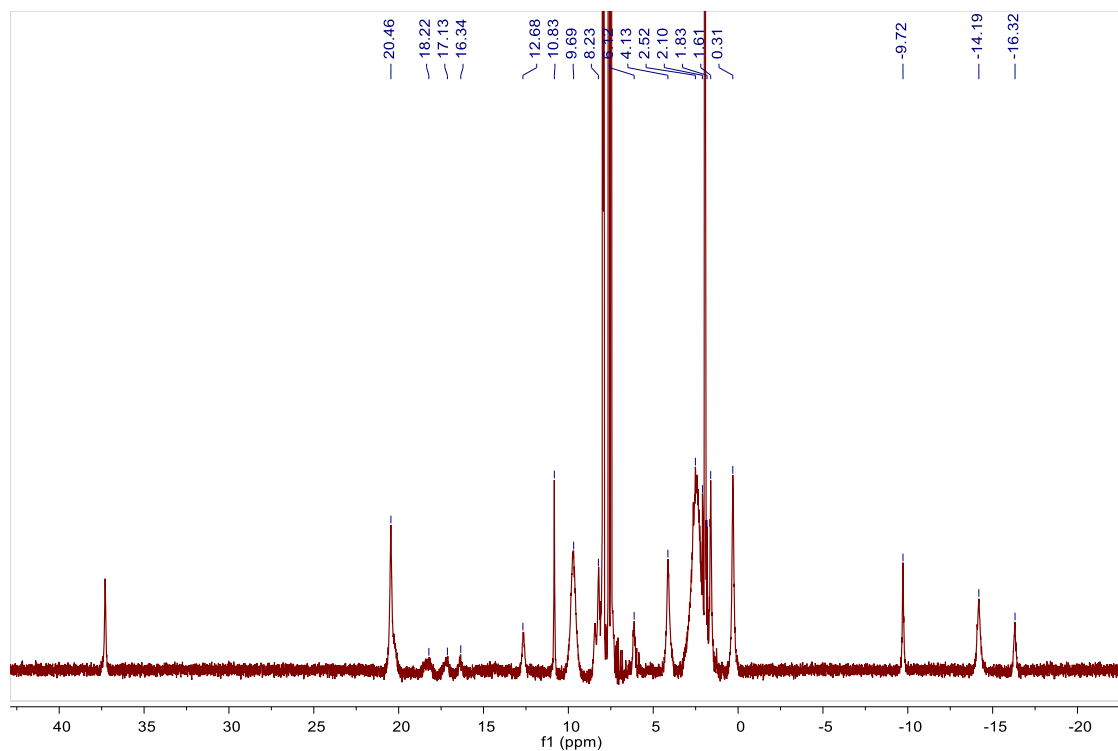
Figure 54. ^{1}H NMR of the iron-oxo species. The intermediate was generated by reacting **1-Fe** with 10 equivalents of *m*CPBA in CD$_3$CN. A similar NMR spectrum, but with broader signals, was obtained after adding 1 equivalent of *m*CPBA to **1-Fe**.
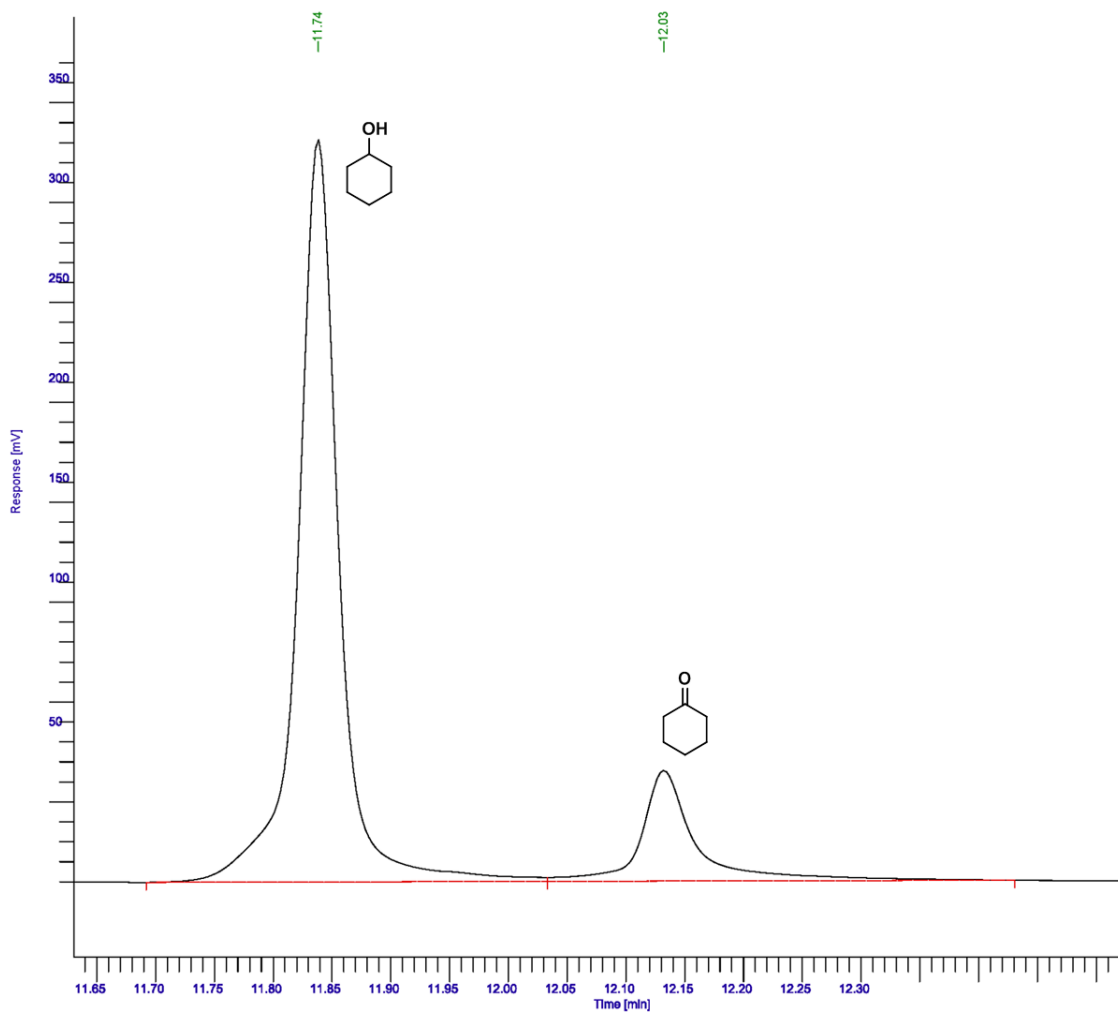
Figure 55. Gas chromatogram of the reaction products generated from reacting 1 mM **1-Fe**, 10 equivalents of *m*CPBA, and 1000 equivalents of cyclohexane.
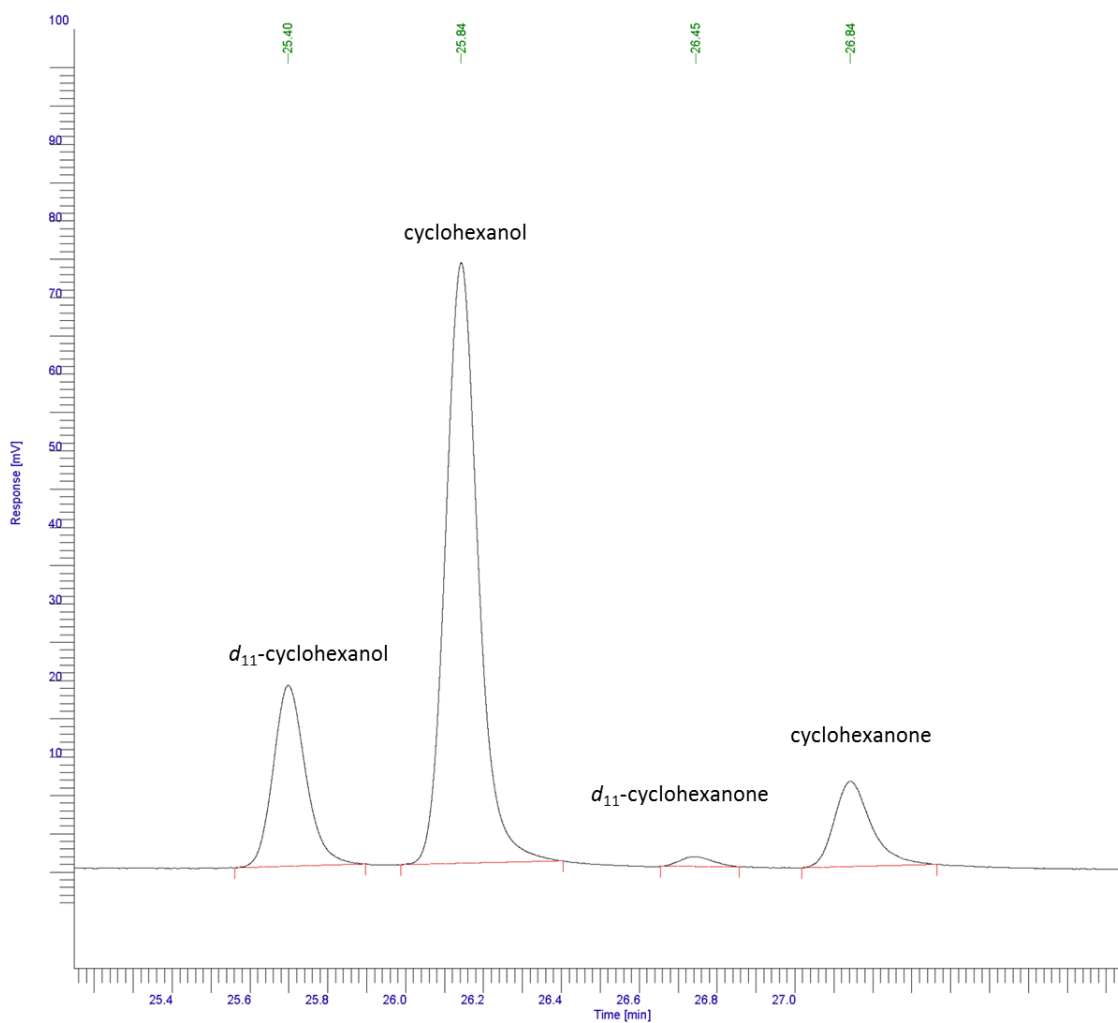
(Top) Gas chromatogram following reaction with 1:1 cyclohexane:d_{12}-cyclohexane.
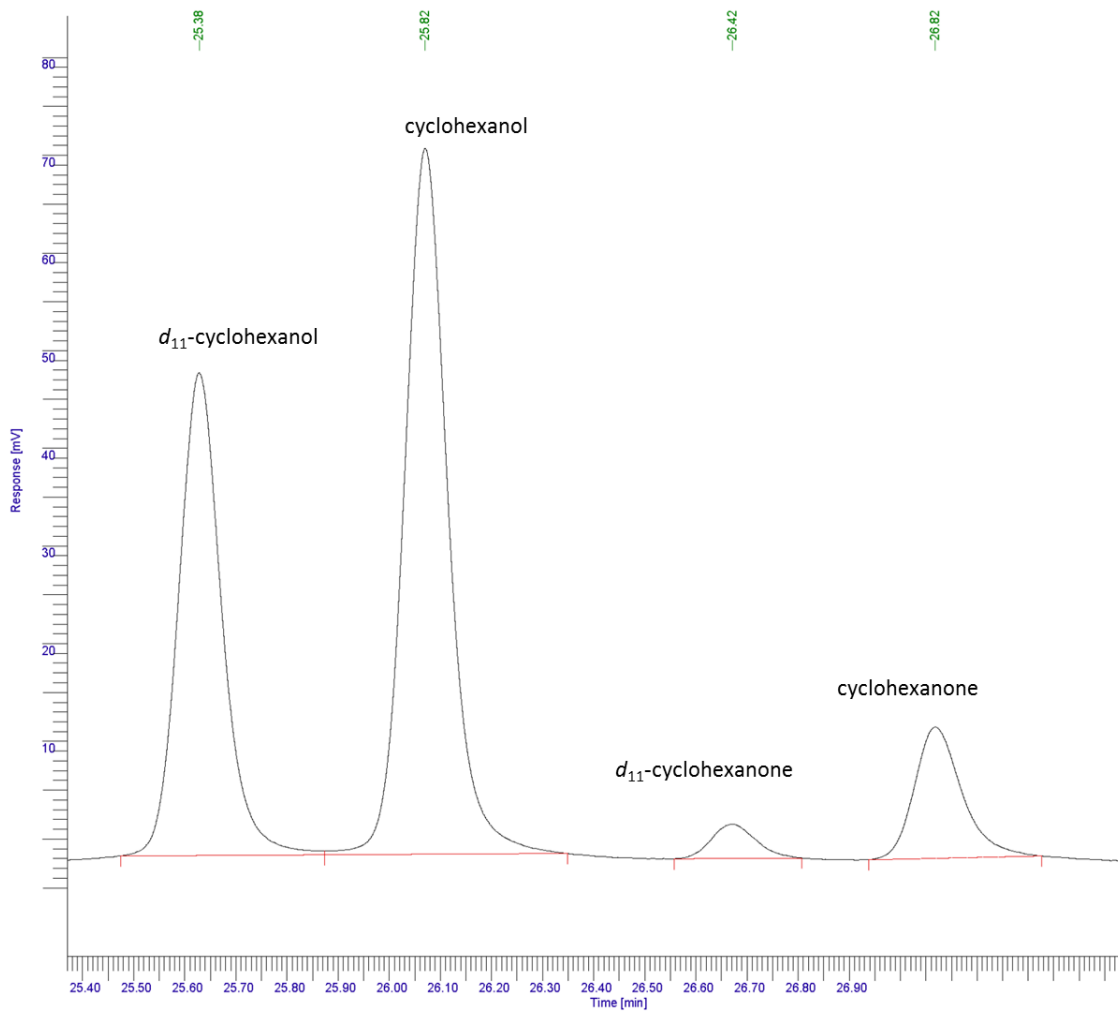
(Middle) Gas chromatogram following reaction with 1:2 cyclohexane:d_{12}-cyclohexane.
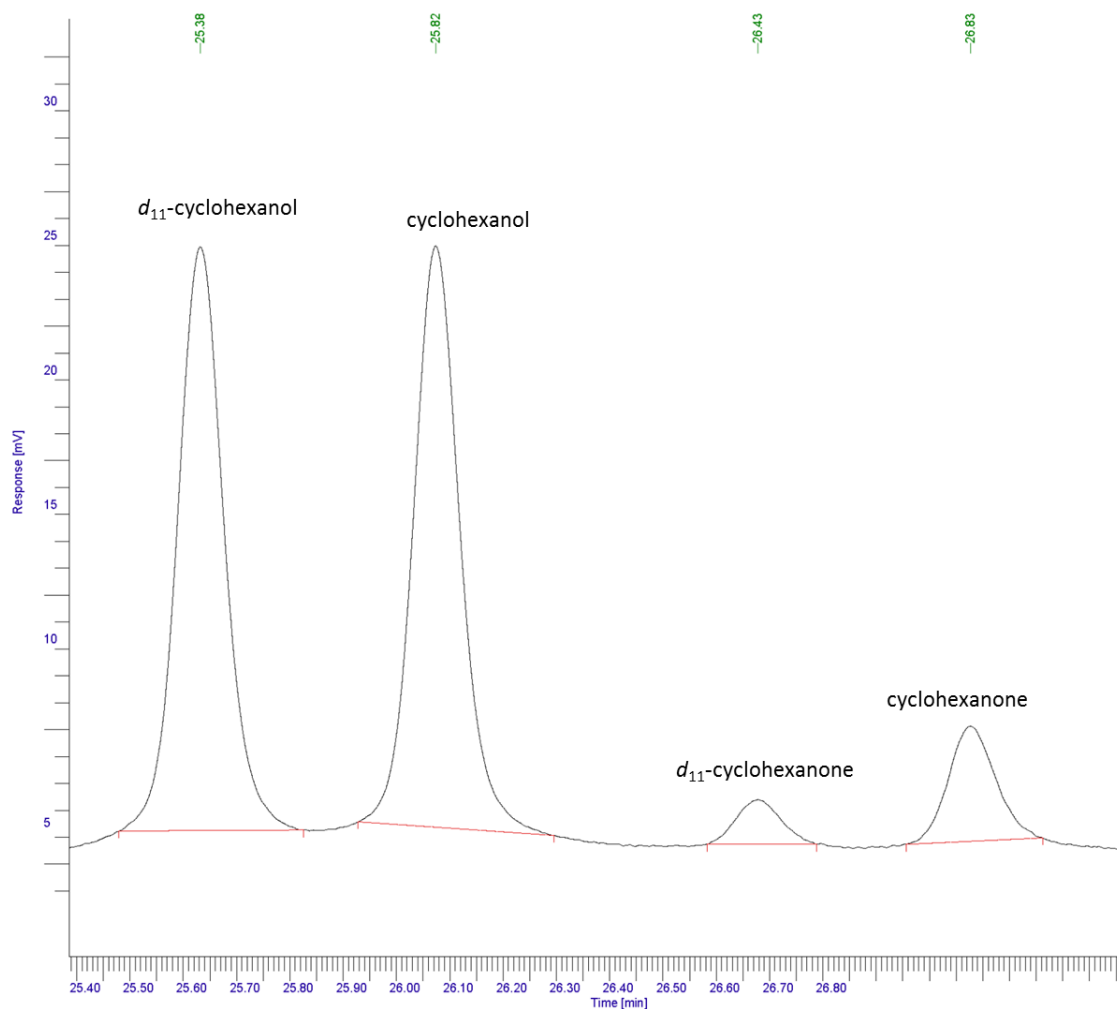
(Bottom) Gas chromatogram following reaction with 1:3 cyclohexane:d_{12}-cyclohexane.

Figure 56. Representative gas chromatograms of reaction products generated from reacting 1 mM **1-Fe**, 10 equivalents of *m*CPBA, and 1000 equivalents of cyclohexane:d_{12}-cyclohexane with different ratios (1:1, top; 1:2, middle; 1:3, bottom).
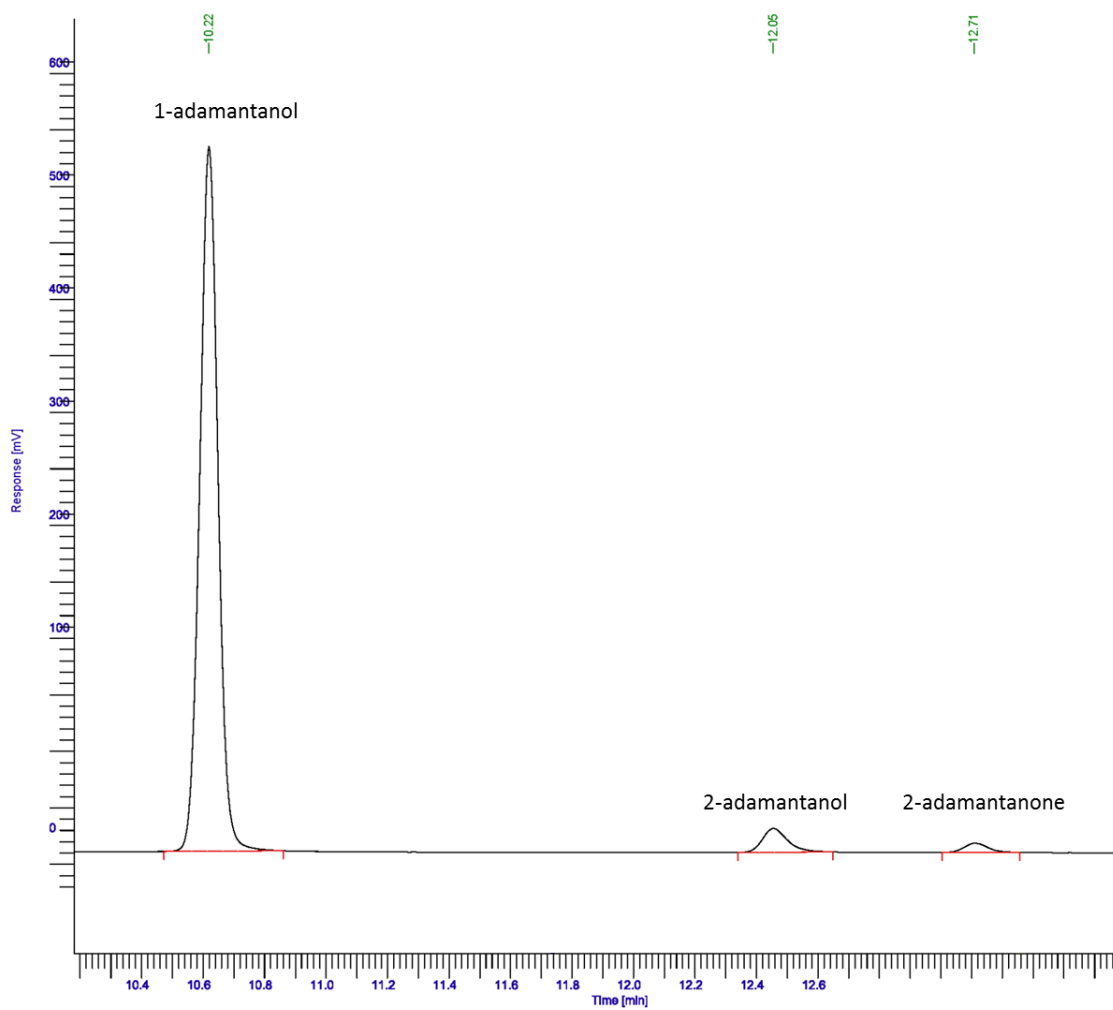
Figure 57. Gas chromatogram of the reaction products generated from reacting 1 mM **1-Fe**, 10 equivalents *m*CPBA, and 500 equivalents adamantane.
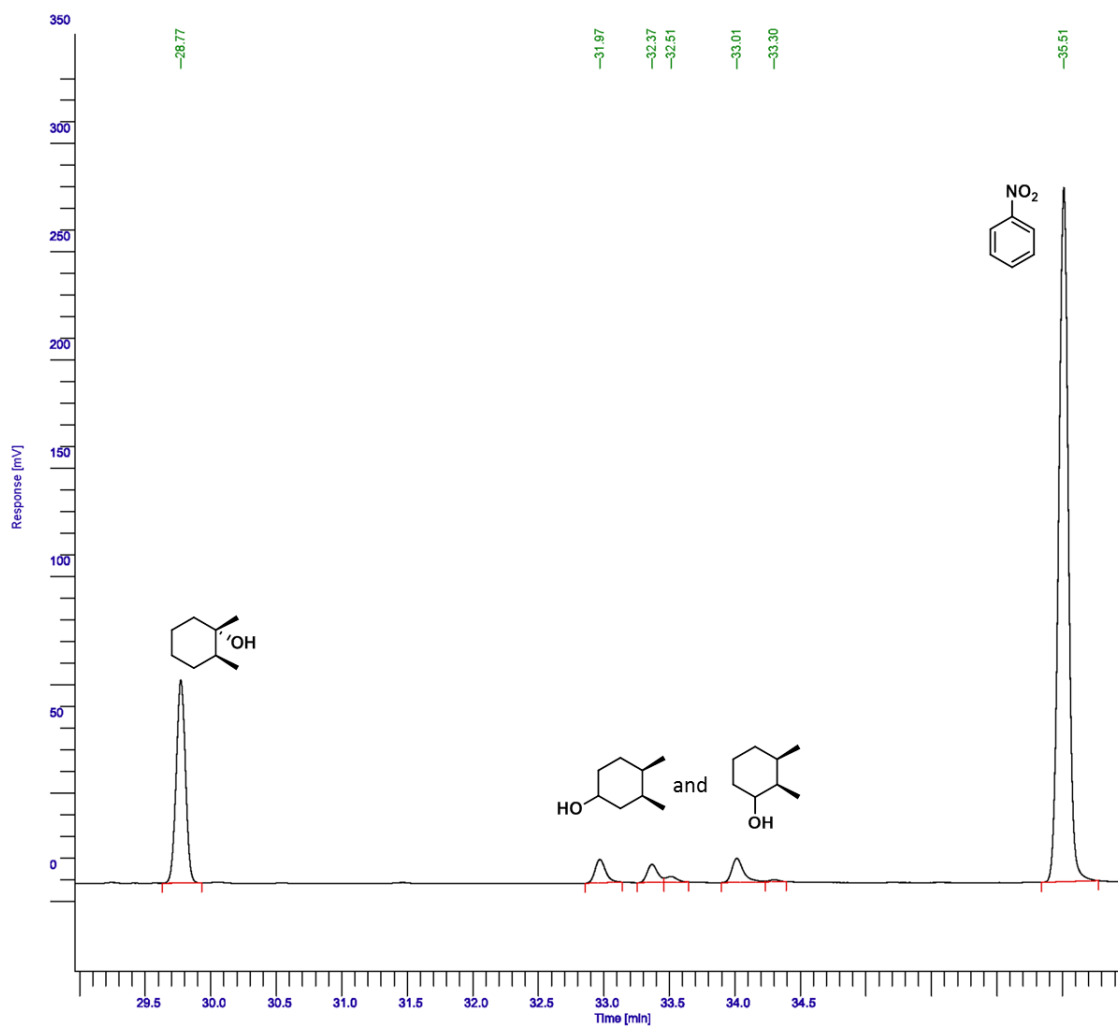
Figure 58. Gas chromatogram of reaction products generated from reacting 1 mM **1-Fe**, 20 equivalents of *m*CPBA, and 25 equivalents of *cis*-dimethylcyclohexane.
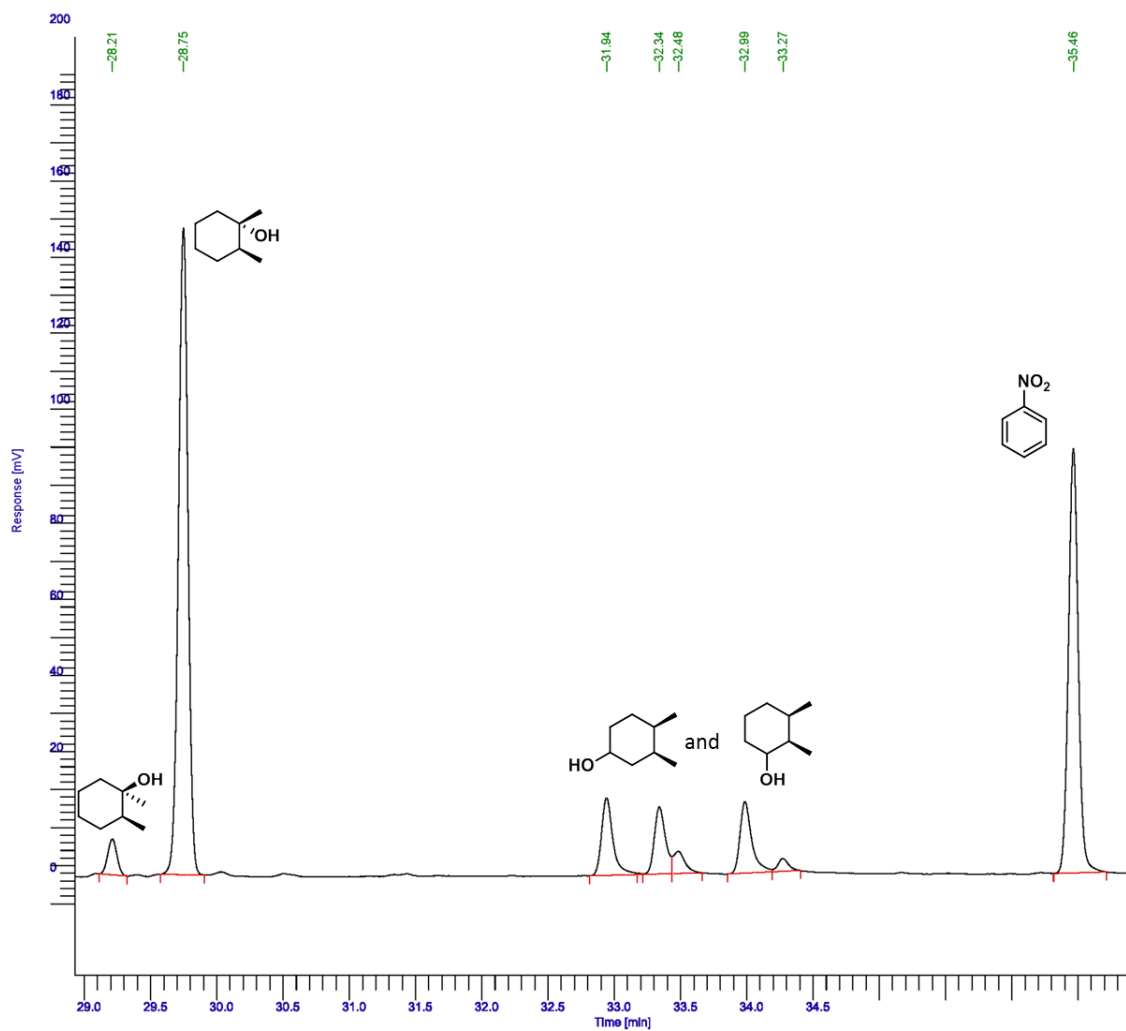
Figure 59. Gas chromatogram of reaction products generated from reacting 1 mM **1-Fe**, 100 equivalents of *m*CPBA, and 120 equivalents of *cis*-dimethylcyclohexane.

Journal permission for chapter 1.

Synthesis of a pentadentate, polypyrazine ligand and its application in cobalt-catalyzed hydrogen production

Check for updates

Lizhu Chen,[a] Amir Khadivi,[a] Manpreet Singh[a] and Jonah W. Jurss[*a]

⊕ Author affiliations

Abstract

A molecular cobalt complex bearing a pentadentate, polypyrazine ligand, 2,6-bis(1,1-di(pyrazin-2-yl)ethyl)pyrazine (PZ5Me$_2$), has been developed for

About   Cited by   Related

Journal permission for chapter 2.

Journal permission for chapter 3.

Publishing Journals Books Databases Advanced ROYAL SOCIETY OF CHEMISTRY

Log in / register

Issue 23, 2018   Previous Article   Next Article   About   Cited by   Related

From the journal:
New Journal of Chemistry

- For reproduction of material from all other RSC journals and books: Reproduced from Ref. XX with permission from The Royal Society of Chemistry.

High-spin enforcement in first-row metal complexes of a constrained polyaromatic ligand: synthesis, structure, and properties

Check for updates

If the material has been adapted instead of reproduced from the original RSC publication "Reproduced from" can be substituted with "Adapted from".

In all cases the Ref. XX is the XXth reference in the list of references.

Lizhu Chen,[a] Hunter A. Dulaney,[a] Branford O. Wilkins,[b] Sarah Farmer,[a] Yanbing Zhang,[a] Frank R. Fronczek[c] and Jonah W. Jurss*[a]

⊕ Author affiliations

If you are the author of this article you do not need to formally request permission to reproduce figures, diagrams etc. contained in this article in third party publications or in a thesis or dissertation provided that the correct acknowledgement is given with the reproduced material.

Abstract

The coordination chemistry of a rigid tetradentate polypyridyl ligand has

VITA

EDUCATION

M.S. in Chemistry (Inorganic Chemistry)

University of Mississippi, *University, MS*, May. 2019, GPA: 3.83/4.0

    Advisor: Jonah W. Jurss

B.S. in Pharmaceutical Engineering (Medicinal Chemistry)

Shenyang Pharmaceutical University, *Shenyang, China,* July 2014 GPA: 3.3/4.0

    Advisors: Yongxiang Liu

RESEARCH EXPERIENCE

Graduate Research   January 2015 – May 2019

- Successfully synthesized 4 robust Iron catalysts for water oxidation and the C-H bond functionalization with excellent selective and stable catalysts for C-H bond oxidation.

- Developed a pentadentate, polypyrazine ligand and applied for Co catalyzed proton reduction, which successfully improved the reactivity and overpotential for proton reduction compared to a reported pentadentae, polypyridine cobalt complex.

- Studied a series of macrocyclic N-heterocyclic carbene (NHC) cobalt complexes for selectively reduce CO_2 to CO in aqueous solutions.

- Applied a series of macrocyclic N-heterocyclic carbene (NHC) cobalt complexes for efficiently reduce proton with a significantly low overpotential as low as 200 mV.

- Developed a series of macrocyclic N-heterocyclic carbene (NHC) Fe catalysts for reactively and selectively reducing CO_2.

- Synthesized a rigid and highly preorganized biphenylbisbypyridine ligand for first row metals for analyzing the effect of ligand to the metal complexes' structures, evaluating their magnetic properties and spin crossover study.

Undergraduate Research   June 2013 – May 2014

- Studied the sythesis of isoprekinamycin

- Helped the condition optimization for gold-catalyzed synthesis of naphthalene

- Studided the synthesis of sulfonamide inhibitors of carbonic anhydrases

PUBLICATION

1) **Chen, L.**; Dulaney, H. A.; Wilkins, B. O.; Farmer, S.; Zhang, Y.; Fronczek, F. R.; Jurss, J. W. "High-Spin Enforcement in First-row Metal Complexes of a Constrained Polyaromatic Ligand: Synthesis, Structure, and Properties." *New. J. Chem.* **2018**, 42, 18667

2) **Chen, L.**; Su, X.; Jurss, J. W. "Selective Alkane C-H Bond Oxidation Catalyzed by a Nonheme Iron-oxo Complex Featuring a Robust Tetradentate Ligand." *Organometallics*. **2018**, 37, 4535.

3) **Chen, L.**; Khadivi, A.; Singh, M.; Jurss, J. W. "Synthesis of a Pentadentate, Polypyrazine Ligand and its Application in Cobalt-Catalyzed Hydrogen Production." *Inorg. Chem. Front.* **2017**, 4, 1649.

4) Liu, Y.; Guo, J.; Liu, Y.; Wang, X.; Wang, Y.; Jia, X.; Wei, G.; **Chen**, **L.**; Xiao, J.; Cheng, M. "Au(I)-Catalyzed Triple Bond Alkoxylation/Dienolether Aromaticity-Driven Cascade Cyclization to Naphthalenes" *Chem Comm*. **2014**, 50, 6243.

PRESENTATIONS

1) "Water Reduction at Low Overpotentials with Cobalt Pyridyl-NHC Electrocatalysts"

National Meeting of the American Chemical Society, New Orleans, LA.   March 2018

2) "New Robust Iron-oxo Catalysts for C-H Bond Functionalization"

   National Meeting of the American Chemical Society, New Orleans, LA.   November 2017

3) "Robust Fe oxo catalyst for C-H bond functionalization"   July 2016

   Feeding and Powering the World, University of Mississippi, University, MS.

4) "Robust catalysts for water oxidation" ***awarded first prize***   June 2016

   Feeding and Powering the World, University of Mississippi, University, MS.

5) "Robust catalysts for water oxidation"   April 2016

   Graduate Student Council Research Day Symposium, University of Mississippi, University,

   MS.

6) "Robust iron-oxo catalysts for water oxidation "   November 2015

   Southeast Regional Meeting of the American Chemical Society, Memphis, TN.

TEACHING EXPEREINCE

General Chemistry Lab 115 and 116, University of Mississippi, University, MS, Prof. Wiginton

January 2015 – May 2018

- Taught two Organic Chemistry sections of 45+ students weekly per semester.

- Graded assigned homework and held weekly office hours for 45+ students.

Inorganic Chemistry Lab, University of Mississippi, University, MS, Prof. Cleland   September

2016 – December 2017

- Mentor seven students of inorganic chemistry weekly during the semester.

- Prepare the chemicals and glassware's needed for the coming lab

Student Mentoring

- Katrina Gateley (Undergraduate student)

- Sarah Farmer (Undergraduate student, authored one paper together)

- Allison Hunter (Undergraduate student)

- Emily Ables (Undergraduate student)